CHAPTER 4: NUMERICAL INVESTIGATION

4.1 Introduction

This numerical investigation was conducted to establish an adequate transverse system in decked bulb T beam bridges and to ensure the distribution of the traffic load without over-stressing or cracking the shear key joints between the beams. The numerical investigation was conducted using the commercial software package ABAQUS version 11.2.1. The investigated transverse post-tensioning (TPT) system in decked bulb T beam bridges consisted of a series of transverse diaphragms, which were either non-prestressed or prestressed with TPT force applied through un-bonded TPT CFCC strands.

This chapter is composed of four main sections. The first section offers a detailed explanation for: the components of the numerical models, material properties, elements types, boundary conditions, analysis steps, and all the assumptions that have been used through the process of modeling. The second section presents the verification of the numerical investigation. The verification was executed by generating and analyzing numerical models for the control beams and bridge model. The third section provides the results of a parametric study that was conducted on real-scale bridges. The fourth section summarizes the results of the numerical investigation and presents a guide specification for transverse post-tensioning systems in typical decked bulb T beam bridges.

4.2 Components of numerical models

All numerical models including verification models and those of the parametric study were composed of decked bulb T beams reinforced and prestressed longitudinally with CFCC strands and transversely with steel or CFCC stirrups. All beams and bridge models were simply supported over two reinforced neoprene pads at their ends. No deck slab was provided but the top flanges of the beams were connected together using UHPC shear key joints. In addition, transverse diaphragms made of UHPC and transverse elements representing TPT CFCC strands were provided in some of the numerical models. The following subsections represent the details of each bridge component.

4.2.1 Decked bulb T beams

The concrete of the decked bulb T beams was simulated using a brick element (C3D8R). This is a three dimensional element with eight nodes as shown in Figure 4.2-1. Each node has three transitional degrees of freedom (U_x , U_y , U_z,).

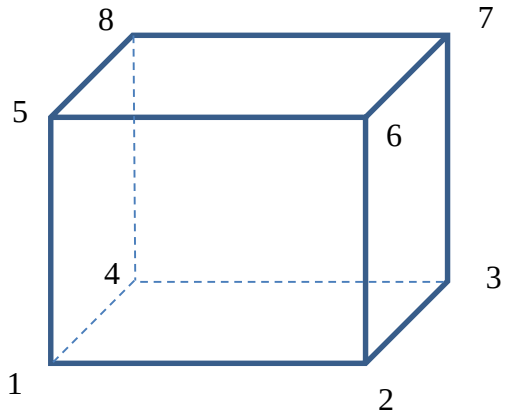

Figure 4.2-1 Illustration of C3D8R brick element used to mode decked bulb T beams (ABAQUS Manual 2011)

A continuum, plasticity-based, damage model for concrete was used to model the material behavior. The concrete damaged plasticity model uses concepts of isotropic damaged elasticity in combination with isotropic tensile and compressive plasticity to represent the inelastic behavior of concrete. It assumes that the main two failure mechanisms are tensile cracking and compressive crushing of the concrete material. Consequently, the concrete material was defined by its uni-axial compressive and tensile performance in addition to the elastic properties.

For compressive stress, the material model response is linear until the value of initial yield. The initial yield is assumed to occur at a stress equal to 60% of the concrete ultimate strength and then the material begins the plastic response, which is typically characterized by stress hardening followed by strain softening beyond the ultimate stress.

For tensile stress, the stress-strain response follows a linear elastic relationship until reaching the value of the cracking stress, which corresponds to the onset of micro-cracking in the concrete material. Beyond the cracking stress, the formation of micro-cracks is represented macroscopically with a softening stress-strain response, which includes strain localization in the concrete structure.

The elastic properties of the concrete including the modulus of elasticity, Poisson's ratio, and modulus of rupture were estimated according to AASHTO LRFD Sections 5.4.2.4, 5.4.2.5, and 5.4.2.6, respectively.

4.2.2 Reinforcement

The reinforcement cages of the decked bulb T beams were modeled using a two-node linear 3D truss element (T3D2) shown in Figure 4.2-2. Each node has three degrees of freedom (U_x , U_y , U_z,). Truss elements were embedded inside the host elements or concrete brick elements. The transitional degrees of freedom of the embedded element nodes were constrained to the interpolated values of the corresponding degrees of freedom of the host element nodes.

The behavior of CFCC reinforcement was assumed elastic to failure. The maximum strength and strain of the material was taken from the material data sheets provided by the manufacturer (Tokyo Rope Co.). It should be noted that there is a slight uncertainty in the ultimate strength and strain of CFCC material. The material data sheets showed a maximum strain within the range of 1.6 to 1.7%. Therefore, during the verification stage, the ultimate strain and corresponding strength was optimized based on the results from the experimental investigation. Losses were taken as 15% of initial prestressing force for all numerical models.

Besides CFCC strands, low-relaxation steel strands with a diameter of 0.6 in. were used in Beam S-S-F-U and steel stirrups were used through all the numerical models except for Beam C-C-S-B. The material properties of the reinforcing steel bars (assuming Grade 60 ksi) and steel strands were taken from AASHTO LRFD 2012 Sections 5.4.3 and 5.4.4, respectively.

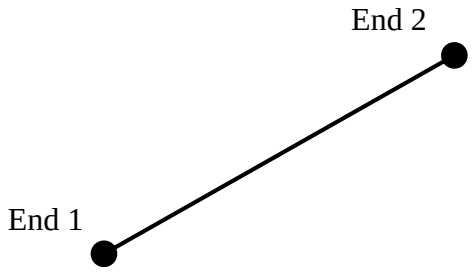

Figure 4.2-2 Two-node linear 3D truss element T3D2 for reinforcement (ABAQUS 2011)

4.2.3 Shear key joints

The shear key joints were modeled using the same three dimensional brick element C3D8R. The material properties were taken based on experimental test results of uni-axial compressive strength test preformed on UHPC cylinders and also with reference to previous studies (Graybeal 2006). The ultimate compressive strength was taken as 28 ksi. The modulus of elasticity was taken as 7000 ksi, while the cracking strength was taken as 1500 psi.

Based on the experimental investigation, the interface between the UHPC and the concrete is stronger than the concrete itself. Therefore, the cracking is likely to occur on the concrete side and not through the interface or the UHPC. Therefore, through the numerical analysis, a full bond was assumed through the interface between the UHPC and the concrete of the beams. The full bond was achieved by assigning a "TIE" element between the nodes of surfaces in contact. The TIE element is a virtual element that constrains the degrees of freedom of one node on one of the surfaces, called the slave surface, to the degrees of freedom of the nearest node on the other surface, called the master surface. The master surface was taken as the surface of the beam, while the slave surface was taken as the surface of the UHPC shear key joint.

4.2.4 Reinforced elastomeric bearing pads for supports

The end supports were provided for the decked bulb T beams as steel-reinforced elastomeric bearings. The bearings were composed of alternate layers of steel reinforcement and elastomer bonded together. The elastomer was defined in the numerical analysis as a hyper-elastic material of ultimate uni-axial tensile stress of 2500 psi and ultimate uni-axial tensile strain of 400% (complies with ASTM D412). Both the reinforcement and the elastomer layers were modeled with eight-node linear brick elements. However, the elements functioned differently during the analysis. The reinforcement layers were modeled with element type C3D8R. This element is controlled by the reduced integration during the analysis (identified by the letter R at the end of the name). The elastomer layers, on the other hand, were modeled with element type C3D8H. This element is controlled by hybrid formulations that can deal with the elastomer material behavior (identified by the letter H). The ABAQUS Manual (2011) for element types provides a detailed description for both elements and their functions.

The length, width, and thickness of the bearing pads were calculated according to AASHTO LRFD 14.7.5 (2012). The pads used in the experimental models had a length of 12 in., a width of 6 in. and a thickness of 1.0 in. The pad is composed of three elastomer layers with a thickness of 0.25 in. each and alternated with two steel layers with a thickness of 0.125 in. each. On the other hand, the pads assigned for the models in the parametric study had a length of 32 in., a width of 8 in. and a thickness of 2.075 in. divided into: three steel layers of thickness 0.125 in. each, two interior elastomer layers of thickness 0.6 in. each, and two exterior elastomer layers of thickness 0.25 in. each. It should be noted that due to their fine detailing, elastomeric bearing pads required a significantly large number of elements, which resulted in considerable CPU time delay in the analysis. Therefore, in models with a large number of elements, elastomeric bearing pads were replaced with steel plates of the same dimensions and boundary conditions were assigned as a roller support for one side and a pin support for the other side. This simplification was verified before implementation and the difference in the results were proven insignificant.

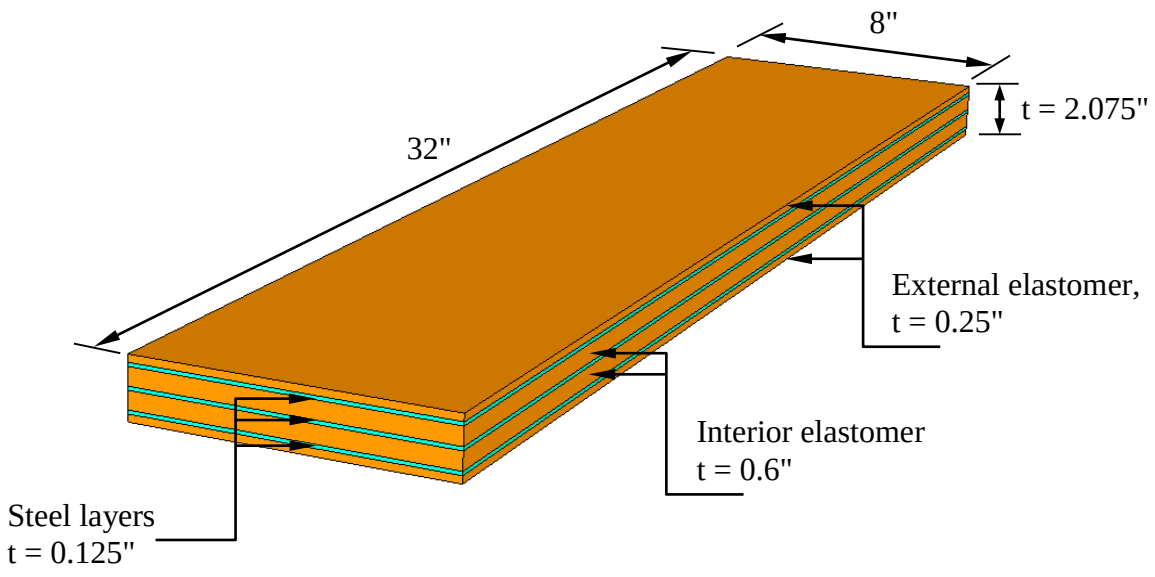

Figure 4.2-3 Elastomeric bearing pad for one beam

4.2.5 Transverse diaphragms

The transverse diaphragms were modeled using the brick element C3D8R with material properties of UHPC. It was assumed that the diaphragms will be cast in place along with the shear key joints from the same UHPC batch. It was also assumed that full bond is developed between the diaphragm and the sides of the decked bulb T beams. No slippage or separation was allowed between the diaphragms and the beams.

4.2.6 Transverse post-tensioning cables

The two-node truss element (T3D2) was used to model the transverse un-bonded post-tensioning strands which functioned as ties confining the decked bulb T beams transversely. The end nodes of the transverse strands were tied to steel plates acting as end bearing plates. The steel plates were tied to the exterior sides of the external box beams. The interior nodes of the post-tensioning strands were not tied to the surrounding objects. The steel plates in this connection were provided to distribute the post-tensioning force on the concrete surface and prevent any concrete crushing failure. The TPT strands were modeled with CFCC properties, where linear elastic behavior was assumed until failure of the strand.

4.3 Verification of numerical study

Through the verification study, finite element models were developed for the tested control decked bulb T beams and to the bridge model. Model response such as deflection, strain distribution in the concrete, strain in the reinforcement, and ultimate load were compared with those obtained experimentally. The following subsections provide a detailed discussion for the finding of the verification study.

4.3.1 Control beams

Numerical models were generated for all experimental control beams. As shown in Figure 4.3-1, the numerical models consisted of the body of the beam, diaphragms, longitudinal reinforcement, stirrups, and supports. Four models representing Beams C-S-F-U, C-S-F-B, C-S-F-O, and S-S-F-U were generated and analyzed in flexural loading as shown in Figure 4.3-2, while one model for Beam C-C-F-B was generated and analyzed under shear loading as shown in Figure 4.3-3.

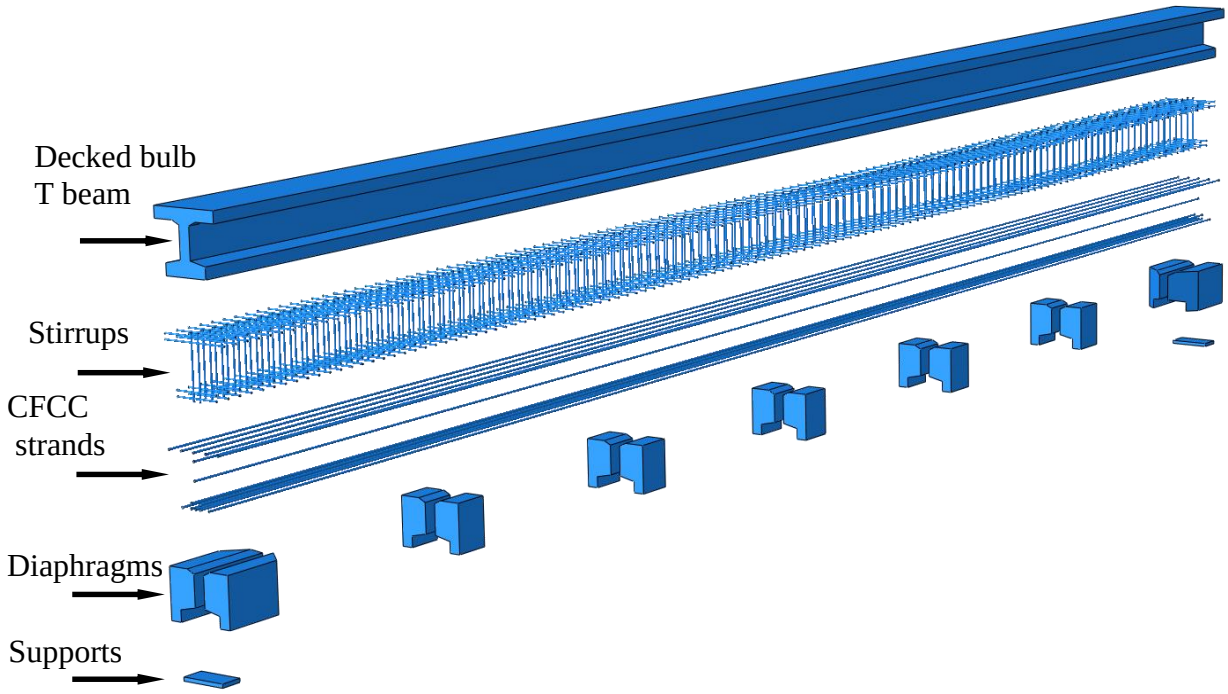

Figure 4.3-1 Details of numerical model

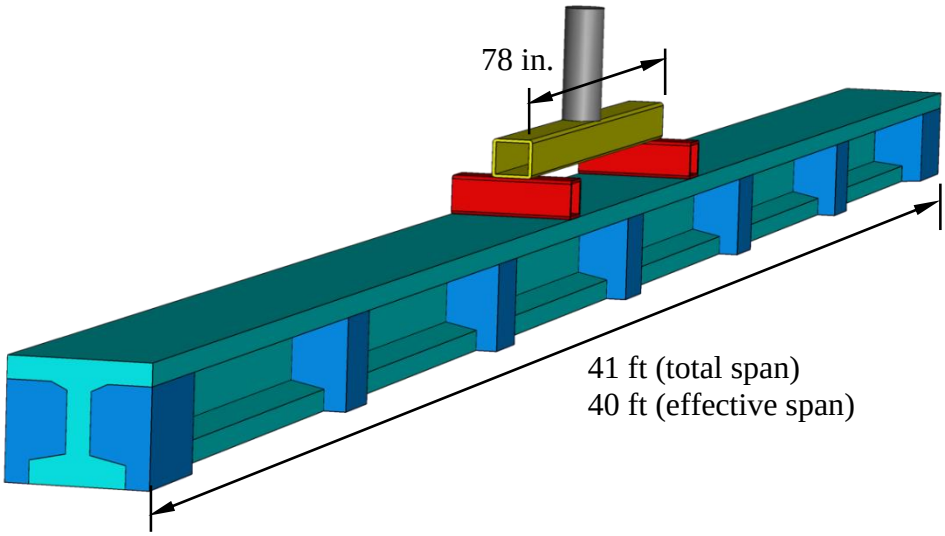

Figure 4.3-2 Models for control beams under flexural loading

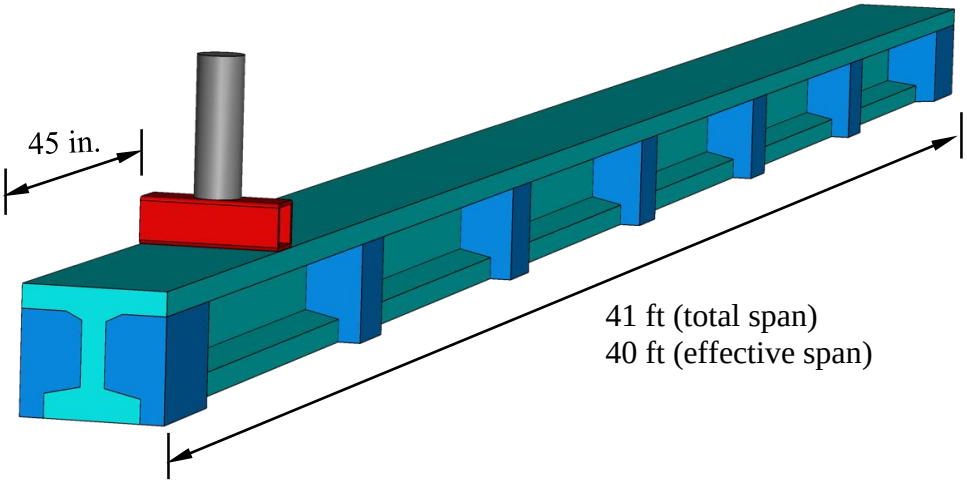

Figure 4.3-3 Model for a control beam with shear loading

4.3.1.1 Numerical model for Beam C-S-F-U

The concrete material in this control beam model was defined with a 28-day compressive strength of 9 ksi, tensile strength of 690 psi, and elastic modulus of 5,751 ksi. Both the modulus of elasticity and the tensile strength were adopted from AASHTO LRFD 2012 Sections 5.4.2.4 and C.5.4.2.7, respectively, while the compressive and tensile stress-strain curves (shown in Figure 4.3-5 and Figure 4.3-6) of the concrete were developed based on an analytical formula (Collins et al. 1993, Popovics et al. 1973, and Thorenfeldt et al. 1987). Normal-weight concrete was assumed with a self-weight of 0.15 kip/ft^3 and Poisson's ratio of 0.2. The beam was reinforced/prestressed with CFCC strands and steel stirrups every 4 in. The beam had a total span of 41 ft and effective span of 40 ft. The numerical model simulated the configuration and the reinforcement of the control beams with four bottom CFCC prestrssing strands and five top non-prestressing CFCC strands in addition to two non-prestressing strands through the depth of the web. The CFCC strands were defined in the model with an effective cross sectional area of 0.179 in.^{2}, a modulus of elasticity of 22,480 ksi, ultimate tensile strength of 375 ksi, and ultimate strain of 1.67%. Figure 4.3-4 shows the stress-strain curve for CFCC materials. The stirrups were modeled as truss elements with cross sectional area of 0.11 in.^{2} (No. 3 deformed steel bars) and were assigned the material properties of Grade 60 steel with a yield strength of 60 ksi, elastic modulus of 29,000 ksi, ultimate strength of 90 ksi, and ultimate strain of 0.05 as shown in Figure 4.3-7.

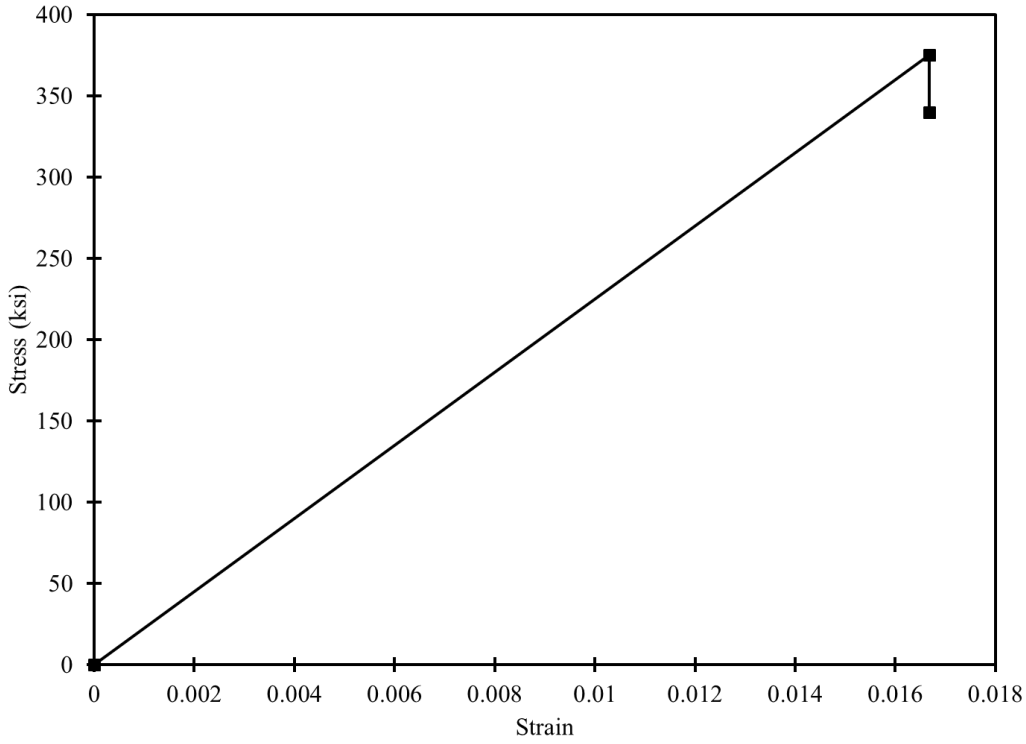

Figure 4.3-4 Stress-strain curve for CFCC strands

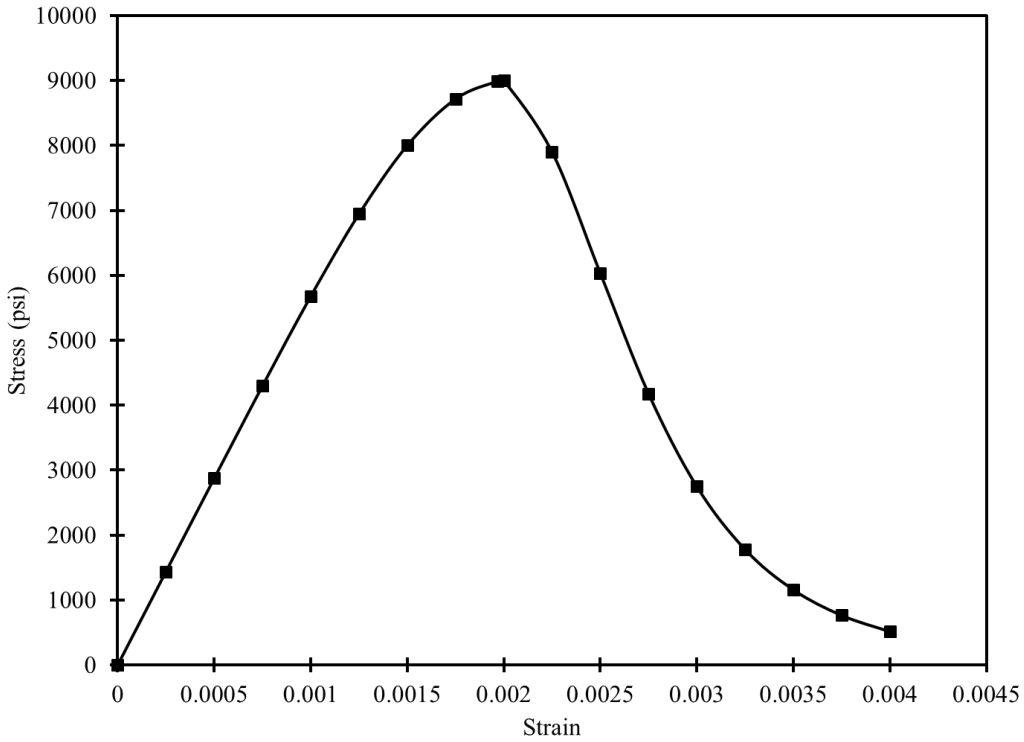

Figure 4.3-5 Compressive stress-strain curve for 9000-psi concrete

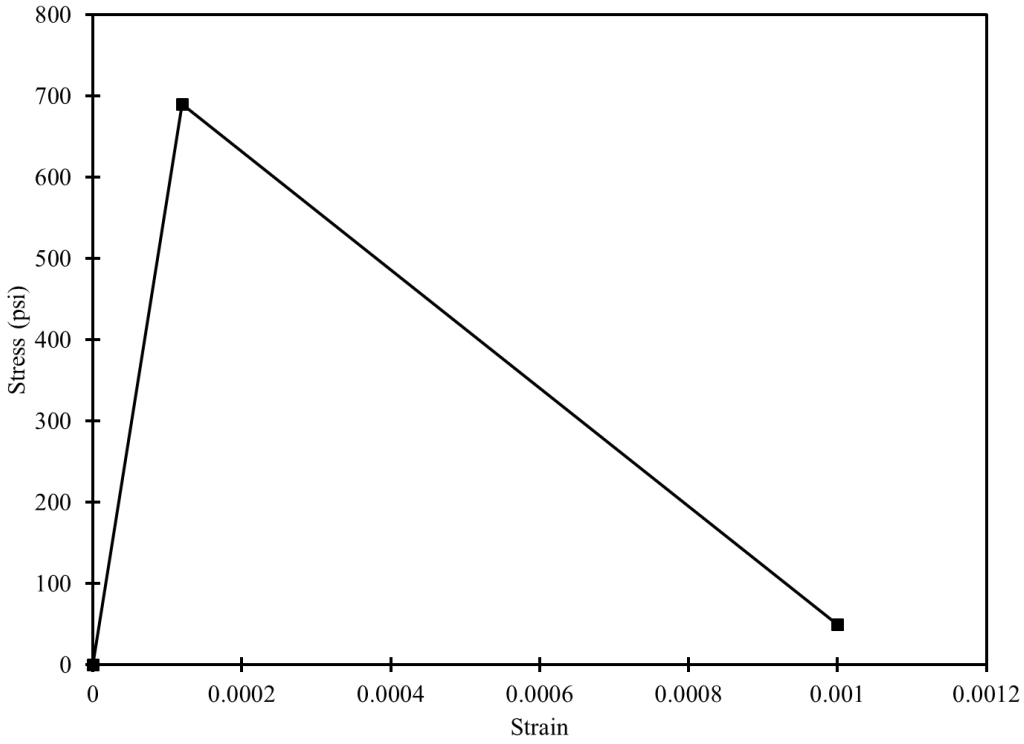

Figure 4.3-6 Tensile stress-strain relationship for 9000-psi concrete

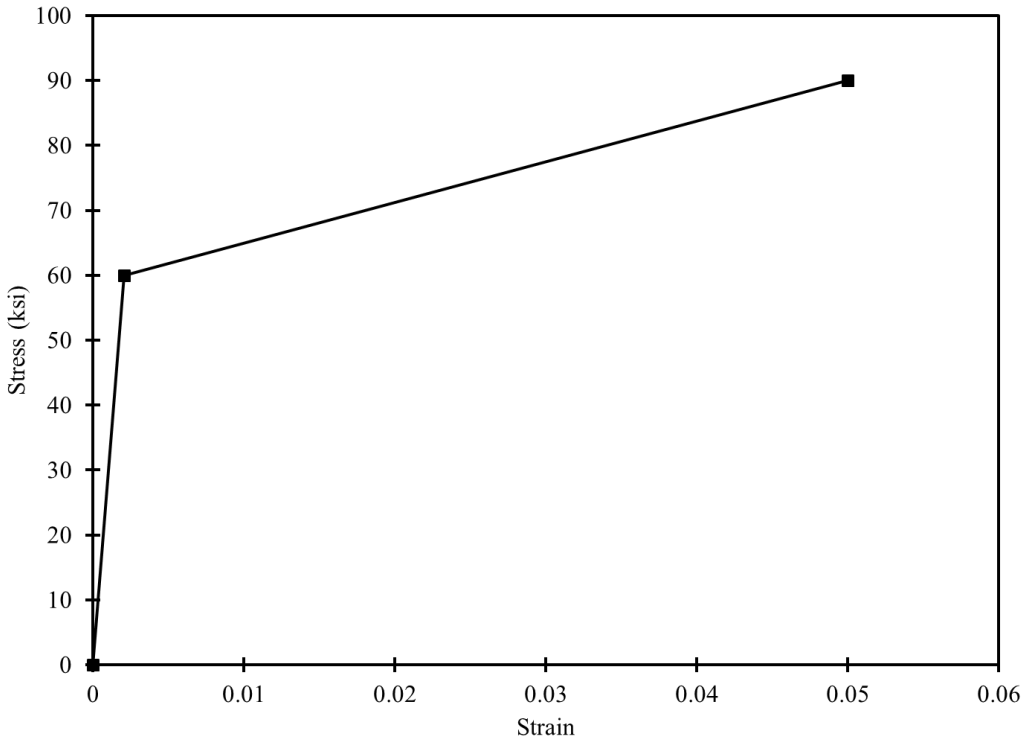

Figure 4.3-7 Idealized stress-strain curve for deformed steel bars, Grade 60

During the numerical analysis, the control beam is analyzed under flexural static load to failure. The load-deflection curves of the beam and the load-strain curves of the concrete and CFCC strands were compared with those obtained from the experimental study. The numerical model exhibited a cracking load of approximately 12.0 kip, which matched the cracking load of the experimental beam. The numerical model showed a maximum load carrying capacity of 33.5 kip with a corresponding deflection at failure of 15.86 in. However, the envelope of the experimental load cycles showed a maximum load 33.1 kip and then the load dropped to 31.4 kip with a corresponding deflection of 16 in. The difference between the numerical and experimental results was approximately 2%. Figure 4.3-8 shows the load deflection curves obtained numerically and experimentally. The experimental load-deflection curve is the envelope for all the load cycles. As shown in the figure, there is an overall fair agreement between the numerical and experimental responses of this control beam. The load-strain curves for the concrete and the CFCC strands are shown in Figure 4.3-9 and Figure 4.3-10, respectively. Close agreement was observed between the numerical and experimental strain reading with a difference of approximately 6 % in concrete strain readings and 9 % in CFCC strain readings at failure.

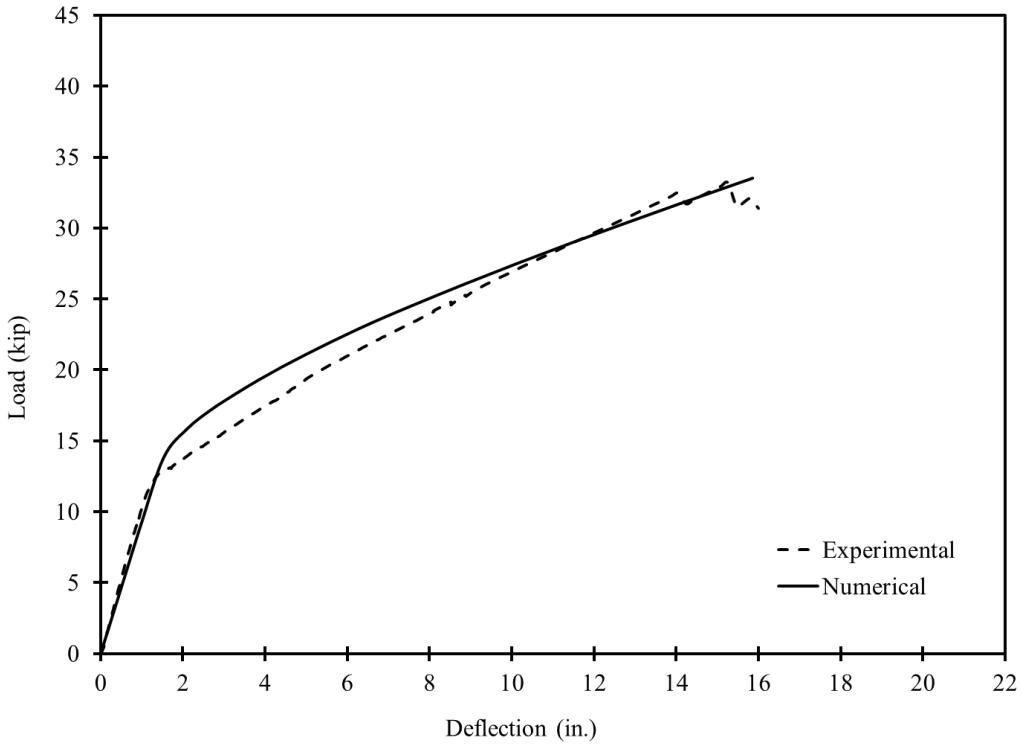

Figure 4.3-8 Numerical vs. experimental load-deflection curves of Beam C-S-F-U

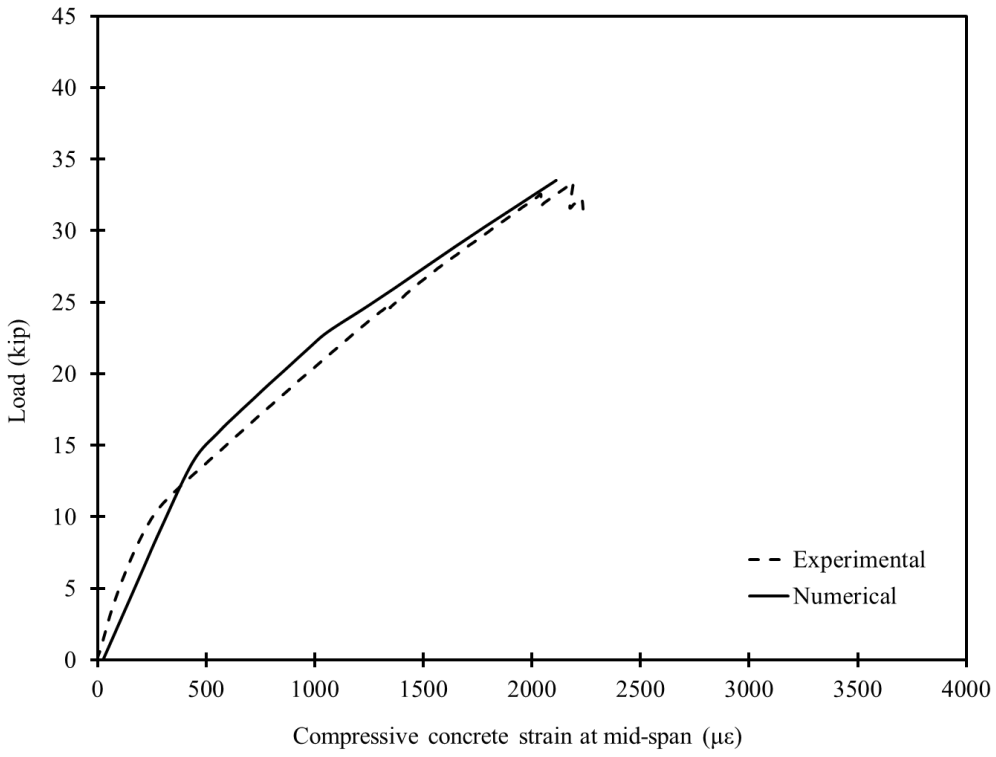

Figure 4.3-9 Numerical vs. experimental load-concrete-strain curves of Beam C-S-F-U

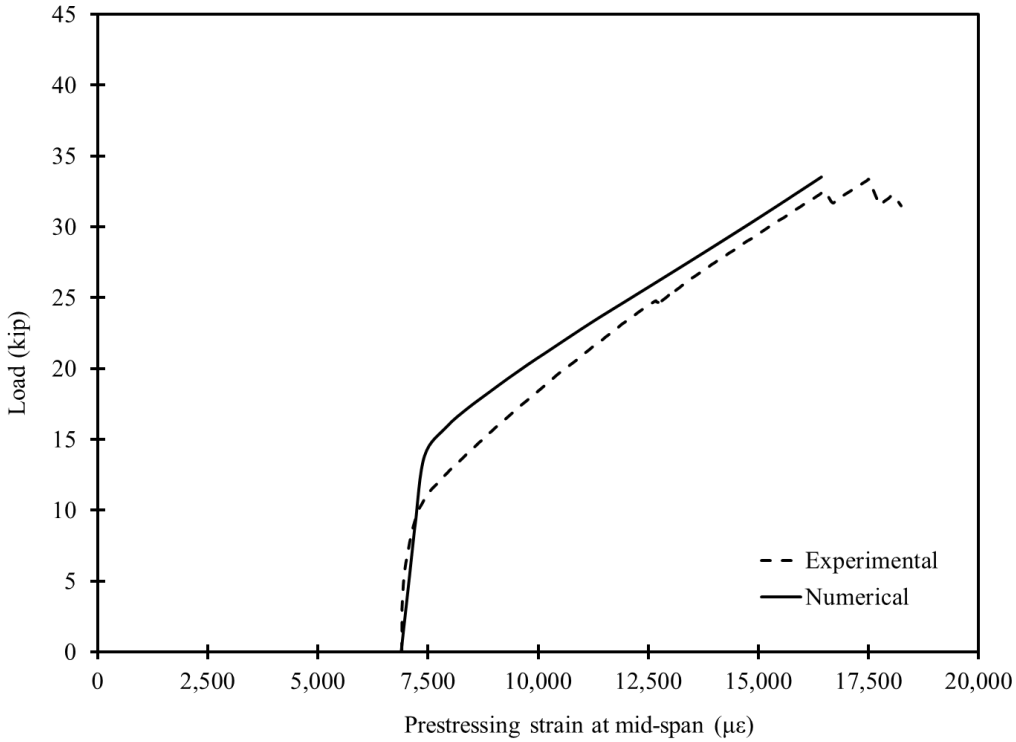

Figure 4.3-10 Numerical vs. experimental load-prestressing-strain of Beam C-S-F-U

4.3.1.2 Numerical model for Beam C-S-F-B

The modeling and analysis approach for this beam was similar to the previous beam with the exception that the concrete strength was slightly lower. Based on the 28-day uni-axial compressive strength, the concrete compressive strength averaged 7,684 psi, and on the day of the test, the concrete compressive strength slightly exceeded 8,000 psi. Therefore, the material properties and stress-strain curves for 8,000-psi concrete was adopted for this beam. It should be noted that this was the only beam that experienced a slightly lower concrete strength. All other beams including those for the bridge model experienced a concrete strength with the average of approximately 9,000 psi. The modulus of elasticity for the concrete was taken as 5,422 ksi, while the direct tensile strength was taken as 650 psi. Figure 4.3-11 shows the adopted compressive stress-strain relationship for the 8,000-psi concrete.

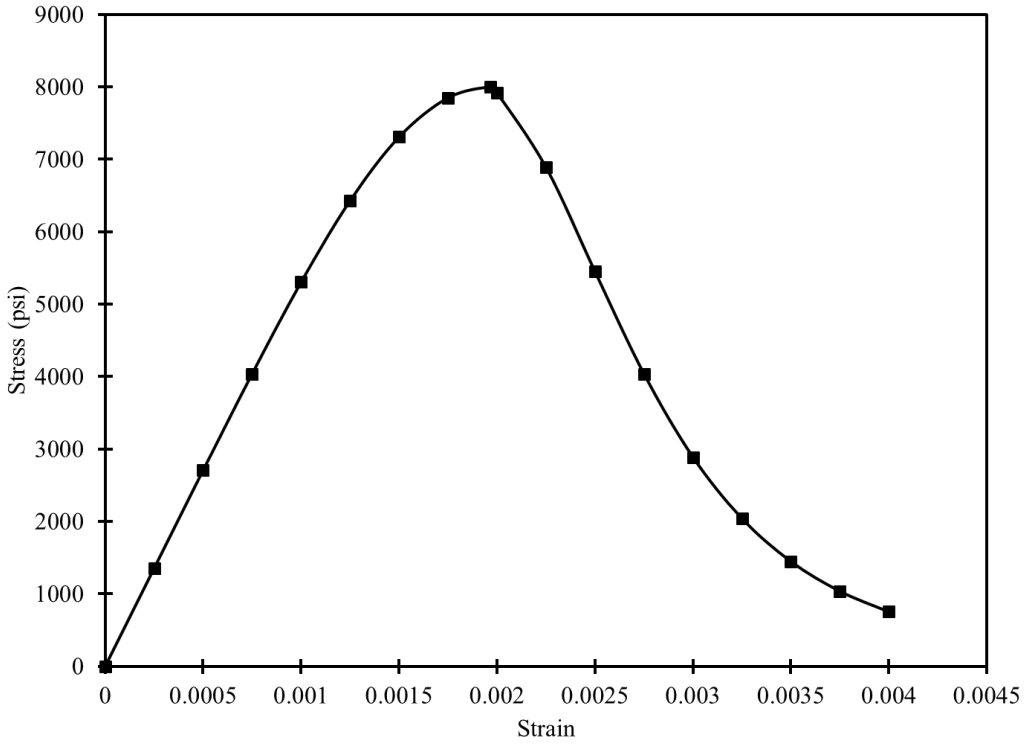

Figure 4.3-11 Compressive stress-strain curve for 8,000-psi concrete

The results from the numerical model are in good agreement with those from the experimental investigation. As shown in Figure 4.3-12, the numerical model predicted the failure at a load level of 41.31 kip with a corresponding deflection of 17.63 in. The experimental test showed an ultimate load of 40.81 kip with a corresponding deflection of 16.43 in. The difference between the

numerical and experimental failure load was approximately 1.2%, while the difference in the deflection at failure was approximately 7%.

Similarly, there is a good agreement between the numerically predicted concrete strain and the experimentally recorded strain as shown in Figure 4.3-13. The numerical model predicted the failure of the beam at a concrete strain of 2,900 με, while the maximum experimentally recorded strain was around 3,270 με. On the other hand, the recoding of the strain in the prestressing strands was interrupted early during the experimental testing but the data collected shows a good agreement with the numerically predicted prestressing strain as shown in Figure 4.3-14. The numerical analysis predicted the failure of the beam at prestressing strain of 16,143 με.

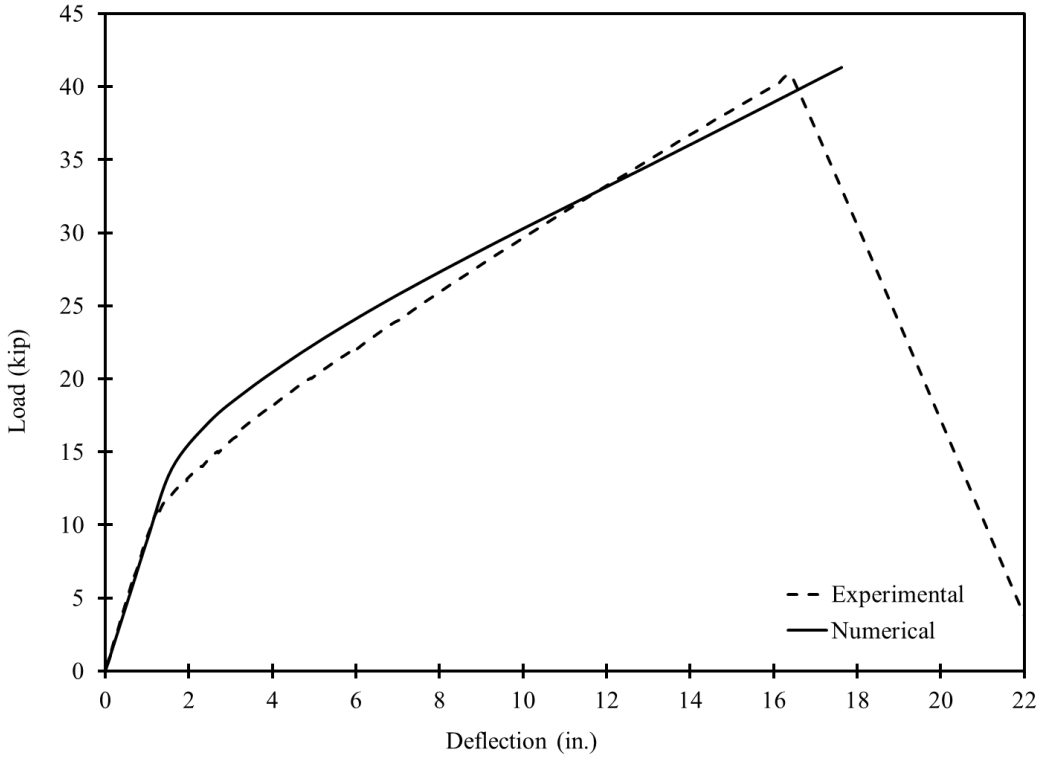

Figure 4.3-12 Numerical vs. experimental load-deflection curves of Beam C-S-F-B

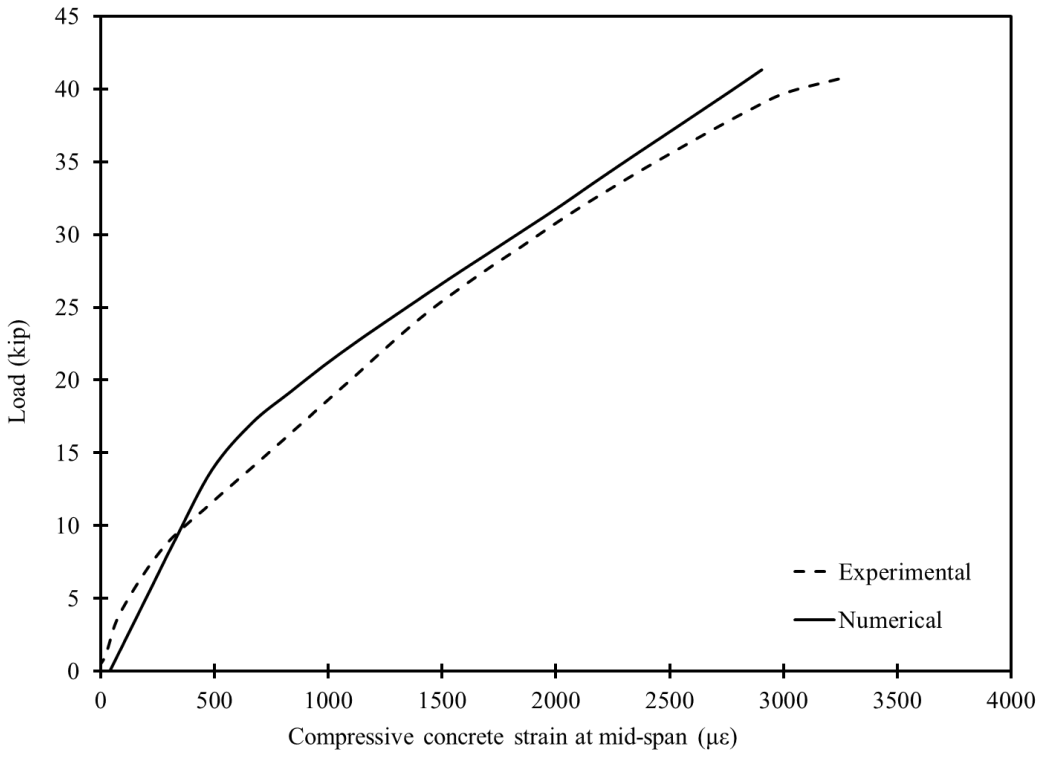

Figure 4.3-13 Numerical vs. experimental load-concrete-strain curves of Beam C-S-F-B

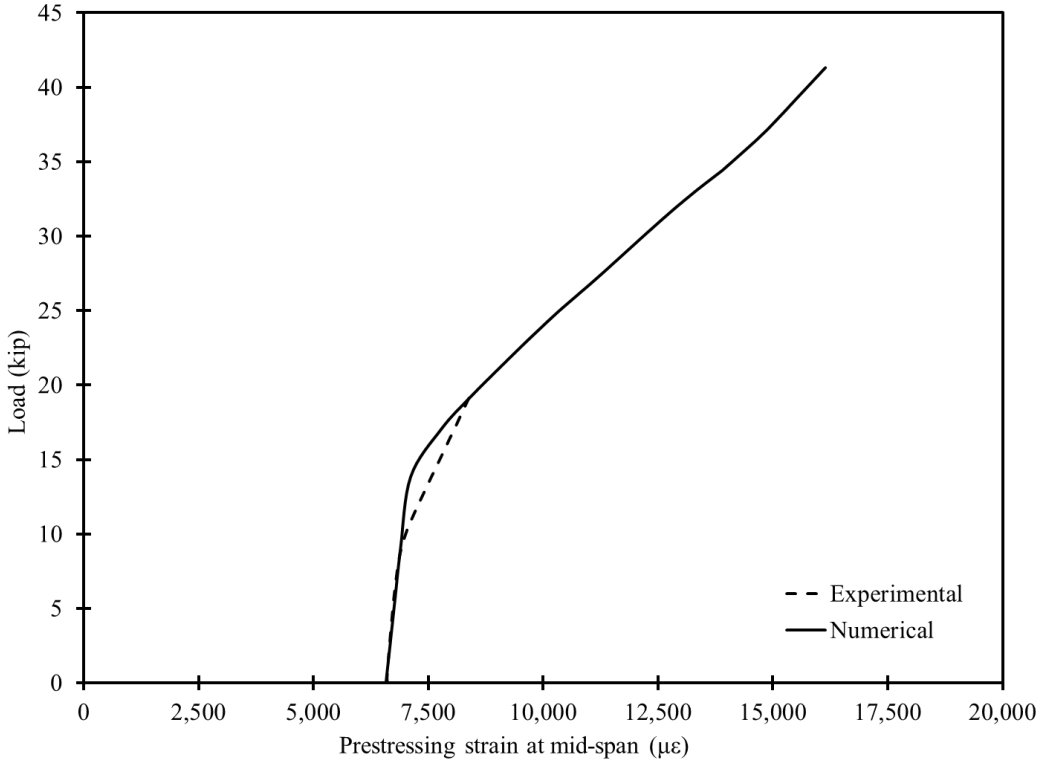

Figure 4.3-14 Numerical vs. experimental load-prestressing-strain curves of Beam C-S-F-B

4.3.1.3 Numerical model for Beam C-S-F-O

Similar to previous beams, a numerical model was generated for Beam C-S-F-O and analyzed under four-point loading. The results from the numerical analysis were compared with those obtained experimentally as shown in Figure 4.3-15 through Figure 4.3-17. The observed cracking load was approximately 12 kip, while the maximum load was approximately 43.7 kip with a corresponding deflection of 14.61 in. The concrete strain obtained numerically was slightly different from that recorded using strain gages, mainly because of the variation in the stress-strain behavior of the concrete. The concrete in the numerical analysis was defined with an ideal concrete stress-strain curve, where for a 9000-psi concrete, it was assumed that the strain corresponding to a stress of 9000 psi was approximately 2,000 με. After that, the concrete was assumed to lose strength with a gradual increase in strain until failure at a strain of 3,000 με. Therefore, the numerical load-strain relationship followed the pre-defined pattern exactly as shown in Figure 4.3-16. At the maximum load, the concrete strain was slightly higher than 2,000 με but it tended to increase with a slight decrease in the load until failure occurred at a concrete strain of 3,000 με. This exact behavior was not captured by the strain gages in the experimental investigation. On the other hand, Figure 4.3-17 shows the numerical vs. experimental prestressing strain in the CFCC strands. As shown in the figure, both the experimental and numerical results indicated a prestressing strain of approximately 13,600 με at failure, which confirmed the compression failure of the beam. Overall, there was good agreement between the numerical and experimental results. At failure, the differences in load, deflection, strain in concrete, and strain in prestressing strands were approximately 0.2, 1.9, 1.6, and 0.4%, respectively.

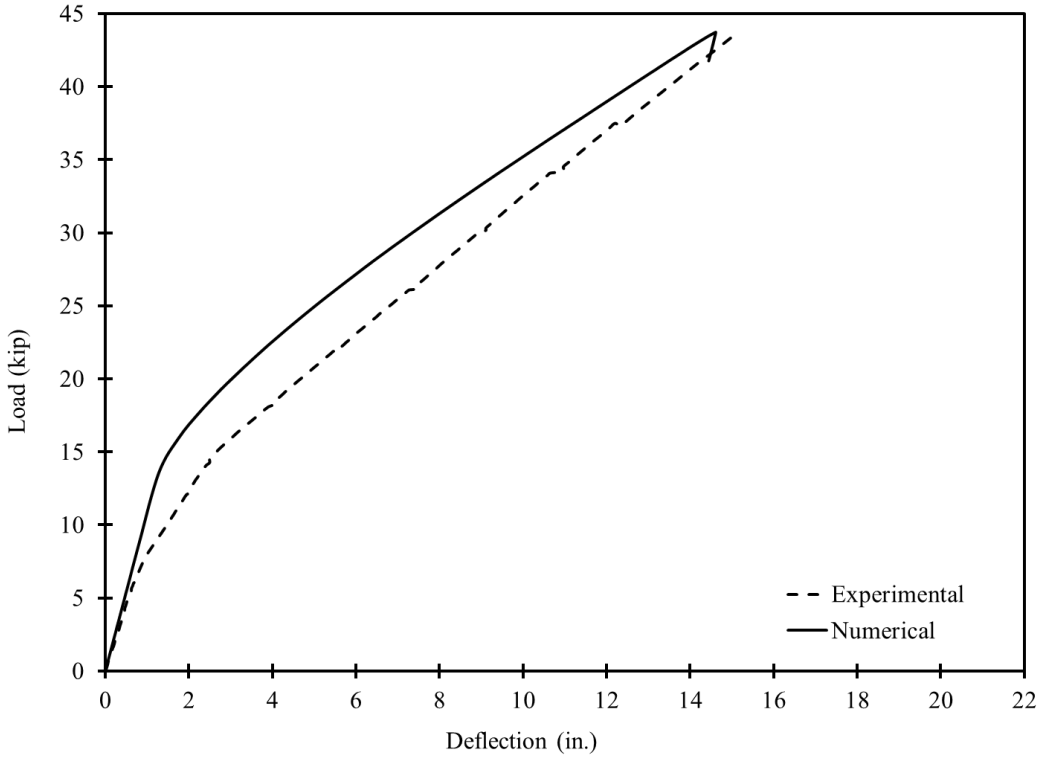

Figure 4.3-15 Numerical vs. experimental load-deflection curves of Beam C-S-F-O

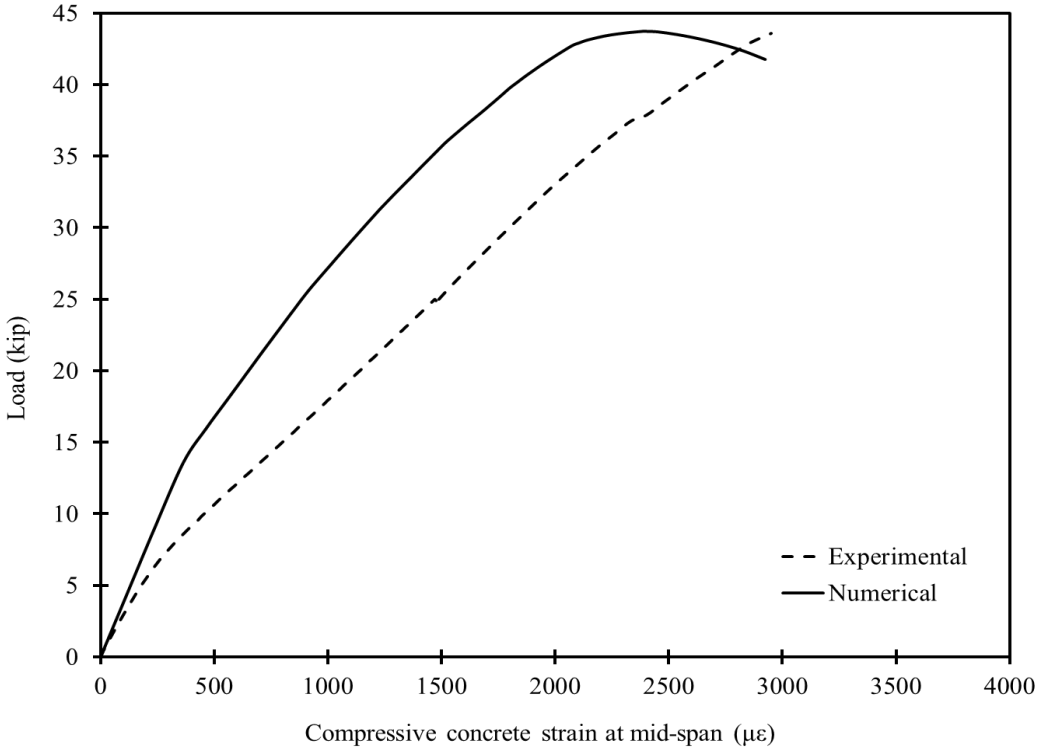

Figure 4.3-16 Numerical vs. experimental load-concrete-strain curves of Beam C-S-F-O

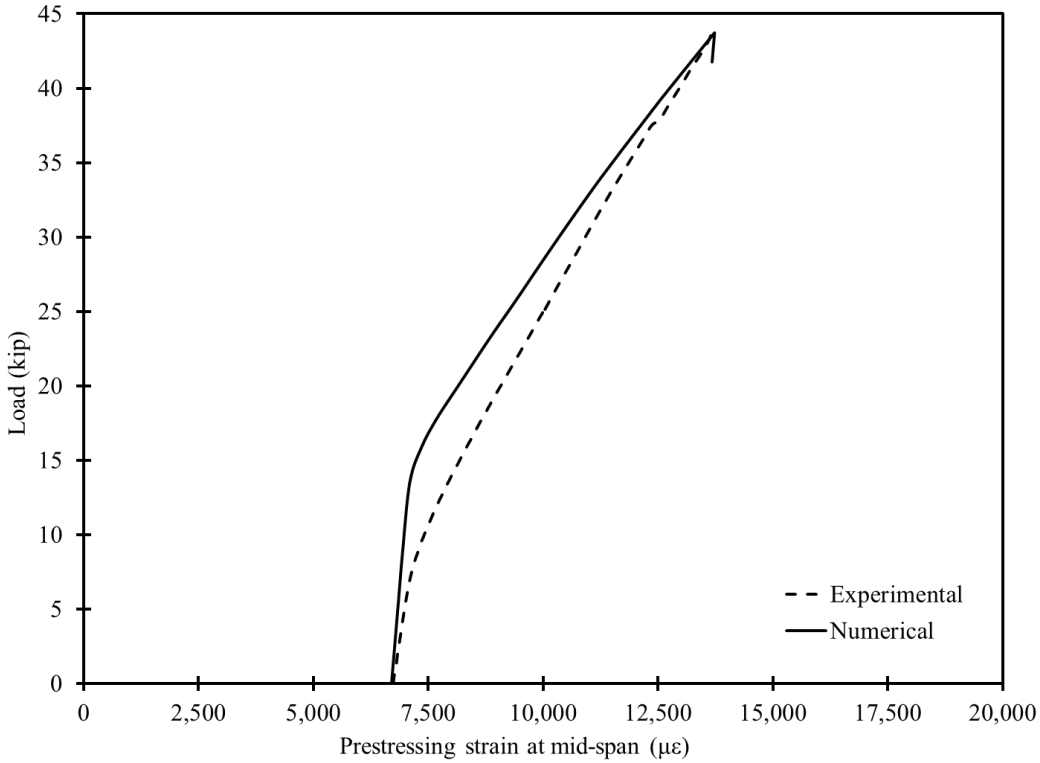

Figure 4.3-17 Numerical vs. experimental load-prestressing-strain curves of Beam C-S-F-O

4.3.1.4 Numerical model for Beam S-S-F-U

This control beam was reinforced with 7-wire low relaxation steel strands with a diameter of 0.6 in. The non-prestressed reinforcement was composed of deformed steel bars, Grade 60. Therefore, in the numerical modeling, the prestressing strands were assigned the material properties of steel strands with modulus of elasticity of 28,500 ksi, yield strength of 230 ksi, and ultimate strength of 270 ksi with a corresponding ultimate strain of approximately 5%. Figure 4.3-18 shows the idealized stress-strain curve for low-relaxation steel strands.

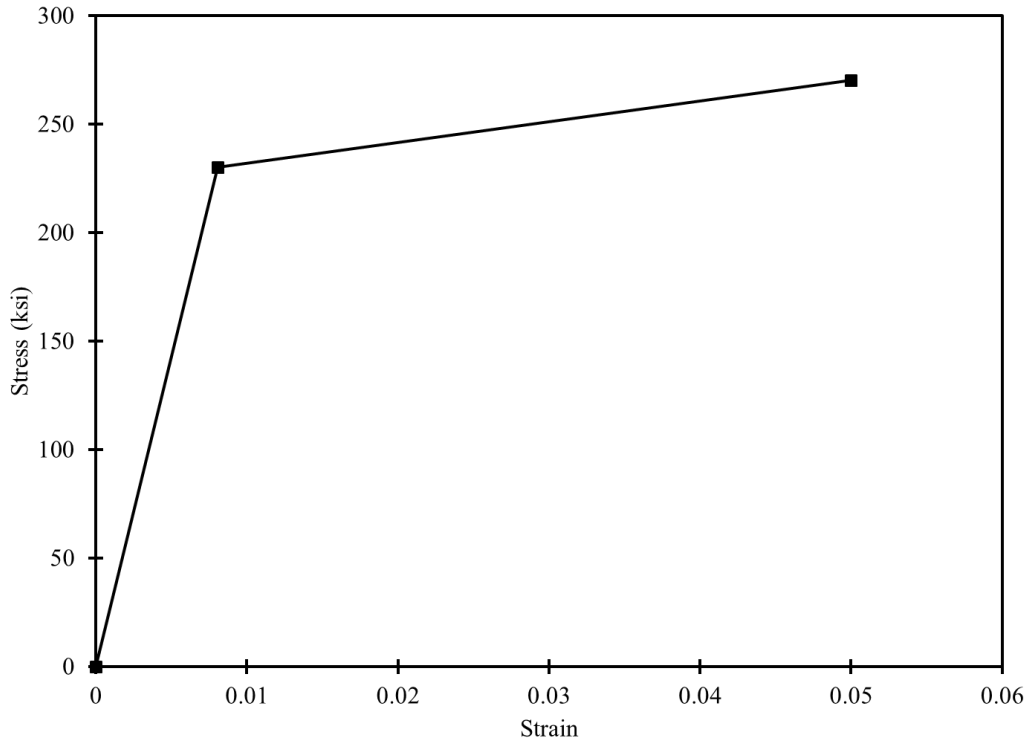

Figure 4.3-18 Idealized stress-strain curve for low-relaxation steel strands

As shown in Figure 4.3-19, Figure 4.3-20, and Figure 4.3-21, the deflection, concrete strain, and prestressing strain values from the numerical analysis are in good agreement with the values obtained experimentally. The numerical analysis shows a maximum load of 38.77 kip with a corresponding deflection at failure of 17.5 in, while the experimental testing shows a maximum load of 39.4 kip with a corresponding deflection of 19.14 in. The maximum experimental recorded strain in the concrete was approximately 2,615 με, which also matched the maximum numerically calculated concrete strain at failure. The experimental strain in the prestressing strands at failure was approximately 18,784 με, while the numerically predicted value is approximately 19,184 με.

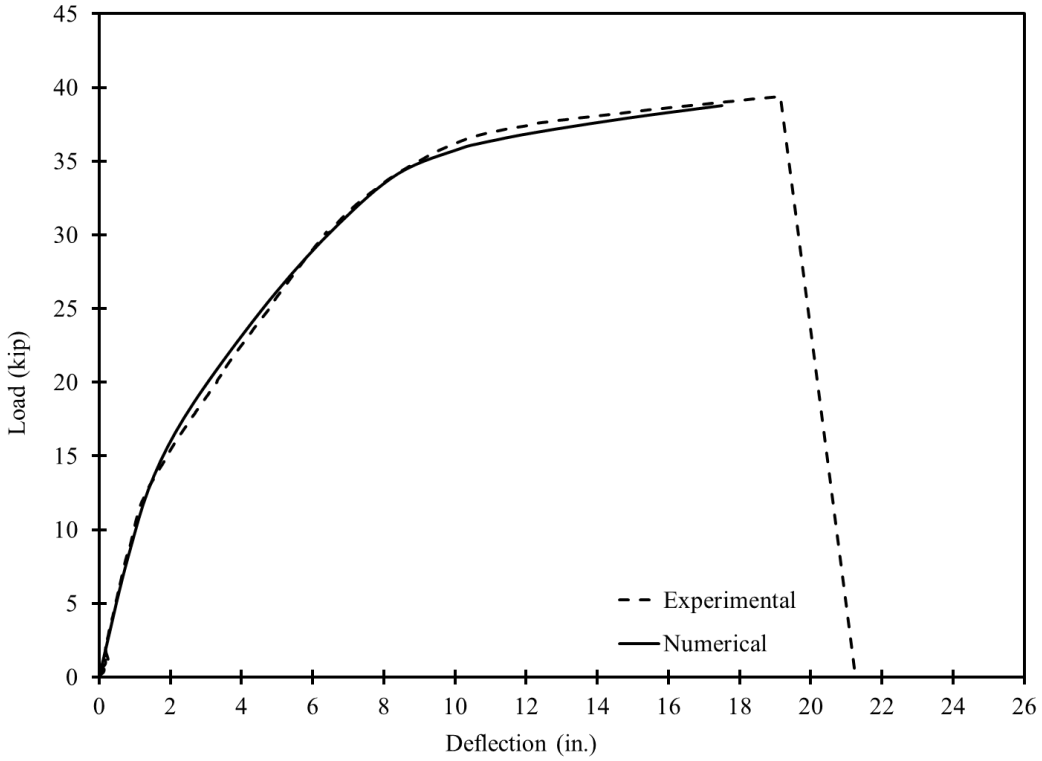

Figure 4.3-19 Numerical vs. experimental load-deflection curves of Beam S-S-F-U

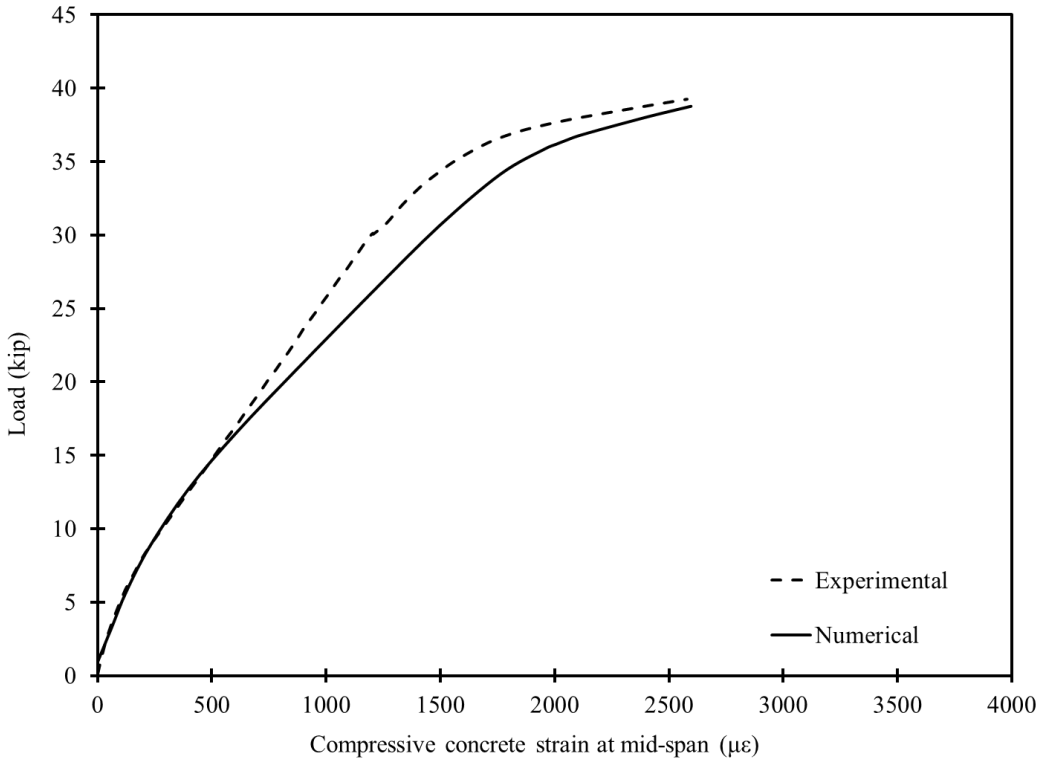

Figure 4.3-20 Numerical vs. experimental load-concrete-strain curves of Beam S-S-F-U

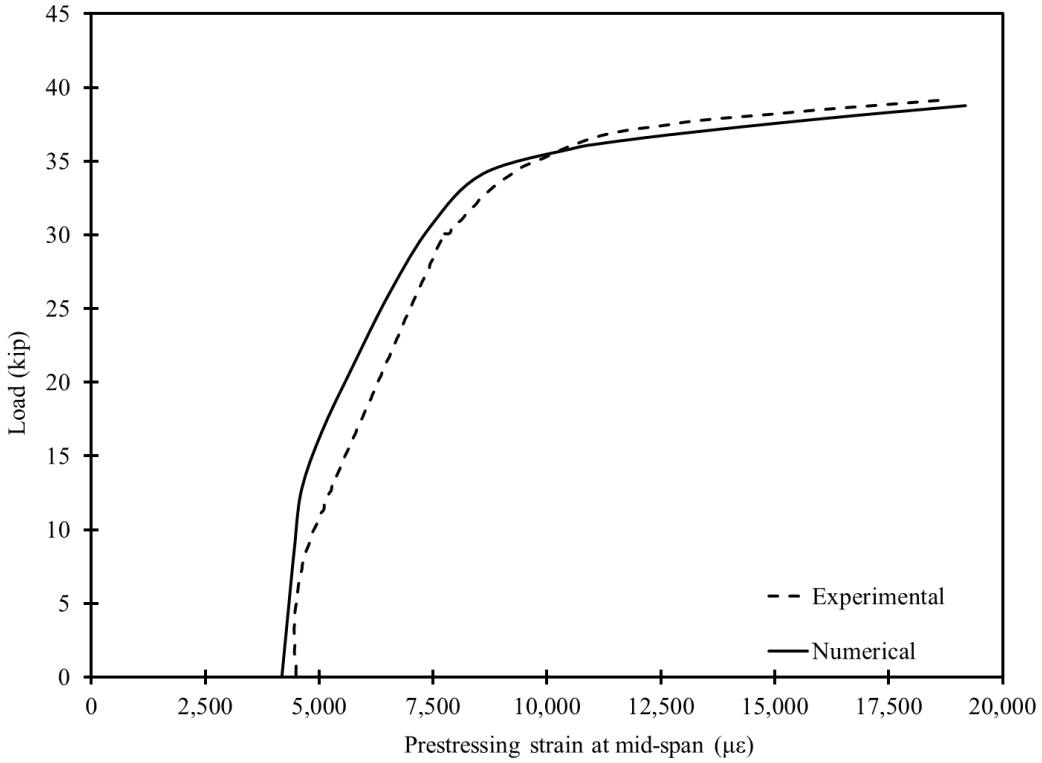

Figure 4.3-21 Numerical vs. experimental load-prestressing-strain curves of Beam S-S-F-U

4.3.1.5 Numerical model for Beam C-C-S-B

This numerical model for this control beam was analyzed under shear loading with a shear span of 45 in. The concrete elements were assigned the material properties of 9,000-psi concrete, while the stirrups were assigned the material properties of CFCC with an elastic modulus of 21,030 ksi and an ultimate strength of 400 ksi with a corresponding ultimate strain of 1.9%. Properties of CFCC stirrups were adopted from a material data sheet tested and provided by the manufacturer. The CFCC stirrups had a diameter of 0.41 in. with effective cross sectional area of approximately 0.09 in^2.

As shown in Figure 4.3-22 and Figure 4.3-23, the numerically-predicted deflection under the loading point and at the mid-span matches those recorded experimentally with a good agreement from the beginning of the loading to failure. The predicted failure load from the numerical analysis is around 80.88 kip with a corresponding deflection of 3.09 in. under the load and 6.08 in. at the mid-span. The experimental results showed that the ultimate load was around 78.4 kip with a corresponding deflection of 3.18 in. under the load and 5.77 in. at the mid-span.

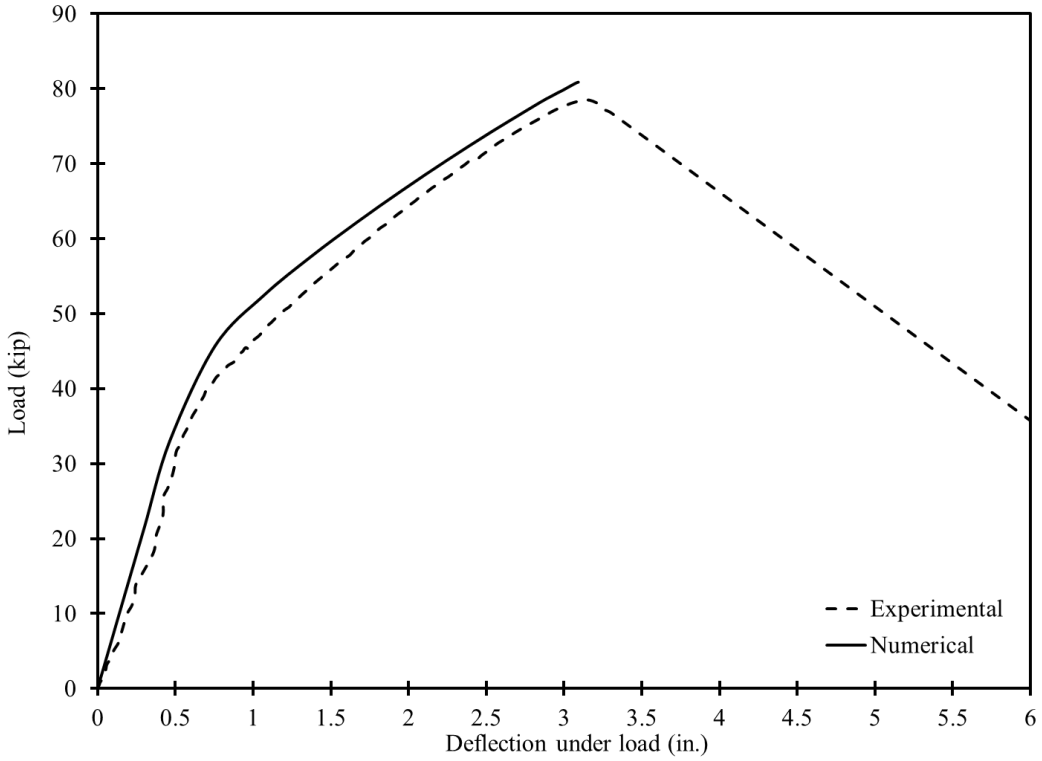

Figure 4.3-22 Numerical vs. experimental load-deflection curves of Beam C-C-S-B

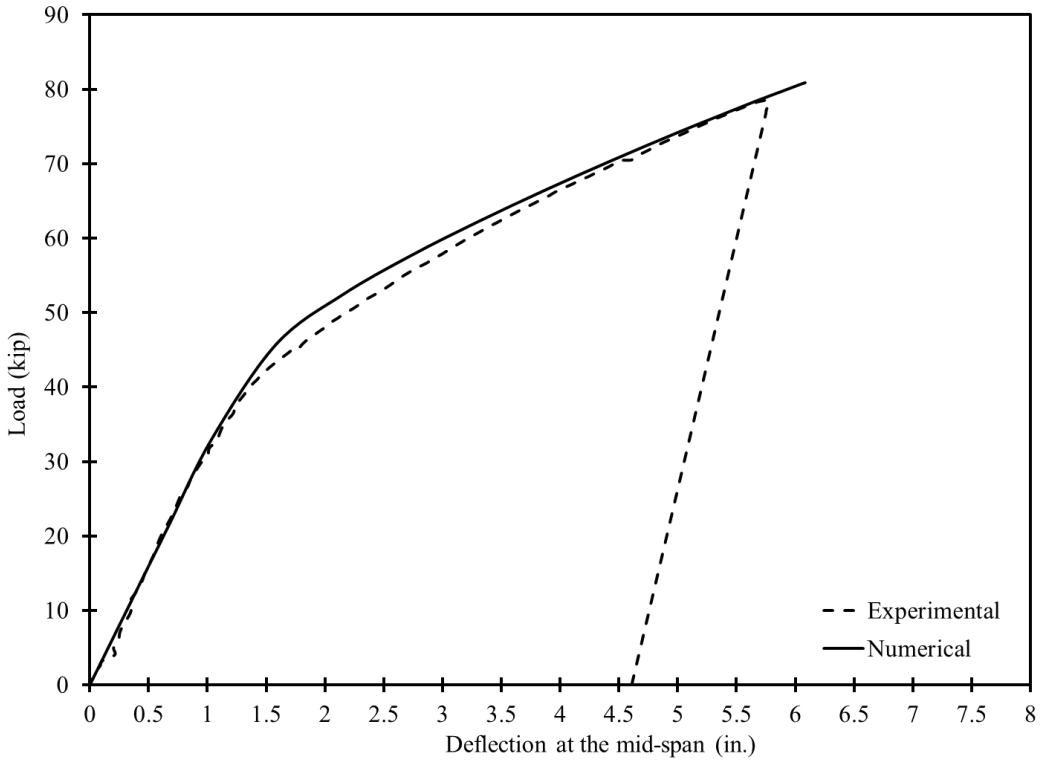

Figure 4.3-23 Numerical vs. experimental load-mid-span-deflection curves of Beam C-C-F-B

The numerical and experimental strain readings in the concrete top flange surface near the loading are compared in Figure 4.3-24. The numerical model predicted a concrete strain of 2,220 με at failure, while the maximum concrete strain that was recorded experimentally is approximately 2,670 με. Similarly, the numerical strain in the longitudinal prestressing strands was compared with that obtained experimentally as shown in Figure 4.3-25. Good agreement is observed in the strain readings with the numerical analysis predicting a maximum prestressing strain of 11,687 με and the experimental recording showing a maximum strain of 12,276 με.

The strain in the CFCC stirrups was obtained numerically and was plotted against the experimental strain in different stirrups. Figure 4.3-26 shows an example for the comparison between the numerical and experimental stirrup strain. As shown in the figure, two trends of experimental strain readings are observed; one trend represented stirrups intercepted by diagonal cracks for the first time (strain reading of S6-B), while the other trend represented the strain in stirrups intercepted by diagonal shear cracks during previous load cycles (strain reading of S3-T). The location of the strain gages on the stirrups is shown in Figure 4.3-27, where S3 is the third instrumented stirrup in the shear span from the left and S6 is the sixth instrumented stirrup. The letters T refers to the top strain gage and the letter B refers to the bottom strain gage on the stirrup. Since no load cycles were performed in the numerical analysis, the predicted strain in the stirrups is in close agreement with the strain in stirrups not intercepted by cracks during previous load cycles.

Finally, the numerical model accurately predicted the failure mode under the shear loading. As shown in Figure 4.3-28, the failure of the numerical model occurred due to excessive strain and deformation in the concrete elements of the web of the beam and to a lesser extent in the top flange, which matched the failure mode observed during the experimental test.

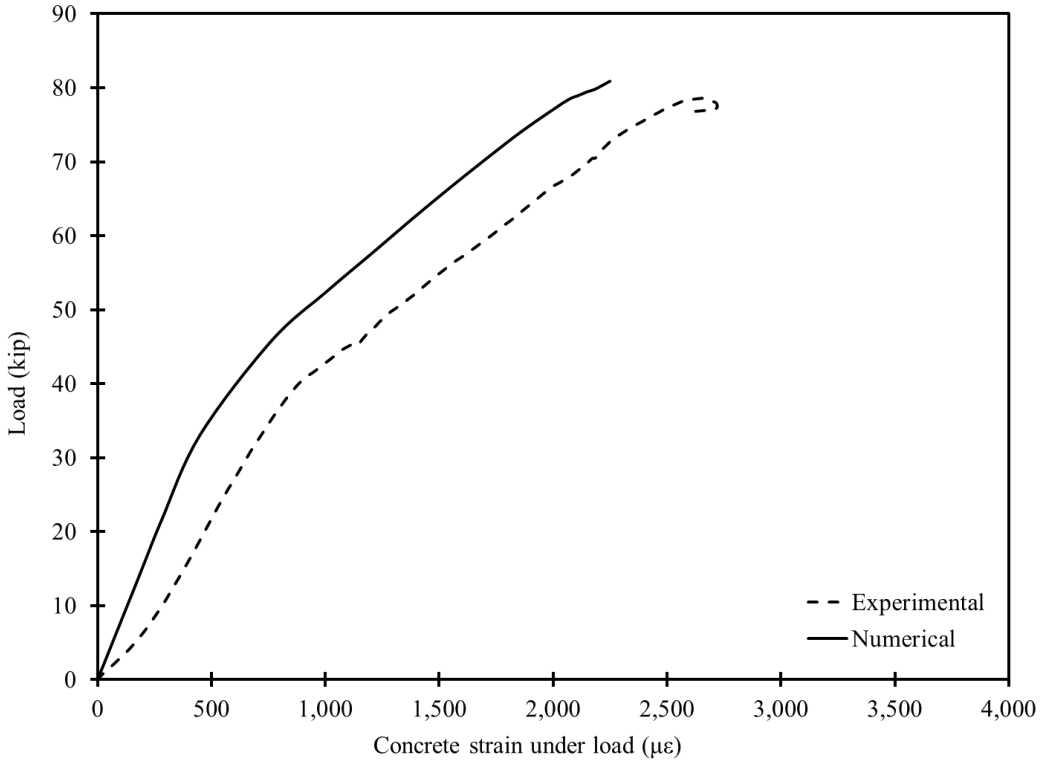

Figure 4.3-24 Numerical vs. experimental load-concrete-strain curves of Beam C-C-F-B

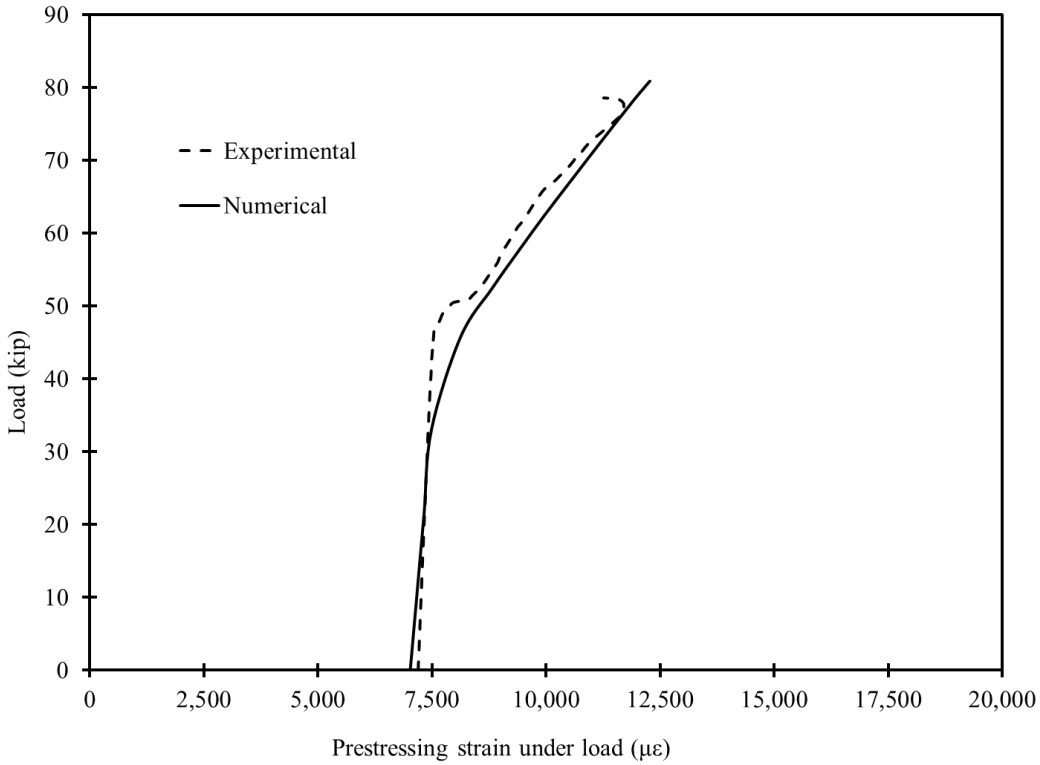

Figure 4.3-25 Numerical vs. experimental load-prestressing-strain curves of Beam C-C-F-B

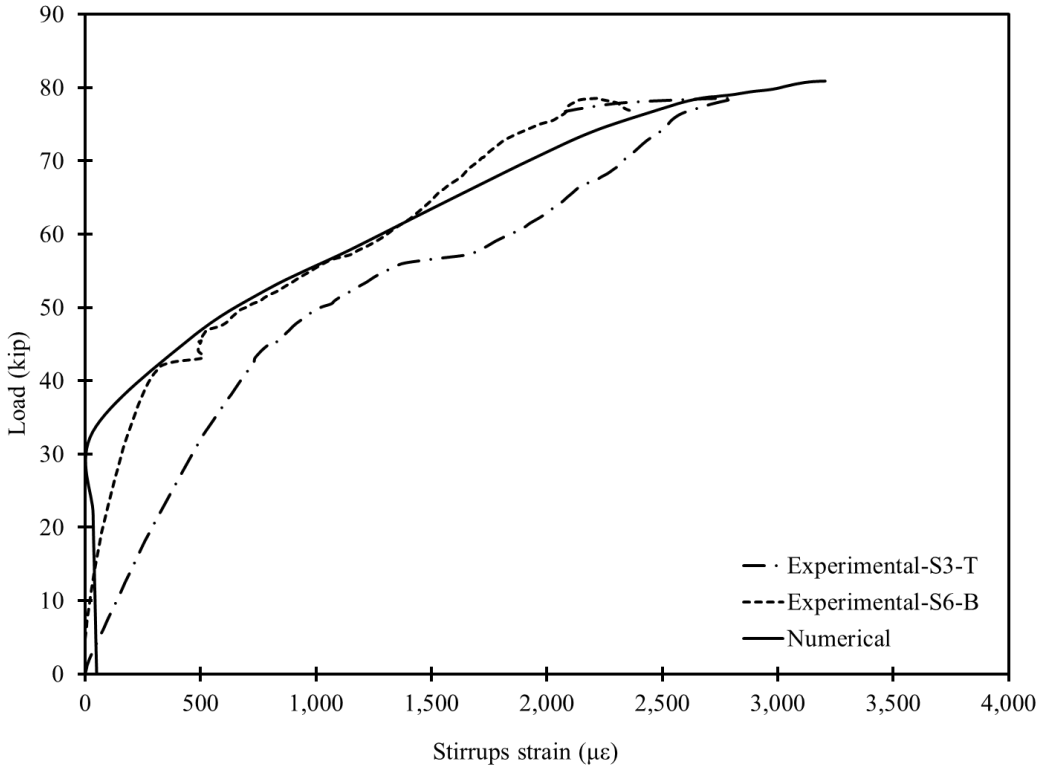

Figure 4.3-26 Numerical vs. experimental load-stirrup-strain curves of Beam C-C-F-B

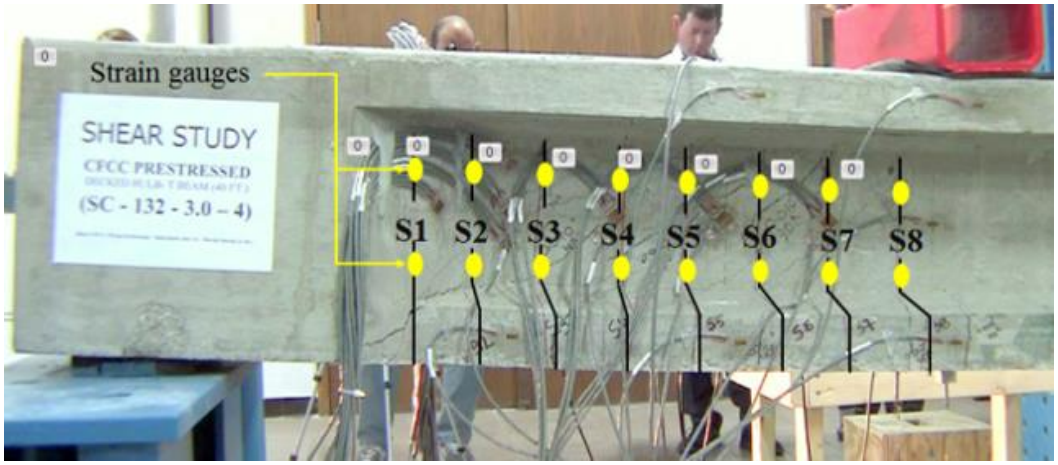

Figure 4.3-27 Nomenclature of strain gages in Beam C-C-S-B

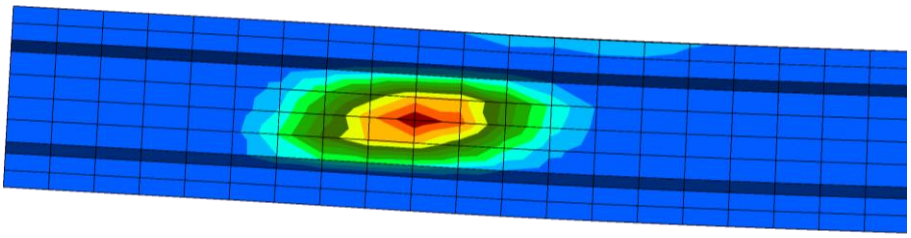

Figure 4.3-28 Shear failure simulation in the numerical model

4.3.2 Bridge model

A numerical model was generated and analyzed for the bridge model under service, post-cracking, and strength limit states. As shown in Figure 4.3-29 through Figure 4.3-31, the numerical analysis depicted with good accuracy the response of the bridge model under service loads of 15 and 30 kip at the mid-span of exterior, interior, and intermediate beams. In addition, and similar to the experimental loading scenario, the numerical model was analyzed under four-point loading until flexural cracks developed and then was analyzed under a single point load of 60 kip on the exterior, interior, and intermediate beams. The numerically obtained deflection values under the load of 60 kip were plotted against those recorded experimentally. The maximum difference between the numerical and experimental results was approximately 8%.

After completing the service and post-cracking limit states analysis, the numerical model was analyzed with the exterior beam loaded under four-point loading (shear key test). The deflection from this phase of analysis is also shown in Figure 4.3-29 at load levels of 80 and 90 kip. At both load levels, the numerical model exhibited a cracking pattern similar to that observed experimentally.

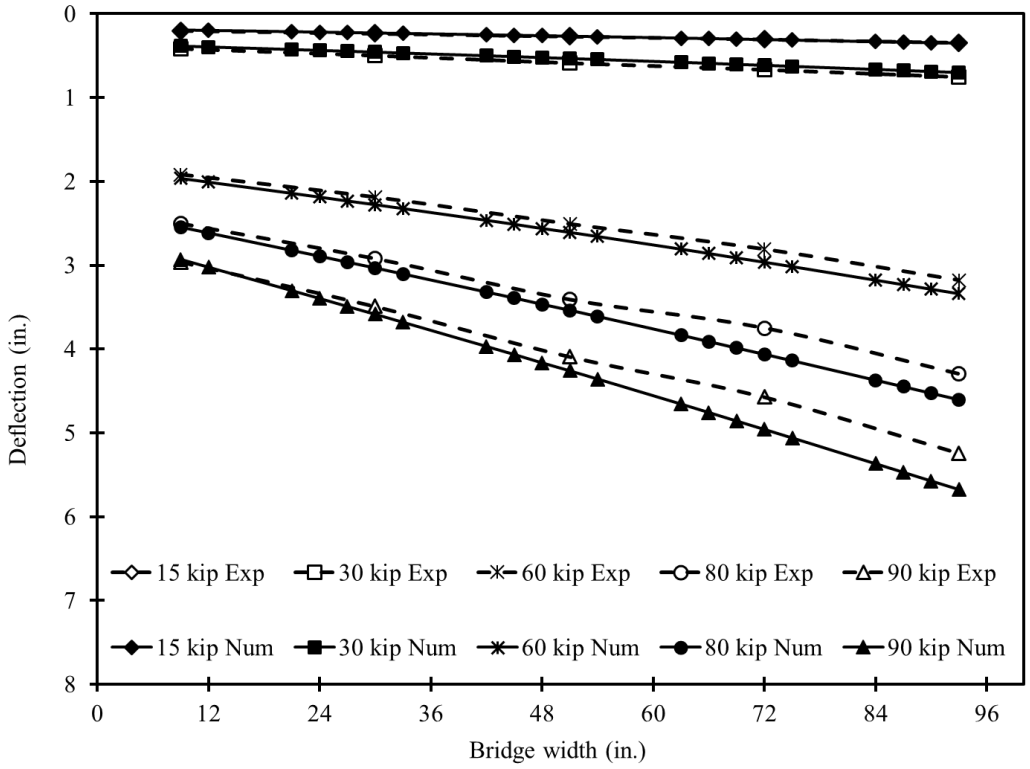

Figure 4.3-29 Numerical vs. experimental deflection curves with loads on exterior beam

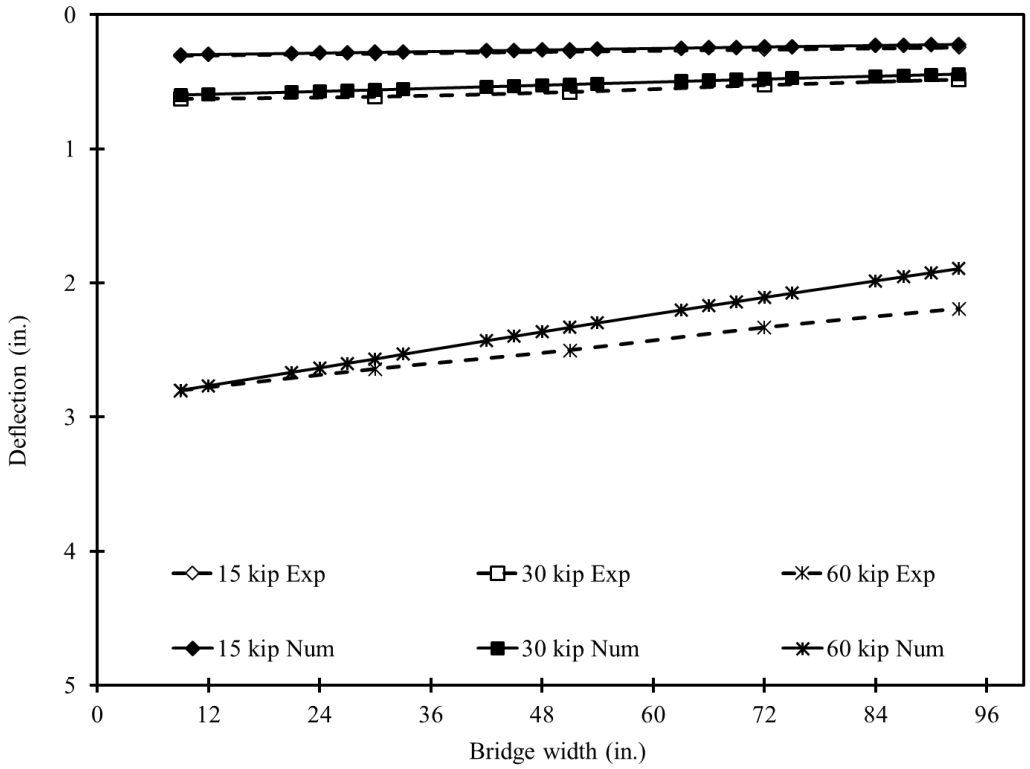

Figure 4.3-30 Numerical vs. experimental deflection curves with loads on interior beam

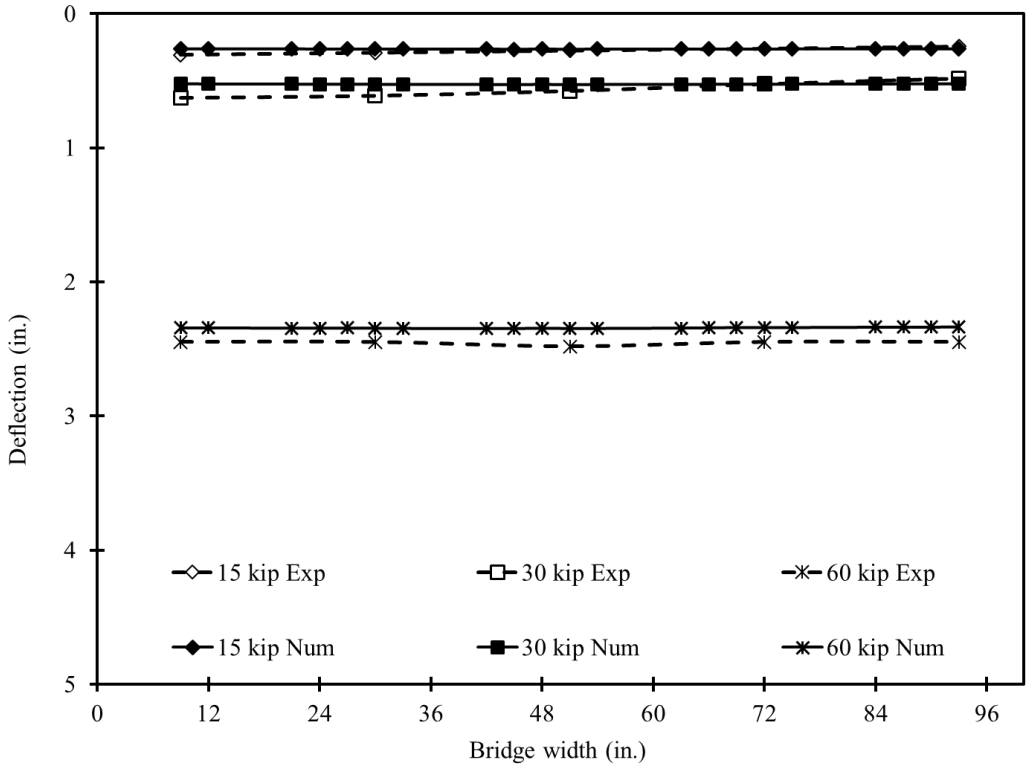

Figure 4.3-31 Numerical vs. experimental deflection curves with loads on intermediate beam

The final stage of the analysis included evaluating the response of the numerical model under strength limit state by performing the analysis with the intermediate beam loaded under a four-point loading setup to failure. Similar to control beams, the response of the bridge model was evaluated through the deflection, concrete strain, and prestressing strain. Figure 4.3-32 through Figure 4.3-34 show the response of the numerical model versus the experimentally recorded data. The numerical analysis showed a failure load of 219.6 kip with a corresponding deflection of 16.64, 16.61, and 16.56 in. under the intermediate, interior, and exterior beams respectively. At the intermediate beam, the concrete strain at the maximum load was approximately 2,800 με, while the strain in the prestressing strands reached the ultimate strain of 16,000 με.

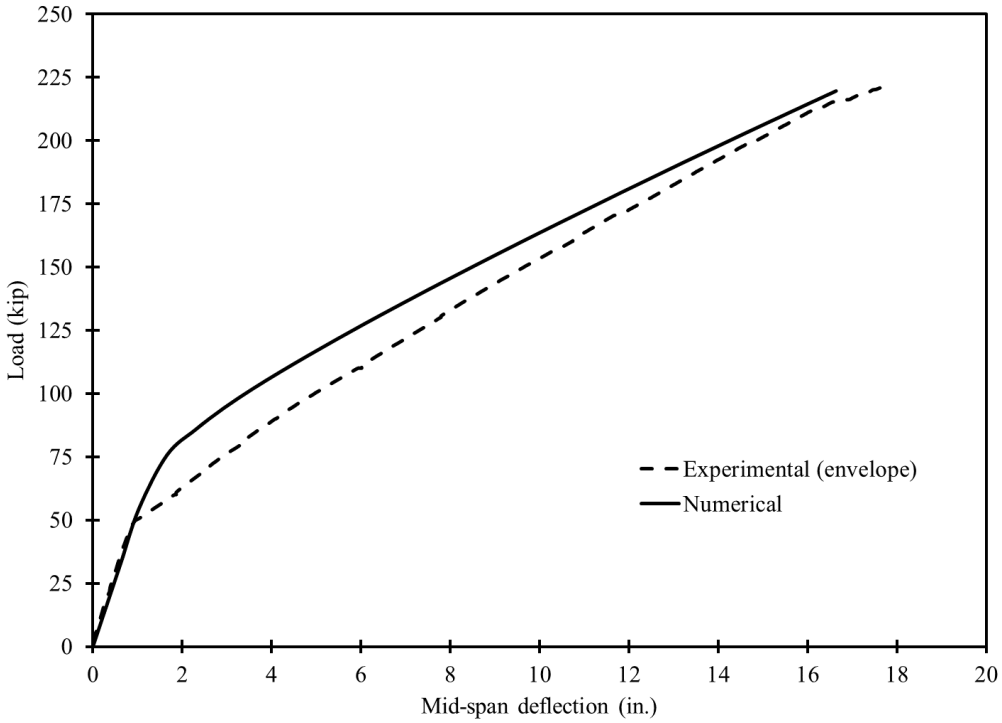

Figure 4.3-32 Numerical vs. experimental deflection curves with loads on intermediate beam during the ultimate load cycle

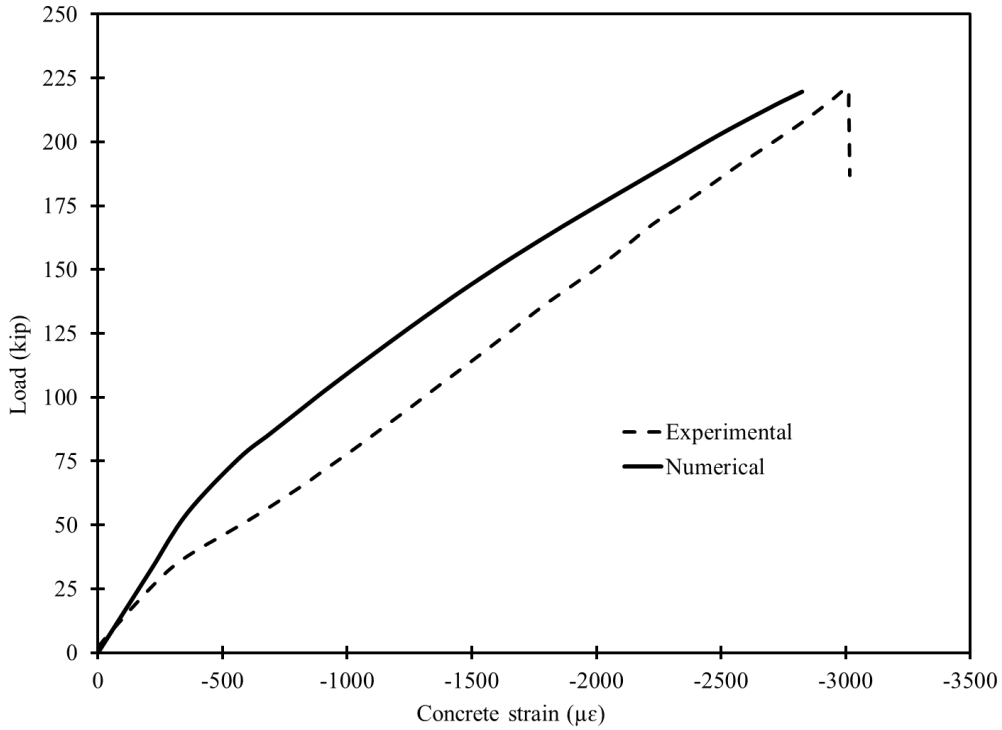

Figure 4.3-33 Numerical vs. experimental load-strain curves in concrete top surface of intermediate (loaded) beam in bridge model during ultimate load cycle

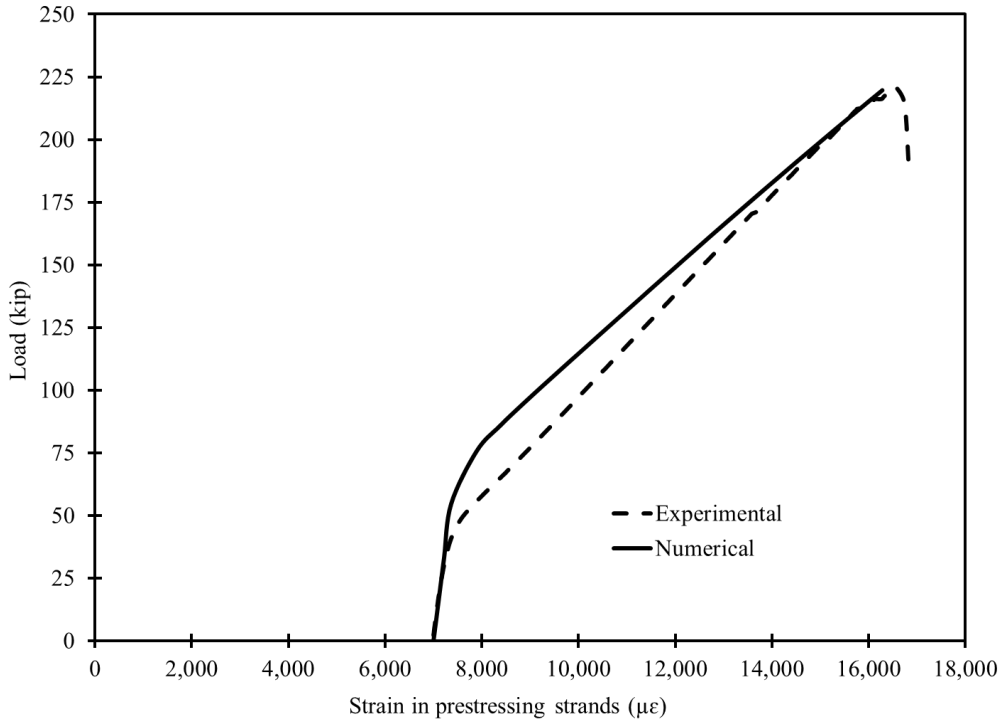

Figure 4.3-34 Numerical vs. experimental load-strain curves in prestressing strands of intermediate (loaded) beam in bridge model during ultimate load cycle

4.4 Parametric study

Through this parametric study, numerical models were generated for decked bulb T beam bridges with different spans and widths to evaluate the performance of the shear key joints and determine the need for a transverse post-tensioning system. The parametric study addressed bridges with spans of 50, 75, and 100 ft and deck widths of approximately 25, 52, and 78 ft. A general cross section for full-scale decked bulb T beam is shown in Figure 4.4-1, where the top flange width can range from 48 in. to 96 in. and the depth of the beam can range from 33 in. to 60 in. The top flange thickness is usually maintained at 9 in. and the bottom flange thickness is maintained at 8 in. with a bottom flange width of 36 in.

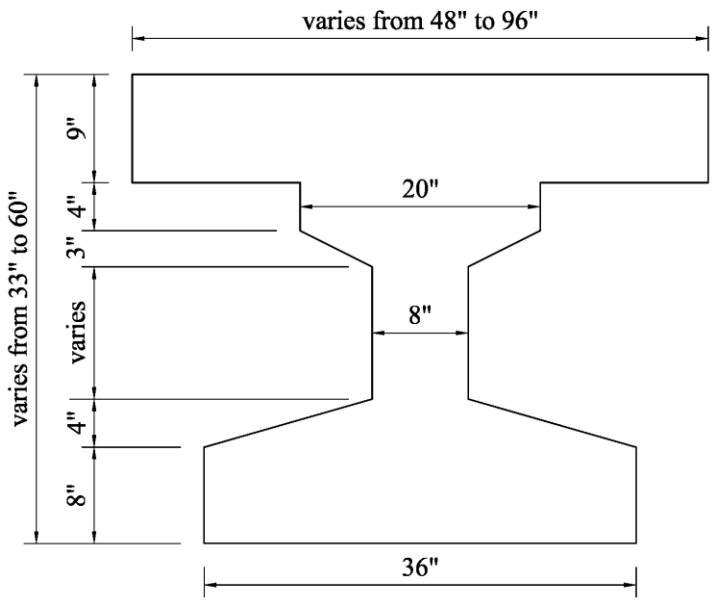

Figure 4.4-1 Typical cross section dimensions for full-scale decked bulb T beams

The choice of the cross section and the amount of reinforcement is dependent on both the span and the width of the bridge. To simplify the analysis and facilitate the choice of the appropriate cross section in the generated full-scale bridge models, a series of design charts were developed analytically to relate the span and flange width of the decked bulb T beam to the depth and the number of prestressing strands.

These design charts are developed based on the design HL-93 vehicular loading with impact allowance of 0.33 for CFCC prestressing strands with a diameter of 0.6 in, cross sectional area of 0.179 in.^{2}, guaranteed tensile strength of 339 ksi, initial prestressing force of 39.5 kip/strand (65% of guaranteed load), and average prestress loss of 15%. The 28-day concrete compressive strength was taken as 7,000 psi. It should be noted, however, that these charts are not a substitute for a detailed bridge design. Instead, they may serve as a rough estimate for the required depth of a decked bulb T beam and the required number of prestressing CFCC strands. The design charts are presented in Figure 4.4-2 through Figure 4.4-8 for decked bulb T beams with depths of 33, 36, 39, 42, 48, 54, and 60 in.

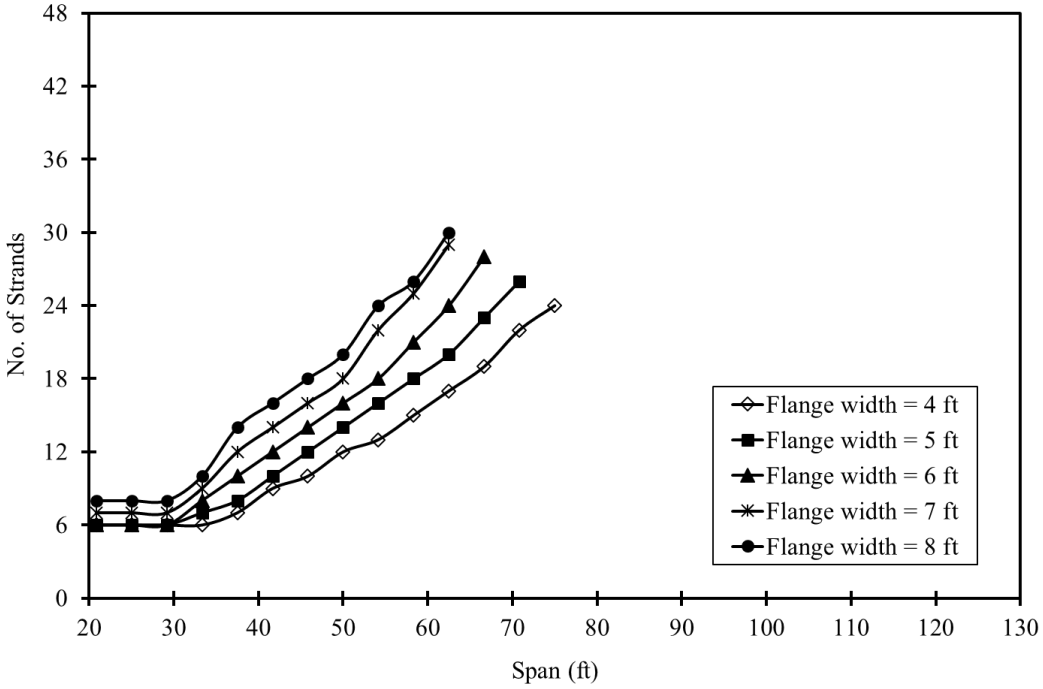

Figure 4.4-2 Design curves for 33-in.-deep decked bulb T beams

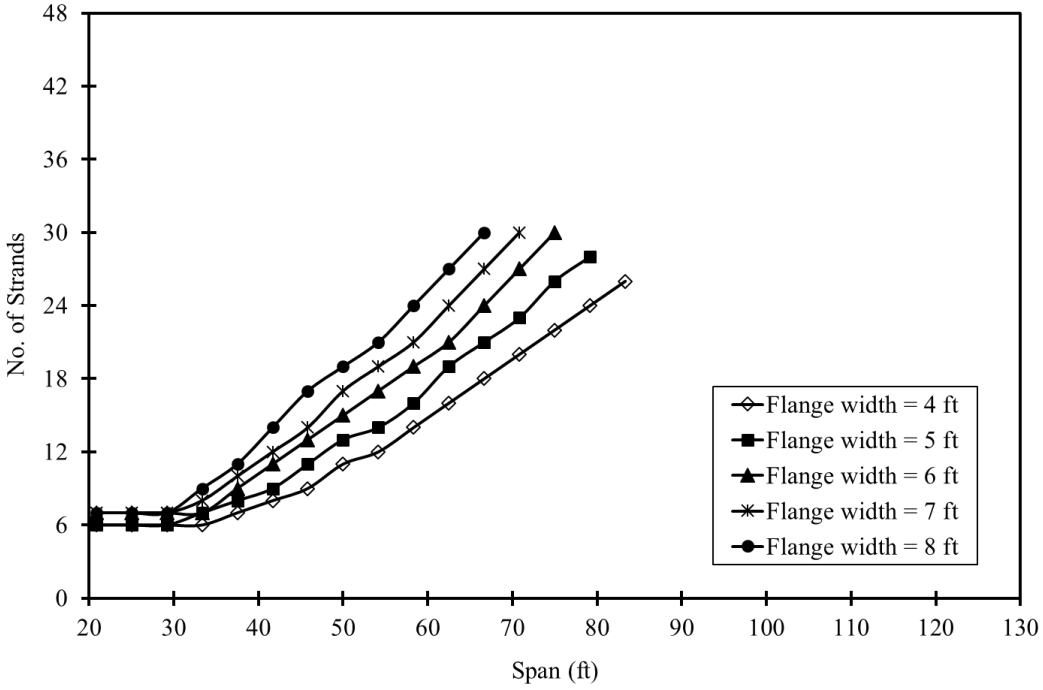

Figure 4.4-3 Design curves for 36-in.-deep decked bulb T beams

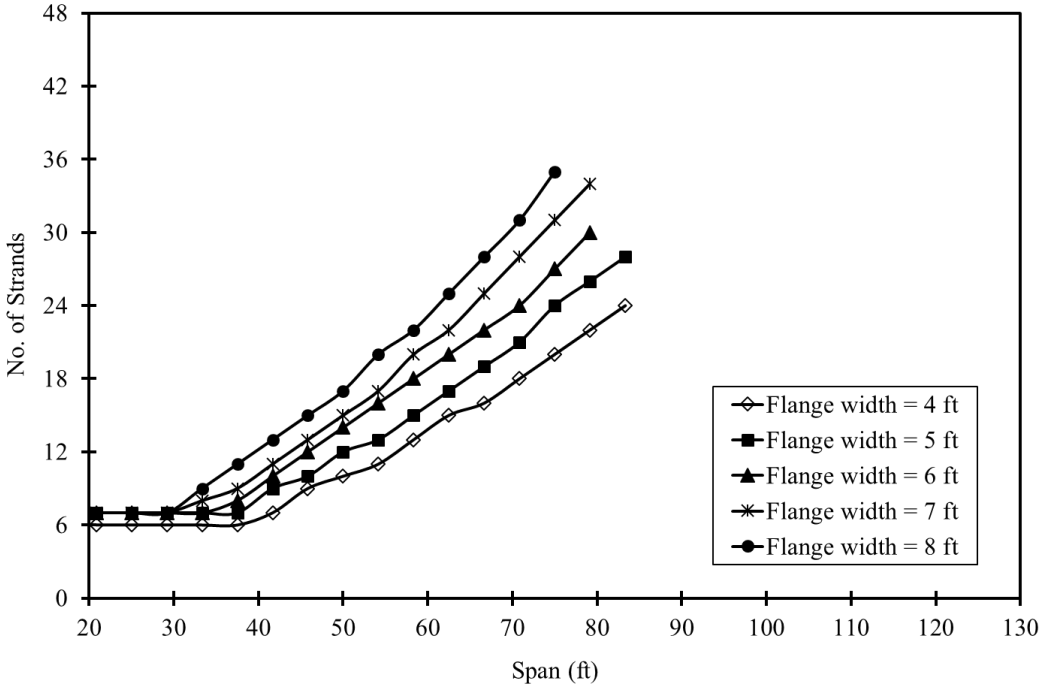

Figure 4.4-4 Design curves for 39-in.-deep decked bulb T beams

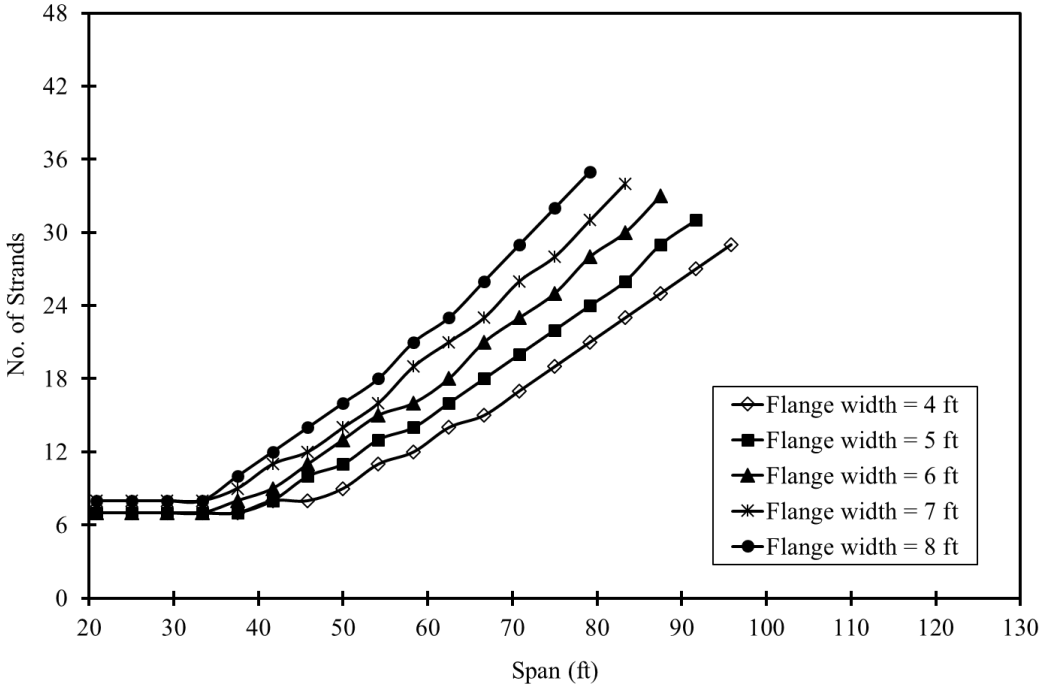

Figure 4.4-5 Design curves for 42-in.-deep decked bulb T beams

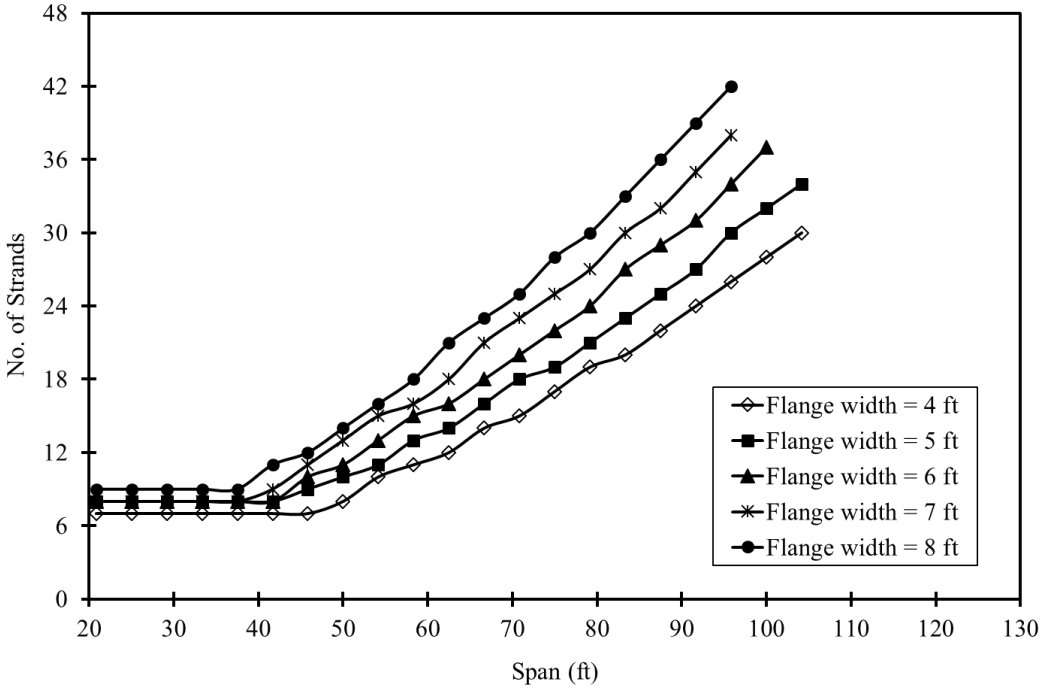

Figure 4.4-6 Design curves for 48-in.-deep decked bulb T beams

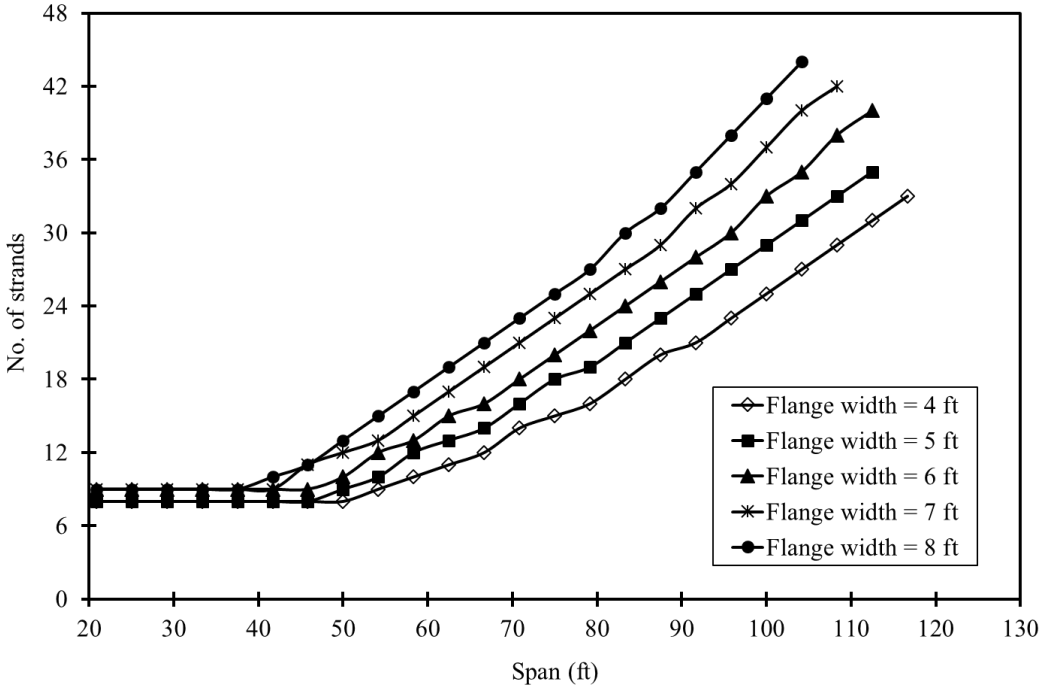

Figure 4.4-7 Design curves for 54-in.-deep decked bulb T beams

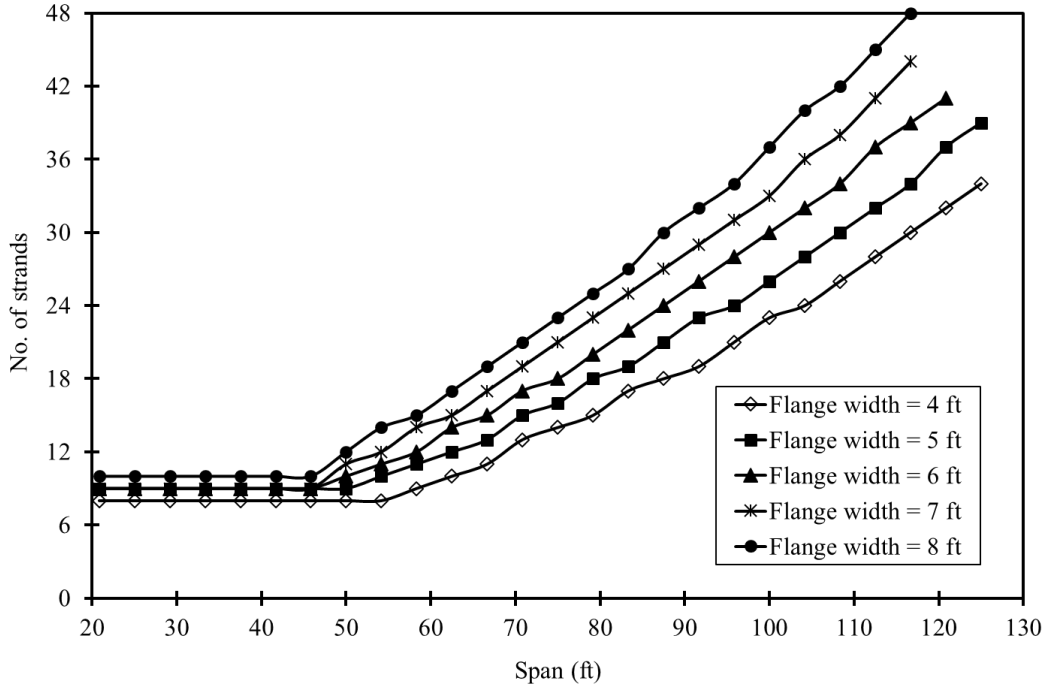

Figure 4.4-8 Design curves for 60-in.-deep decked bulb T beams

4.4.1 Loads and environmental conditions

The FEA bridge models in this parametric study were subjected to two groups of loads, construction loads and traffic loads in addition to a positive temperature gradient. Construction loads included the prestressing force, dead loads, transverse post-tensioning force, and superimposed dead loads, which included the self-weight of the parapet and the self-weight of a 2-in. wearing surface. The prestressing force and the self-weight of the beams were applied before adding the shear keys, and the diaphragms, to the bridge model. The self-weight of the shear keys and the superimposed dead loads were applied after integrating the shear keys to the bridge model. It should also be noted that the prestressing force was reduced from the initial prestressing value to the final prestressing value (85% of the initial value) after integrating the shear keys into the bridge models and before applying the superimposed dead loads.

The self-weight of the decked bulb T beams was calculated assuming a unit weight of 150 lb/ft^3 and was applied as a gravity load in the beams. The prestressing force was introduced as initial conditions in the prestressing strands with initial prestrssing force of 39.5 kip/strand and final prestressing force of 33.5 kip/strand. Superimposed dead loads included the weight of a

wearing surface (25 lb/ft^2) and the weight of the barriers. Barriers Type 4 with a weight of 475 lb/ft were provided at both sides of the bridge model.

Based on previous studies (Grace et al. 2008 and 2012), it was determined that shear key joints are most vulnerable to positive temperature gradient (+ve TG) and to a lesser extent the traffic loads. The worst situation, which usually results in shear key cracking is when positive temperature gradient is combined with traffic loads. Therefore, the application of the service loads in the current numerical investigation included applying positive temperature gradient followed by applying traffic loads. Both temperature gradient and traffic loads were taken according to AASHTO LRFD (2012) with the appropriate adjustment factors.

When exposed to sunlight during the daytime, the top fibers of the bridge experience higher temperatures than the bottom fibers, defined herein as positive gradient, and when the temperature drops down during the night in the winter, the top fibers experience lower temperatures than what the bottom fibers experience, defined herein as negative gradient. The variation of the temperature over the cross section of the bridge is usually highly nonlinear. For simplicity, AASHTO LRFD 3.12.3 provides a general bi-linear configuration for the positive temperature gradient, shown in Figure 4.4-9. The negative temperature gradient can be obtained from the same figure by multiplying the temperature values by -0.2 for decks with asphalt overlay and -0.3 for plain concrete.

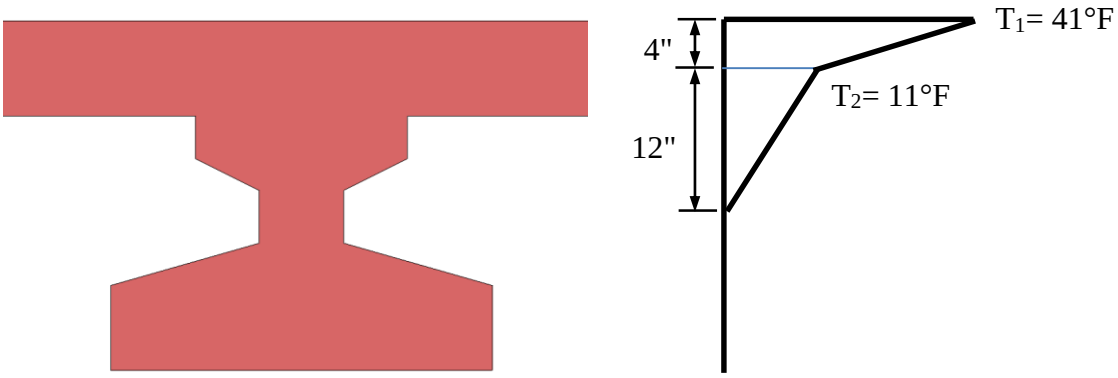

Figure 4.4-9 Positive temperature gradient (+ve TG) in MI according to AASHTO LRFD (2012)

Section 3.6.1.2 of AASHTO LRFD (2012) provides the common vehicular loading HL-93 (Figure 4.4-10), which consists of a combination of a design truck or tandem in addition to a design lane load. Each design lane under consideration shall be occupied by either a design truck or tandem, coincident with the lane load. The load shall be assumed to occupy 10.0 ft transversely within a design lane. Furthermore, the maximum live load effect shall be determined by considering each possible load combination of number of loaded lanes multiplied by the corresponding multiple presence factor as provided by Section 3.6.1.1.2 of AASHTO LRFD which account for the probability of simultaneous lane occupation by the HL-93 live load. The presence factors is highlighted in Table 4.4-1. Since the study accounts for the effect of positive temperature gradient and traffic load at the same time, a situation that may occur for a few hours during the day, it was not realistic to consider presence factor for average daily truck traffic (ADTT) more than 5,000. Instead, presence factors corresponding to ADTT between 100 and 1,000 were found appropriate for the current case of analysis.

To account for the dynamic effect of the moving loads, AASHTO LRFD 3.6.2 specifies a percentage of the static load of the truck or the tandem, but not the lane load, to be added to the original load as a dynamic allowance. The limit shall be taken as 75% for the purpose of designing the deck slab joints and 33% for designing other bridge components. It is not specified clearly in Section 3.6.2 whether 75% is applicable for the design of the transverse deck joints only or if it is applicable for the design of both transverse and longitudinal deck joints. In this numerical analysis, the impact allowance was taken equal to 75% based on the calibration of a full-scale bridge model (Grace et al. 2008).

The traffic load was positioned relative to the span of the bridge as to induce the maximum bending moment. In the transverse direction, the traffic load was positioned in three different locations named as Traffic Locations I, II, and III (TL#I, II, and III) as shown in Figure 4.4-11. In Traffic Location I, one lane (with a width of 10 ft) is occupied by the traffic load HL-93. This lane is the first lane immediately after the edge of parapet on either side of the bridge. In Traffic Location II, both side lanes of the bridge are occupied with traffic load HL-93 (each lane is loaded with HL-93 vehicular loading). In Traffic Location III, the two central lanes of the bridge are loaded with HL-93 vehicular loading. The central lanes are 10-ft-wide each measured from the mid-width of the bridge.

Table 4.4-1 Multiple presence factor, m, AASHTO LRFD 3.6.1.1.2 (2012)

Number of loaded lanes	Multiple presence factor (*m*)		
	ADTT[1] > 5000	100 ≤ ADTT ≤ 1000	ADTT < 100
1	1.20	1.14	1.08
2	1.00	0.95	0.90
3	0.85	0.81	0.73
> 3	0.65	0.62	0.59

1: Average Daily Truck Traffic

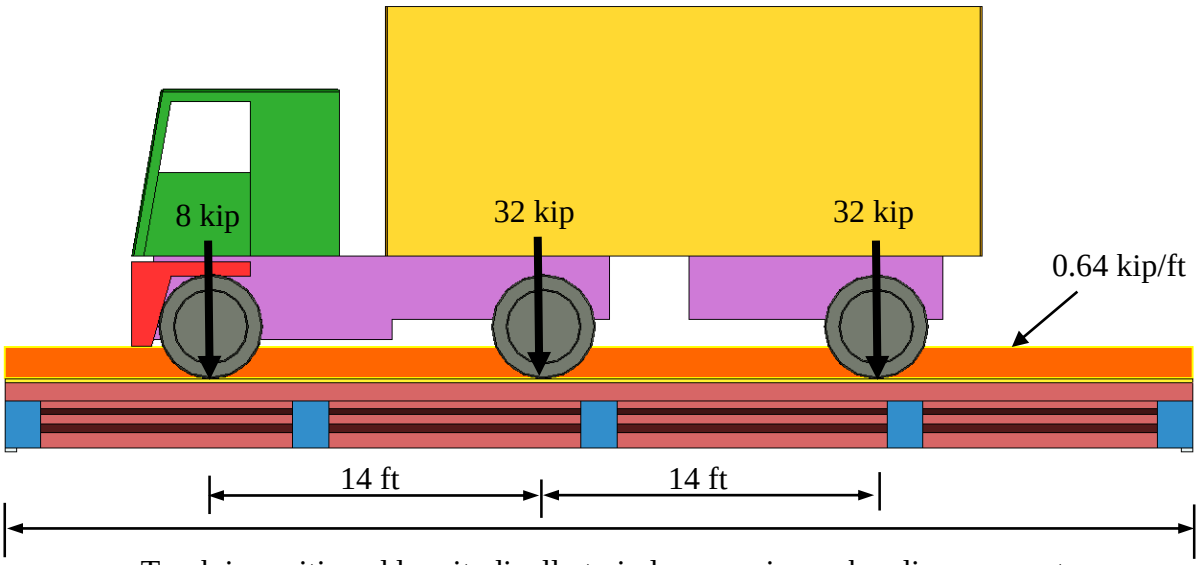

Truck is positioned longitudinally to induce maximum bending moment

Figure 4.4-10 AASHTO LRFD HL-93 vehicular loading

Traffic Location I
(TL#I)

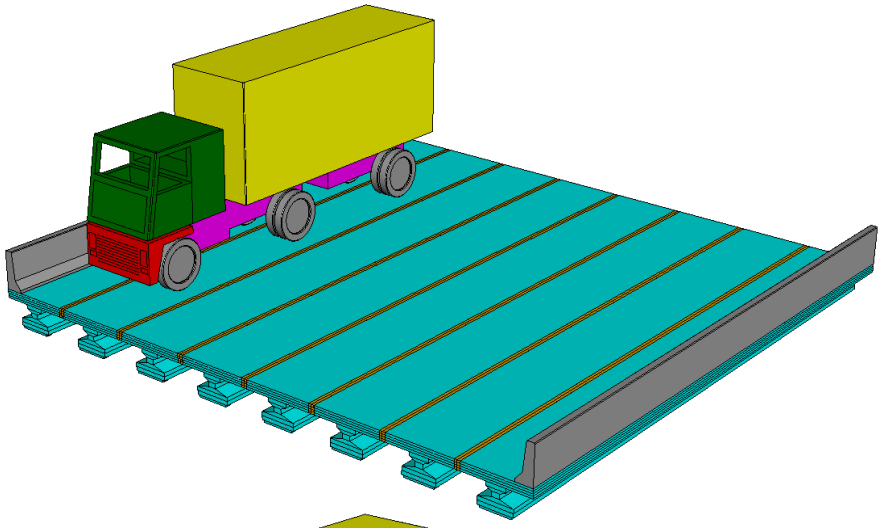

Traffic Location II
(TL#II)

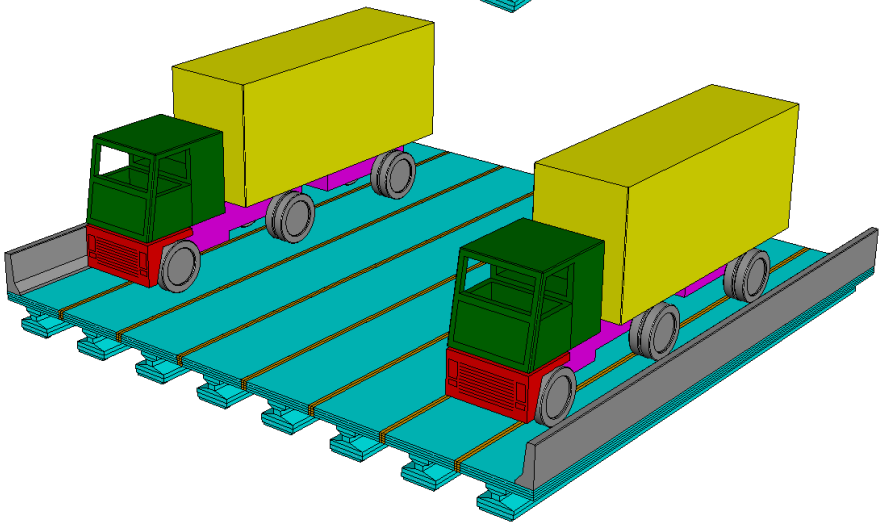

Traffic Location III
(TL#III)

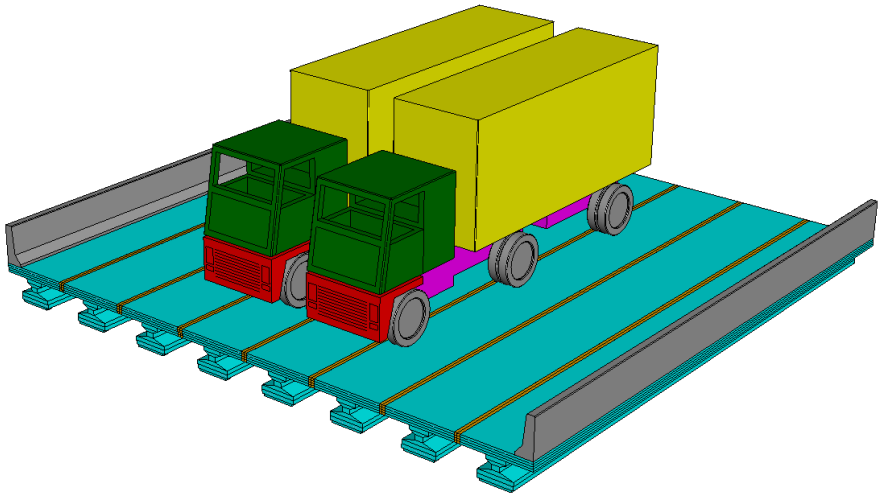

Figure 4.4-11 Truck locations across the width of the bridge models

4.4.2 Layout of parametric study

The main study was developed for decked bulb T beams with a flange width of 72 in. Later on, key models were generated for decked bulb T beams with flange widths of 48 in. and 96 in. to verify the results. The cross section dimensions and number of prestressing strands for the numerical models were selected based on the design graphs provided early in this section.

The general layout of the parametric study is presented in Figure 4.4-12. The steps of the analysis can be summarized as follows:

1. Decked bulb T beam bridge models with different span and widths were generated.
2. The bridge models were analyzed with no transverse diaphragms under positive temperature gradient and AASHTO LRFD vehicular loading with appropriate impact and presence allowances.
3. The models were checked for shear key cracks. When cracks were observed in the bridge model, the analysis was repeated with transverse diaphragms. The number of transverse diaphragms ranged from two, at the ends of the span, to five equally spaced diaphragms along the span.
4. This stage of analysis was performed for bridge models with:
    - Spans of 50, 75, and 100 ft.
    - Widths of 25, 52, and 78 ft.
    - Skew angles of 0, 30, 45, and 60°
5. When cracks persisted even with the increased number of diaphragm, TPT force was applied through the transverse diaphragms. The TPT force ranged from 50 to 200 kip/diaphragm.
6. The analysis ended when the bridge model was able to sustain the positive temperature gradient and the traffic loads with no shear key cracks.
7. Bridge models that exhibited shear key cracks even with using practical number of diaphragms and TPT force were labeled to avoid when using decked bulb T beam bridge system.

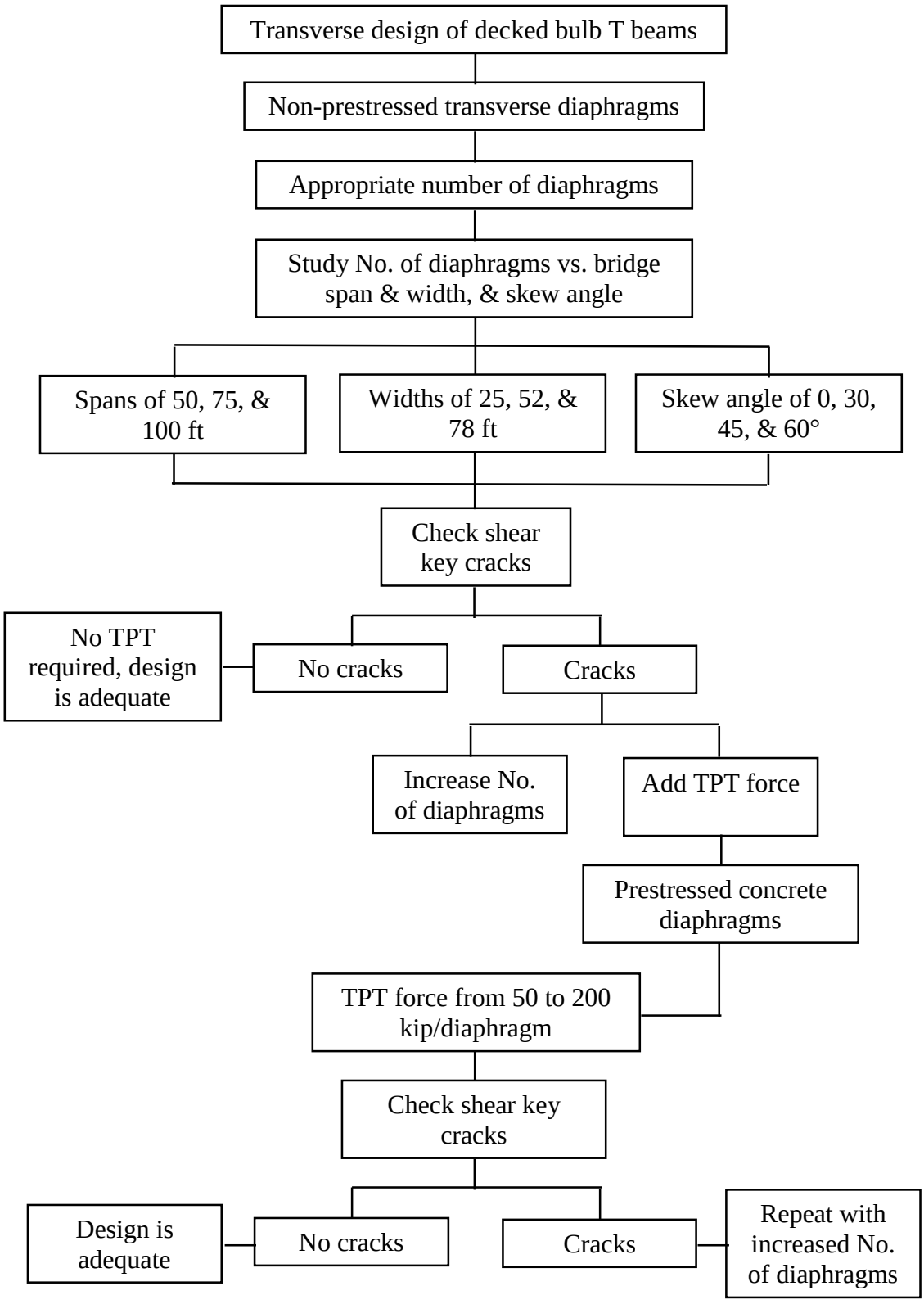

Figure 4.4-12 Flowchart of conducted parametric study

4.4.3 Configuration of numerical models

The numerical investigation included bridge models with spans of 50, 75, and 100 ft and widths of 25.5, 51.5, and 77.6 ft as shown in Figure 4.4-13. Since the main investigation was performed on decked bulb T beam with a flange width of 6 ft, bridge models with a deck width of 25.5 ft were assembled of four beams with three 6-in.-wide shear key joints. Bridge models with a deck width of 51.5 ft were assembled from eight beams with seven shear key joints and bridge models with a width of 77.5 ft were assembled from twelve beams and eleven shear key joints.

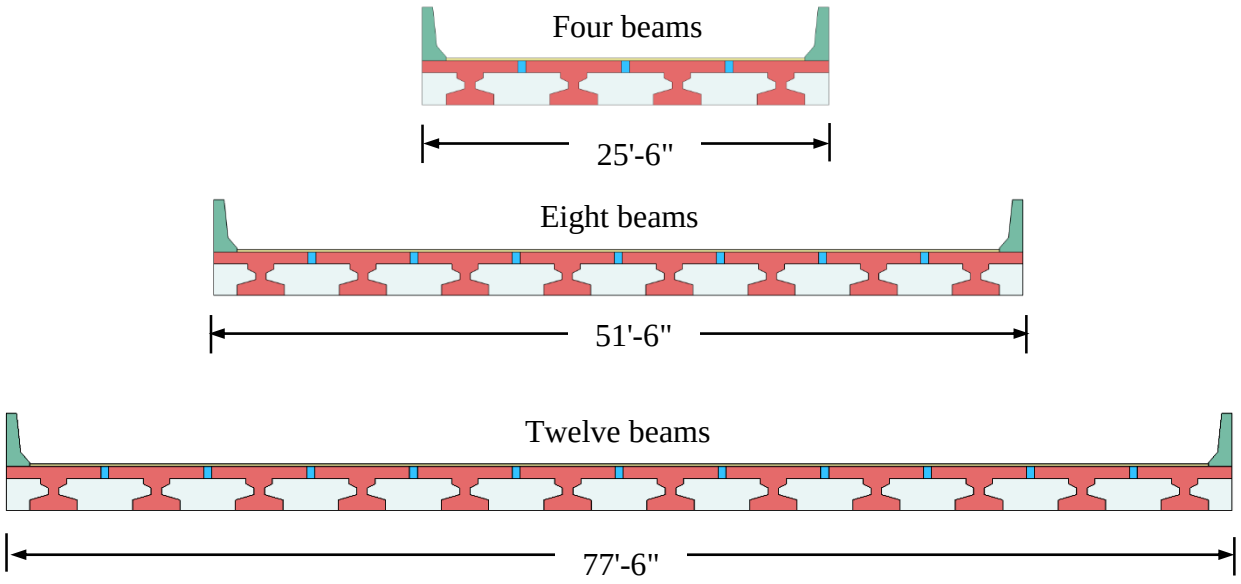

Figure 4.4-13 Widths of bridge models considered in the investigation

The cross section of the decked bulb T beam was dependent on the span. For bridge models with a span of 50 ft, 33-in-deep decked bulb T beams with 17 CFCC strands (diameter of 0.6 in.) were used through the analysis. For bridge models with a span of 75 ft, the depth of the decked bulb T beam was increased to 42 in. and the prestressing strands increased to 26 strands. Finally, for bridge models with a span of 100 ft, 54-in-deep decked bulb T beams with 34 prestressing CFCC strands were used in the analysis. The dimensions and reinforcement for the selected cross sections are shown in Figure 4.4-14.

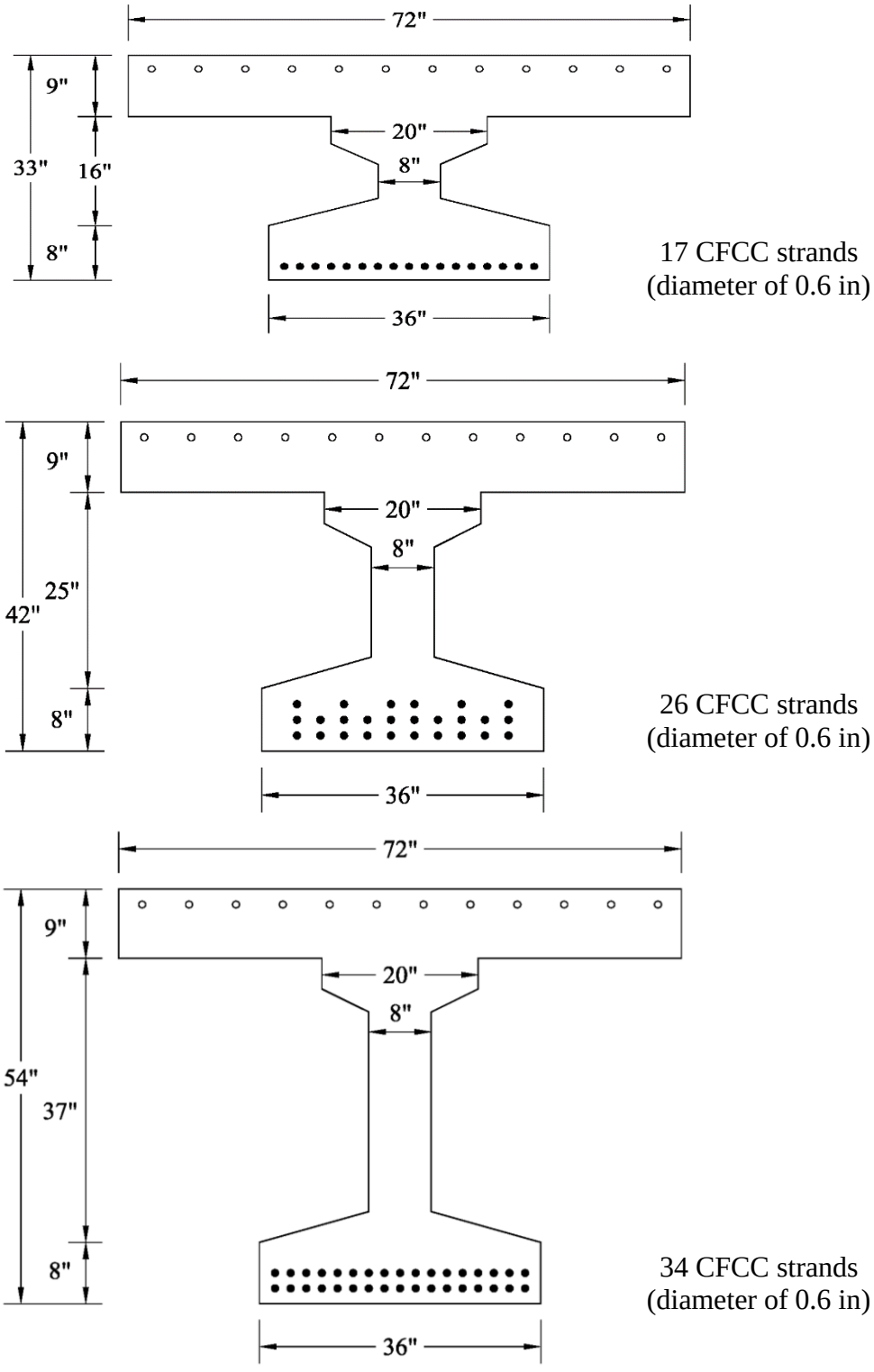

Figure 4.4-14 Configuration of cross sections used in main numerical investigation

4.4.4 Effect of number of diaphragms

The first step of the numerical analysis was to determine the appropriate number of diaphragms. All the numerical models were analyzed with:

1. No transverse diaphragms,
2. Two diaphragms at the ends,
3. Two diaphragms at the ends and one intermediate diaphragm at the mid-span
4. Five equally spaced diaphragms along the span

The general procedure for analysis and applying the loads consisted of five phases:

- Phase I included applying the self-weight of the beams and the prestressing force simultaneously. The self-weight of the beams and the prestressing force were applied to the individual beams as the shear key joints were not introduced into the model in this phase.
- The shear key joints and the joints between transverse diaphragms were integrated into the model through Phase II of analysis.
- Phase III of the analysis included applying the superimposed dead loads, the self-weight of the barriers and the weight of the wearing surface.
- Phase IV of the analysis included applying the positive temperature gradient.
- Phase V included applying the traffic loads in either Location I, II, or III.

4.4.4.1 Results of numerical models with a span of 50 ft

The maximum recorded principal, longitudinal, and transverse stresses in the deck flanges of bridge models with a span of 50 ft are shown in Table 4.4-2, Table 4.4-3, and Table 4.4-4, respectively. It should be noted that these stresses do not necessarily develop at the same location. As shown in the tables, the deck flange experiences tensile stresses during prestressing. With the current prestressing level, the longitudinal tensile stresses was approximately 392 psi and are developed near the ends of the beams. These longitudinal tensile stresses caused the maximum principal stresses at that location to reach 392 psi. There are also mild transverse tensile stresses of 125 psi due to prestressing. These transverse stresses are developed at the junction between the

web and the flange at the ends of the beams. They are not developed at the same location of the maximum longitudinal stresses of 392 psi.

Adding SIDL (self-weight of parapets and wearing service) slightly reduces the longitudinal tensile stresses and increases the transverse tensile stresses. The overall change in the maximum principal stresses does not exceed 20 psi.

A significant change in the map of stress distribution occurs when positive temperature gradient is applied to the bridge model. Concrete is considered a good thermal insulator and therefore, as the temperature of the top deck is elevated during the day, the temperature of the bottom of the deck remains substantially low. According to AASHTO LRFD (2012), this difference in temperature through the depth of the deck flange can reach 35 °F. The expansion of the top surface due to heating generates compressive stresses in the top fibers and tensile stresses in the bottom fibers of the deck flange.

Applying positive temperature gradient increased or decreased the maximum principal stresses as shown in the Table 4.4-2. A clear relationship cannot be established from the maximum principal stresses as the location of the maximum stresses changes with applying the positive temperature gradient. However, by examining the longitudinal and transverse stresses, it can be determined that applying positive temperature gradient resulted in reduction in the longitudinal tensile stresses but a significant increase in the transverse tensile stresses. The increase in transverse stresses is maximized in the case of no transverse diaphragms and decreases with the increase in the number of diaphragms. The same trend is noticed in bridge models with different widths.

The maximum transverse stresses due to positive temperature gradient are developed near the ends of the beams. Therefore, adding two end diaphragms seems to have the maximum influence on reducing the transverse stresses under positive temperature gradient. Adding intermediate diaphragms does not seem to have the same transverse stress reduction influence as that of the end diaphragms as shown in Figure 4.4-15.

The addition of traffic load at select locations seems to further increase the maximum principal stresses and the transverse tensile stresses in the deck flange. For instance, adding the traffic load in Location I in bridges with no transverse diaphragms results in cracking the deck flange (Figure

4.4-16). The cracks appeared in all bridge models regardless of the deck width. The cracks developed at the ends of the beams at the locations that showed high transverse tensile stresses under positive temperature gradient.

Adding end diaphragms to the bridge model eliminated the cracks at the ends of the beams and reduced the maximum principal stresses and the tensile transverse stresses in the deck. Intermediate diaphragms, while slightly reducing the tensile stress, did not seem to greatly influence the stress values in case of traffic loads at Location I.

The same trend was also noticed when adding traffic load in Location II. Cracks developed at the ends of the beams where there was no transverse diaphragms (Figure 4.4-17). After adding the end diaphragms, the maximum principal stresses and the transverse stresses in the deck reduced and the cracks were eliminated at the ends of the beams. Adding intermediate diaphragms did not seem to have a significant influence on the stress level under this loading case even though bridge models with five transverse diaphragms consistently exhibited slightly lesser tensile stresses than those observed in bridge models with two or three transverse diaphragms.

Unlike Locations I and II, traffic loads positioned in Location III showed a direct relationship to the number of intermediate diaphragms with no relationship to the end diaphragms. In case of bridge models with no diaphragms or with diaphragms at the ends only, the models with traffic loads at Location III always exhibited cracks at the mid-span of the bridge (Figure 4.4-18). When an intermediate diaphragm is added, the shear key cracks were eliminated but the transverse stresses and the corresponding maximum principal stresses remained critical. Increasing the number of diaphragms from three to five significantly reduced the transverse stresses by approximately 148 psi and 208 psi in case of bridge models with deck widths of 52.5 ft and 77.5 ft, respectively.

Table 4.4-2 Maximum principal stresses in deck flange for bridges with a span of 50 ft

Span (ft)	Width (ft)	No. Diaph.	Maximum principal stresses in deck (psi)					
			Prestress	SIDL	+ve TG	TL#I	TL#II	TL#III
50	25.5	0	392	379	569	crack	-	-
	25.5	2		386	356	482	-	-
	25.5	3		377	346	421	-	-
	25.5	5		374	332	395	-	-
	51.5	0		396	527	crack	crack	crack
	51.5	2		401	365	425	443	crack
	51.5	3		393	365	417	438	430
	51.5	5		388	347	416	407	309
	77.5	0		405	527	crack	crack	crack
	77.5	2		410	384	475	485	crack
	77.5	3		403	386	476	488	502
	77.5	5		399	353	431	441	322

Table 4.4-3 Longitudinal stresses in deck flange for bridges with a span of 50 ft

Span (ft)	Width (ft)	No. Diaph.	Longitudinal stresses in deck (psi)					
			Prestress	SIDL	+ve TG	TL#I	TL#II	TL#III
50	25.5	0	392	375	277	crack	-	-
	25.5	2		382	278	294	-	-
	25.5	3		375	268	283	-	-
	25.5	5		373	266	274	-	-
	51.5	0		393	288	crack	crack	crack
	51.5	2		397	292	315	305	crack
	51.5	3		391	294	314	300	242
	51.5	5		387	293	310	296	247
	77.5	0		403	293	crack	crack	crack
	77.5	2		407	301	314	325	crack
	77.5	3		401	302	311	323	267
	77.5	5		398	302	309	321	267

Table 4.4-4 Transverse stresses in deck flange for bridges with a span of 50 ft

Span (ft)	Width (ft)	No. Diaph.	Transverse stresses in deck (psi)					
			Prestress	SIDL	+ve TG	TL#I	TL#II	TL#III
50	25.5	0	125	153	565	crack	-	-
	25.5	2		144	337	406	-	-
	25.5	3		135	306	357	-	-
	25.5	5		129	288	339	-	-
	51.5	0		162	521	crack	crack	crack
	51.5	2		146	365	396	436	crack
	51.5	3		139	354	389	432	430
	51.5	5		137	334	389	399	282
	77.5	0		165	522	crack	crack	crack
	77.5	2		147	374	472	480	crack
	77.5	3		140	377	473	484	502
	77.5	5		138	342	427	435	294

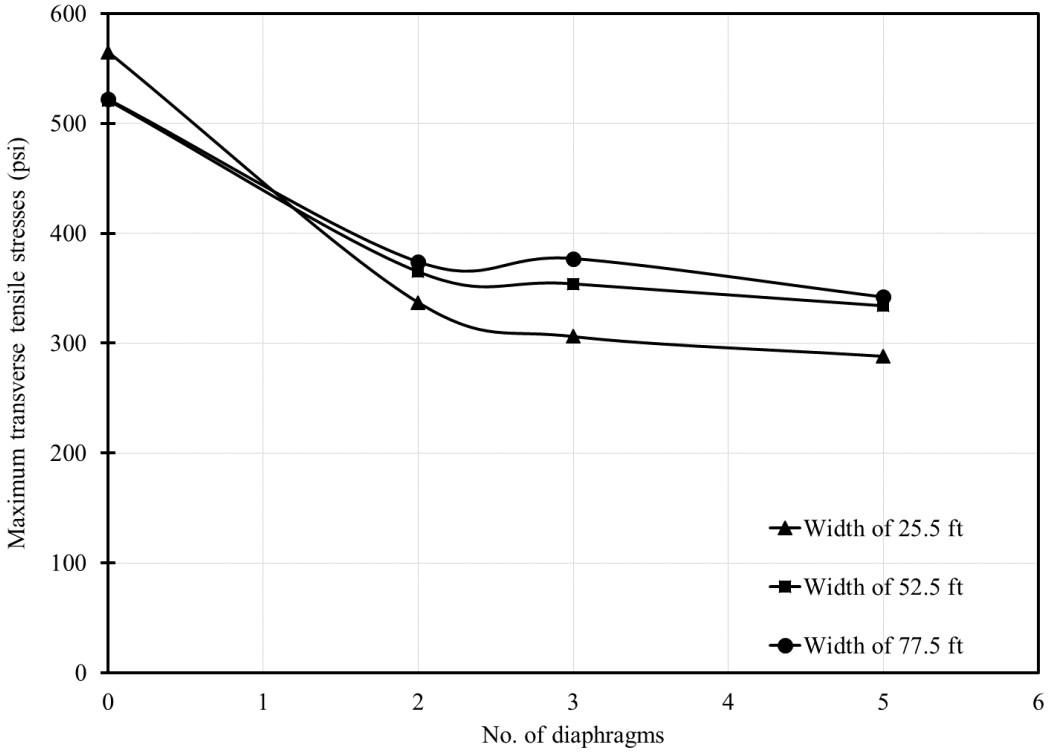

Figure 4.4-15 Effect of increasing number of diaphragms on transverse stresses under positive temperature gradient in bridges with a span of 50 ft

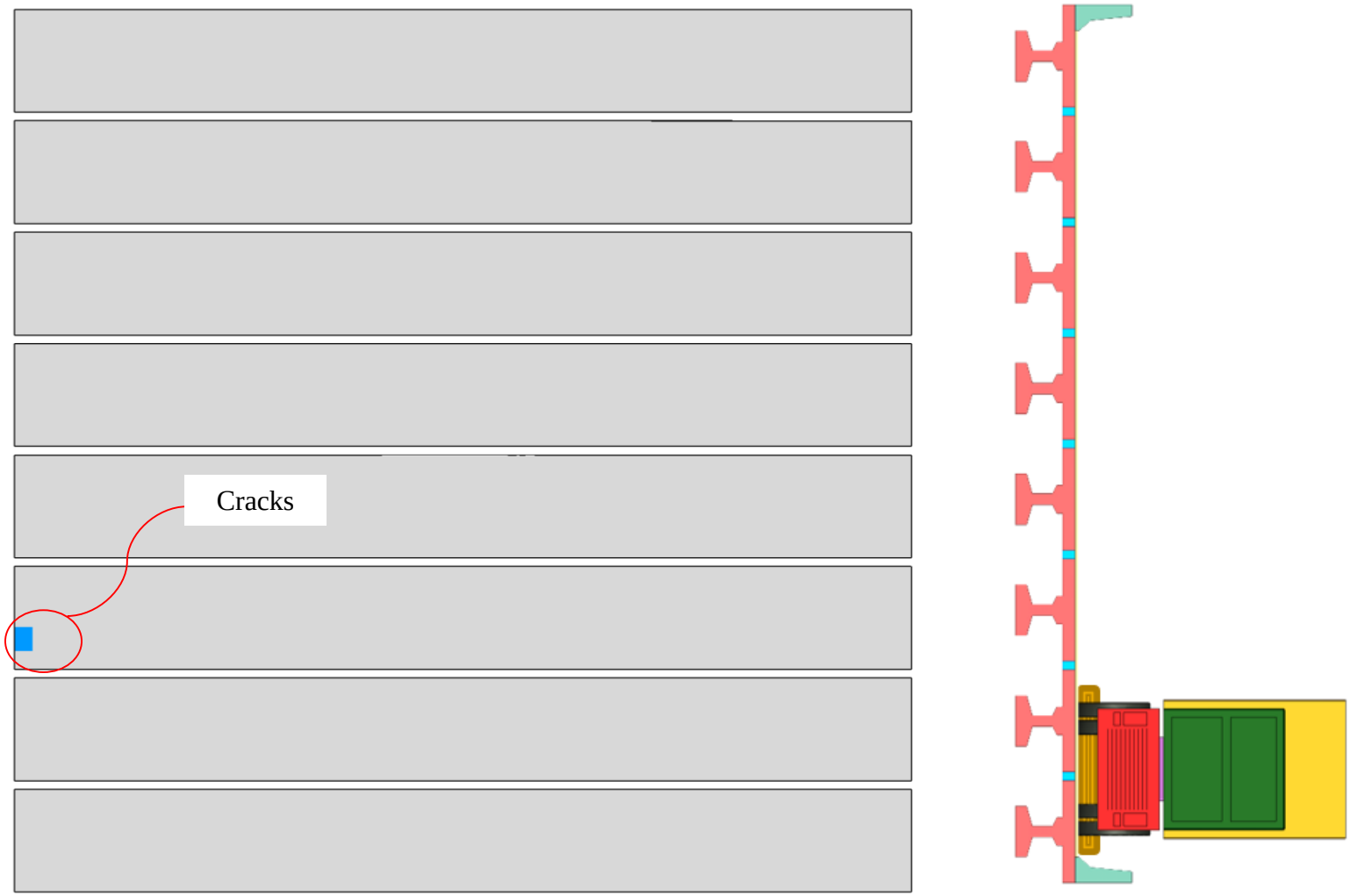

Figure 4.4-16 Typical crack pattern under traffic loads in Location I (Bridge span of 50 ft, width of 52.5 ft, no diaphragms)

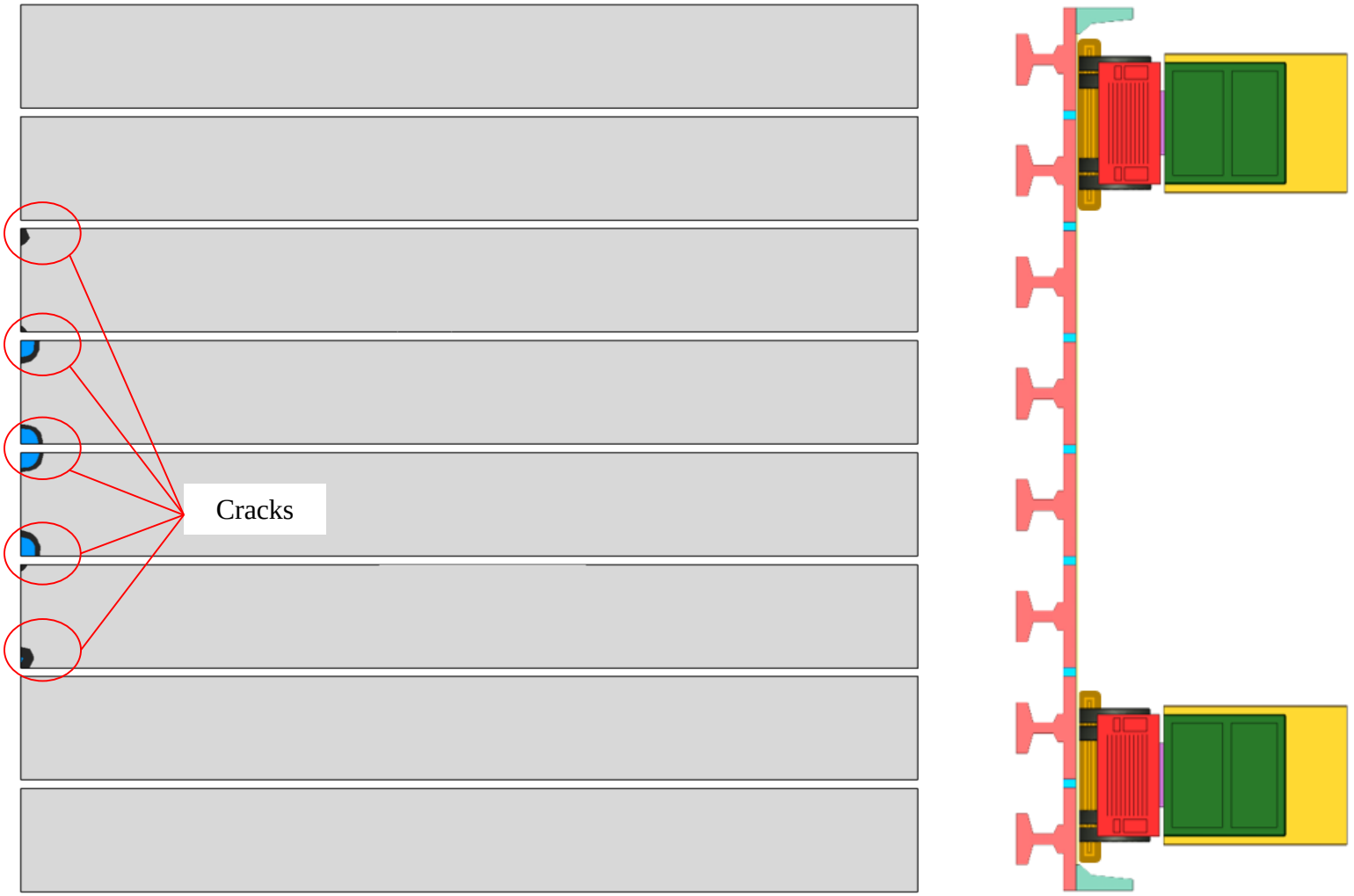

Figure 4.4-17 Typical crack pattern under traffic loads in Location II (Bridge span of 50 ft, width of 52.5 ft, no diaphragms)

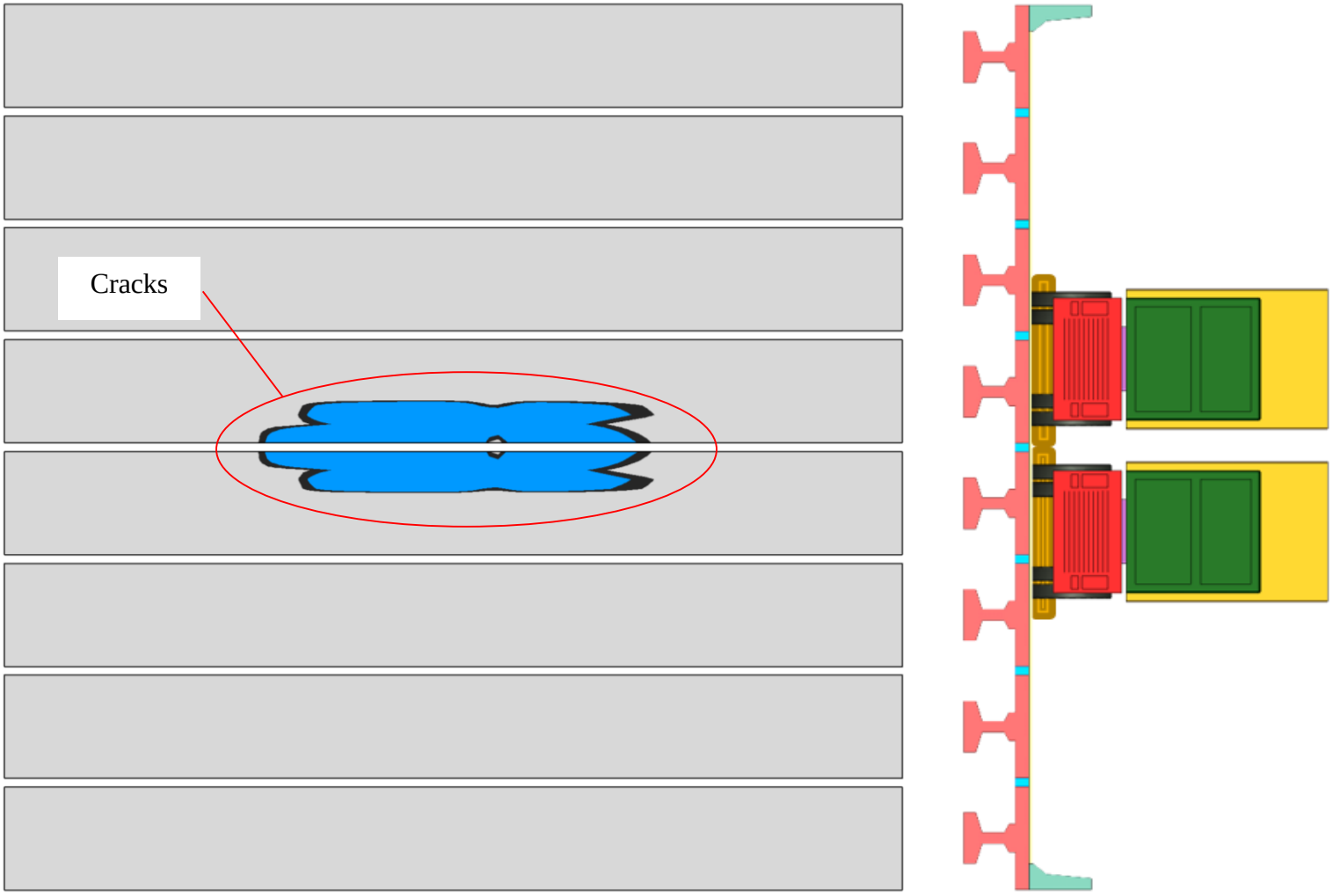

Figure 4.4-18 Typical crack pattern under traffic loads at Location III (Bridge span of 50 ft, width of 52.5 ft, no diaphragms)

4.4.4.2 Results of numerical models with a span of 75 ft

The maximum principal stresses, longitudinal stresses, and transverse stresses in the deck flanges of bridge models with a span of 70 ft are shown in Table 4.4-5, Table 4.4-6, and Table 4.4-7. The relationship between the number of diaphragms and both the span and width of the bridge models was similar to that observed in bridge models with a span of 50 ft. The case of no transverse diaphragms always yielded deck cracking regardless of the width of the bridge model. Adding two end diaphragms seemed to reduce the transverse tensile stresses under positive temperature gradient and under traffic loads in Locations I and II. However, it did not mitigate the crack development when the traffic loads were positioned in Location III. The deck cracking due to traffic loads at Location III was mitigated after adding intermediate diaphragms. In bridge models with widths of 25.5 ft and 51.5 ft, an intermediate diaphragm in addition to the two end diaphragms were sufficient to prevent deck cracking. However, in case of bridge models with a width of 77.5 ft, it was mandatory to provide five transverse diaphragms to eliminate the cracks.

It should be noted that in the case of bridge models with a span of 75 ft and a deck width of 77.5 ft, the size of the analysis file was too large to be processed. Therefore, only half of the model was analyzed and symmetry conditions were assumed along the longitudinal axis of the bridge model. Because of the symmetry, applying the traffic loads in Location I was not feasible and only the cases of traffic loads in Locations II and III were analyzed.

The concentration of the stresses took the same pattern observed in bridge models with a span of 50 ft. The superimposed dead loads did not significantly increase or decrease the stresses in the different directions. However, positive temperature gradient caused a dramatic increase in the transverse stresses and consequently the principal stresses. The increase in the stresses was relatively localized near the ends of the beams. By adding the end diaphragms, the transverse stresses were reduced and the maximum values shifted towards the mid-span.

The addition of the traffic loads in Locations I and II seemed to overstress the region with already high transverse tensile stresses due to positive temperature gradient. However, transverse stresses due to traffic loads in Location III took a different pattern and accumulated at the mid-span rather than the ends of the beams. The region of the mid-span suffered from moderate increase in tensile transverse stresses during the application of positive temperature gradient.

Table 4.4-5 Maximum principal stresses in deck flange for bridges with a span of 75 ft

Span (ft)	Width (ft)	No. Diaph.	Maximum principal stresses in deck (psi)					
			Prestress	SIDL	+ve TG	TL#I	TL#II	TL#III
75	25.5	0	357	361	592	crack	-	-
	25.5	2		360	339	381		
	25.5	3		351	329	363	-	-
	25.5	5		346	325	369	-	-
	51.5	0		383	549	crack	crack	crack
	51.5	2		383	371	433	408	crack
	51.5	3		367	365	399	361	457
	51.5	5		360	348	384	352	357
	77.5	0		360	590	-	crack	crack
	77.5	2		385	378	-	crack	crack
	77.5	3		373	369	-	crack	crack
	77.5	5		366	351	-	469	358

Table 4.4-6 Longitudinal stresses in deck flange for bridges with a span of 75 ft

Span (ft)	Width (ft)	No. Diaph.	Longitudinal stresses in deck (psi)					
			Prestress	SIDL	+ve TG	TL#I	TL#II	TL#III
75	25.5	0	357	358	258	crack	-	-
	25.5	2		356	253	290	-	-
	25.5	3		349	235	271	-	-
	25.5	5		346	229	255	-	-
	51.5	0		379	279	crack	crack	crack
	51.5	2		377	281	330	306	crack
	51.5	3		364	272	309	276	230
	51.5	5		358	269	298	266	235
	77.5	0		358	268	-	crack	crack
	77.5	2		378	277	-	crack	crack
	77.5	3		369	274	-	crack	crack
	77.5	5		364	274	-	296	237

Table 4.4-7 Transverse stresses in deck flange for bridges with a span of 75 ft

Span (ft)	Width (ft)	No. Diaph.	Transverse stresses in deck (psi)					
			Prestress	SIDL	+ve TG	TL#I	TL#II	TL#III
75	25.5	0	110	144	592	crack	-	-
	25.5	2		121	280	336	-	-
	25.5	3		117	317	359	-	-
	25.5	5		113	320	348	-	-
	51.5	0		156	547	crack	crack	crack
	51.5	2		133	367	372	337	crack
	51.5	3		124	322	345	306	457
	51.5	5		118	314	343	327	355
	77.5	0		150	590	-	crack	crack
	77.5	2		130	376	-	crack	crack
	77.5	3		126	358	-	crack	crack
	77.5	5		124	347	-	467	356

4.4.4.3 Results of numerical models with a span of 100 ft

The stresses in bridge models with a span of 100 ft followed the same trend observed in models with spans of 50 and 75 ft with the exception that the stresses were slightly higher. Deck cracking was seen as early as when positive temperature gradient was applied. This indicates that tensile stresses in the deck increases with increasing bridge span. However, five diaphragms were sufficient to mitigate the deck cracking in all bridge models with a span of 100 ft as shown in Table 4.4-8, Table 4.4-9, and Table 4.4-10. Bridge models with a span of 100 ft and a width of 51.5 ft or 77.5 ft were not analyzed with traffic loads at Location I as only half of the bridge was modeled and symmetry conditions were assumed along its longitudinal axis.

Table 4.4-8 Maximum principal stresses in deck flange for bridges with a span of 100 ft

Span (ft)	Width (ft)	No. Diaph.	Maximum principal stresses in deck (psi)					
			Prestress	SIDL	+ve TG	TL#I	TL#II	TL#III
100	25.5	0	355	319	crack	crack	-	-
	25.5	2		317	341	382	-	-
	25.5	3		310	356	370	-	-
	25.5	5		307	356	381	-	-
	51.5	0		383	549	-	crack	crack
	51.5	2		342	389	-	400	crack
	51.5	3		323	387	-	366	471
	51.5	5		318	379	-	358	357
	77.5	0		383	crack	-	crack	crack
	77.5	2		385	378	-	crack	crack
	77.5	3		373	368	-	crack	crack
	77.5	5		366	351	-	469	358

Table 4.4-9 Longitudinal stresses in deck flange for bridges with a span of 100 ft

Span (ft)	Width (ft)	No. Diaph.	Longitudinal stresses in deck (psi)					
			Prestress	SIDL	+ve TG	TL#I	TL#II	TL#III
100	25.5	0	354	317	crack	crack	-	-
	25.5	2		312	295	275	-	-
	25.5	3		308	275	264	-	-
	25.5	5		307	259	252	-	-
	51.5	0		379	279	-	crack	crack
	51.5	2		335	295	-	291	crack
	51.5	3		320	282	-	263	246
	51.5	5		318	269	-	256	235
	77.5	0		378	crack	-	crack	crack
	77.5	2		378	277	-	crack	crack
	77.5	3		368	274	-	crack	crack
	77.5	5		364	274	-	296	237

Table 4.4-10 Transverse stresses in deck flange for bridges with a span of 100 ft

Span (ft)	Width (ft)	No. Diaph.	Transverse stresses in deck (psi)					
			Prestress	SIDL	+ve TG	TL#I	TL#II	TL#III
100	25.5	0	103	134	crack	crack	-	-
	25.5	2		120	287	322	-	-
	25.5	3		105	356	363	-	-
	25.5	5		97	355	367	-	-
	51.5	0		156	547	-	crack	crack
	51.5	2		114	368	-	310	crack
	51.5	3		102	358	-	353	471
	51.5	5		98	329	-	343	355
	77.5	0		130	crack	-	crack	crack
	77.5	2		130	376	-	crack	crack
	77.5	3		126	358	-	crack	crack
	77.5	5		124	347	-	467	356

4.4.5 Effect of skew angle

The numerical investigation extended to examine the influence of the skew angle on the development of shear key cracks in a decked bulb T beam bridge system. Key bridge models with skew angles of 30, 45, and 60 degrees were generated and analyzed under the same loading and environmental conditions. The results were compared with those of bridges with no skew angle.

As shown in Table 4.4-11 through Table 4.4-18, the maximum principal stresses, longitudinal stresses, and transverse stresses in the deck flanges of the bridge models increase with increasing the skew angle. All the bridge models were analyzed with five equally spaced transverse diaphragms but without TPT force.

Compared to those with no skew angle, bridge models with a skew angle of 30° showed a remarkable increase in the overall deck flange tensile stresses. The increase in the tensile stresses due to the skew angle does not seem to be directly related to the span length. For instance, bridges with a width of 25.5 ft and span lengths of 50, 75, and 100 ft experienced an increase in the maximum principal stresses of 16, 28, and 28%, respectively from similar bridges with no skew

angles. It should be noted that the location of the maximum tensile stresses, whether near the ends of the beams or near the middle region of the span, varied from case to case depending on the loading conditions.

The bridge width also does not seem to be directly related to the increase in the deck flange tensile stresses due to the skew angle. For instance, bridges with a span of 100 ft and widths of 25.5, 51.5, and 77.5 ft experienced an increase in the maximum principal stresses of approximately 16, 29, and 30%, respectively.

Table 4.4-18 and Figure 4.4-19 through Figure 4.4-21 show the increase in the tensile stresses with increasing the skew angle. In bridges with skew angle of 60°, cracks developed at the shear key joints when the traffic loads were added at Locations I, II, and III. Similarly, the tensile stresses in bridges with a skew angle of 45° also increased from the stresses observed in bridges with no skew angle and as shown in Figure 4.4-22, the deck flange experienced shear key cracks when the traffic loads were added at Location I. Adding the traffic loads at Locations II and III in the 45°-skew bridge did not yield any shear key cracks. However, the maximum principal stresses reached approximately 511 and 463 psi, respectively.

Table 4.4-11 Deck flange stresses for bridges with a span of 50 ft and a width of 25.5 ft

	Maximum principal stresses (psi)			Longitudinal stresses (psi)			Transverse stresses (psi)		
	Skew angle		% increase	Skew angle		% increase	Skew angle		% increase
	0°	30°		0°	30°		0°	30°	
+ve TG	332	359	8%	266	275	3%	288	280	-3%
TL#I	395	457	16%	274	274	0%	339	425	25%

Table 4.4-12 Deck flange stresses for bridges with a span of 50 ft and a width of 51.5 ft

	Maximum principal stresses (psi)			Longitudinal stresses (psi)			Transverse stresses (psi)		
	Skew angle		% increase	Skew angle		% increase	Skew angle		% increase
	0°	30°		0°	30°		0°	30°	
+ve TG	347	430	24%	293	318	9%	334	341	2%
TL#I	416	507	22%	310	308	-1%	389	461	19%
TL#II	407	447	10%	296	375	27%	399	417	5%
TL#III	309	400	29%	247	260	5%	282	399	42%

Table 4.4-13 Deck flange stresses for bridges with a span of 50 ft and a width of 77.5 ft

	Maximum principal stresses (psi)			Longitudinal stresses (psi)			Transverse stresses (psi)		
	Skew angle		% increase	Skew angle		% increase	Skew angle		% increase
	0°	30°		0°	30°		0°	30°	
+ve TG	353	436	24%	302	320	6%	342	336	-2%
TL#I	431	453	5%	309	403	30%	427	447	5%
TL#II	441	475	8%	321	394	23%	435	427	2%
TL#III	322	420	30%	267	274	3%	294	417	42%

Table 4.4-14 Deck flange stresses for bridges with a span of 75 ft and a width of 25.5 ft

	Maximum principal stresses (psi)			Longitudinal stresses (psi)			Transverse stresses (psi)		
	Skew angle		% increase	Skew angle		% increase	Skew angle		% increase
	0°	30°		0°	30°		0°	30°	
+ve TG	325	322	-1%	229	286	25%	320	304	-5%
TL#I	369	473	28%	255	273	7%	348	451	30%

Table 4.4-15 Deck flange stresses for bridges with a span of 75 ft and a width of 51.5 ft

	Maximum principal stresses (psi)			Longitudinal stresses (psi)			Transverse stresses (psi)		
	Skew angle		% increase	Skew angle		% increase	Skew angle		% increase
	0°	30°		0°	30°		0°	30°	
+ve TG	348	392	13%	269	319	19%	314	364	16%
TL#I	384	470	22%	298	366	23%	343	459	34%
TL#II	352	427	21%	266	335	26%	327	420	28%
TL#III	357	415	16%	235	266	13%	355	414	17%

Table 4.4-16 Deck flange stresses for bridges with a span of 75 ft and a width of 77.5 ft

	Maximum principal stresses (psi)			Longitudinal stresses (psi)			Transverse stresses (psi)		
	Skew angle		% increase	Skew angle		% increase	Skew angle		% increase
	0°	30°		0°	30°		0°	30°	
+ve TG	351	406	16%	274	327		347	380	10%
TL#I	-	-	-	-	-	-	-	-	-
TL#II	469	475	1%	296	457	54%	467	451	-3%
TL#III	358	427	19%	237	280	18%	356	424	19%

Table 4.4-17 Deck flange stresses for bridges with a span of 100 ft and a width of 25.5 ft

	Maximum principal stresses (psi)			Longitudinal stresses (psi)			Transverse stresses (psi)		
	Skew angle		% increase	Skew angle		% increase	Skew angle		% increase
	0°	30°		0°	30°		0°	30°	
+ve TG	356	380	7%	259	297	15%	355	335	-6%
TL#I	381	486	28%	252	310	23%	367	480	31%

Table 4.4-18 Deck flange stresses for bridges with a span of 75 ft and a width of 51.5 ft

	Maximum principal stresses (psi)				Longitudinal stresses (psi)				Transverse stresses (psi)			
	Skew angle				Skew angle				Skew angle			
	0°	30°	45°	60°	0°	30°	45°	60°	0°	30°	45°	60°
+ve TG	348	392	357	427	269	319	326	375	314	364	349	403
TL#I	384	470	C	C	298	366	C	C	343	459	C	C
TL#II	352	427	511	C	266	335	355	C	327	420	500	C
TL#III	357	415	463	C	235	266	239	C	355	414	457	C

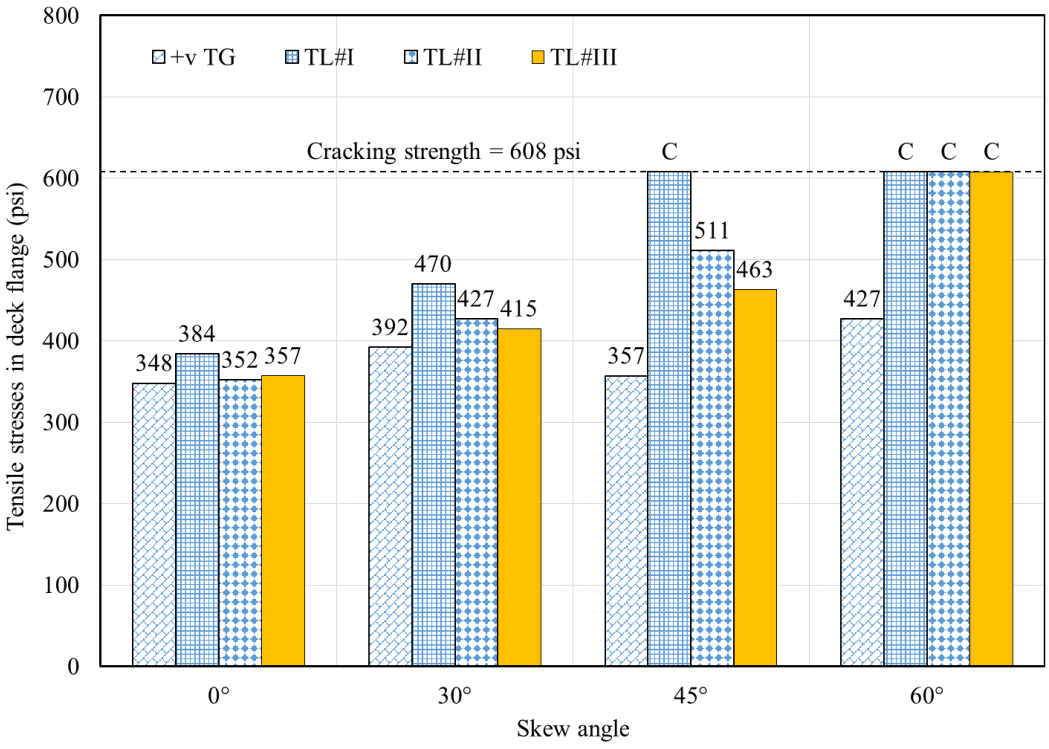

Figure 4.4-19 Effect of increasing skew angle on maximum principal stresses in deck flange

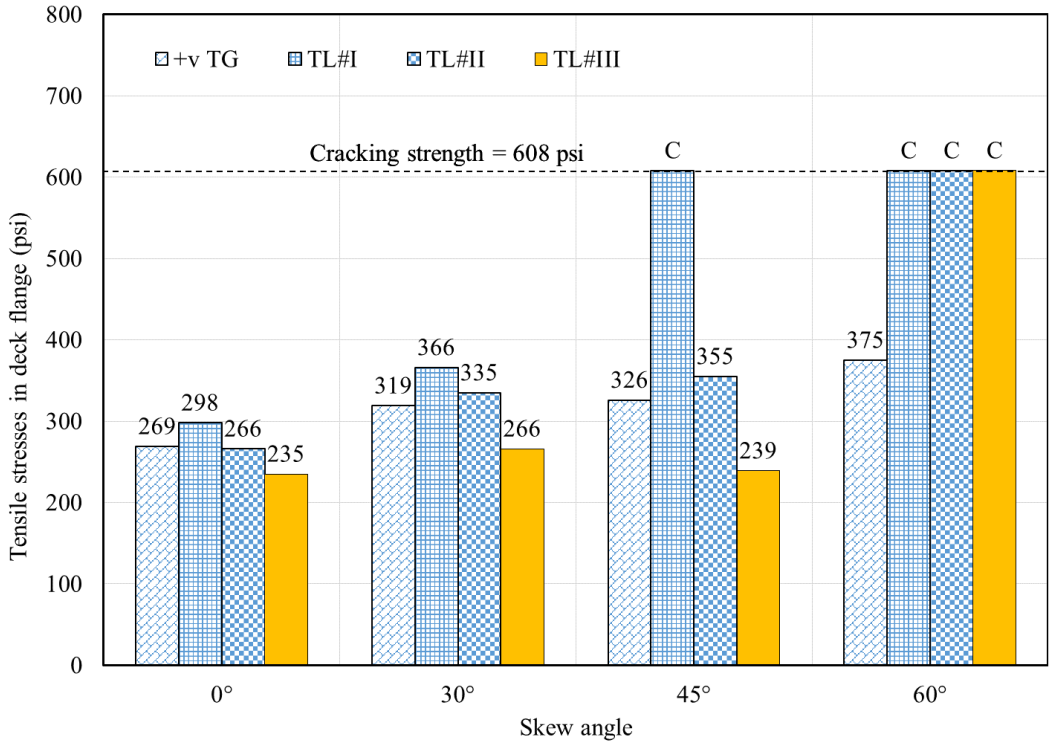

Figure 4.4-20 Effect of increasing skew angle on Longitudianl stresses in deck flange

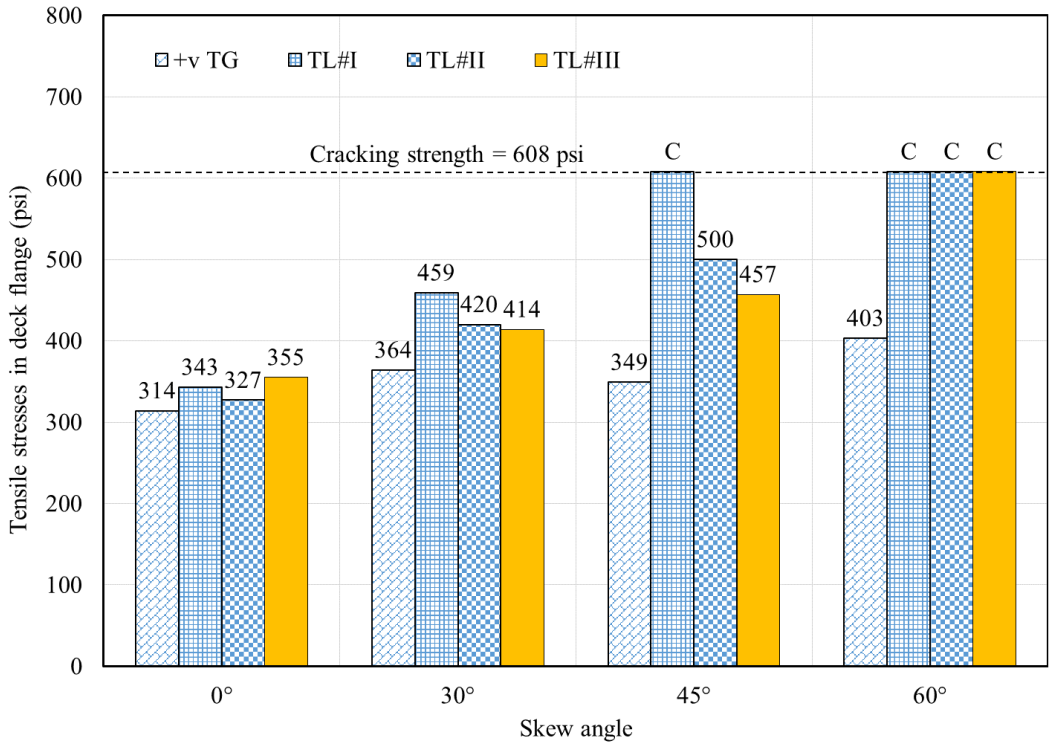

Figure 4.4-21 Effect of increasing skew angle on transverse stresses in deck flange

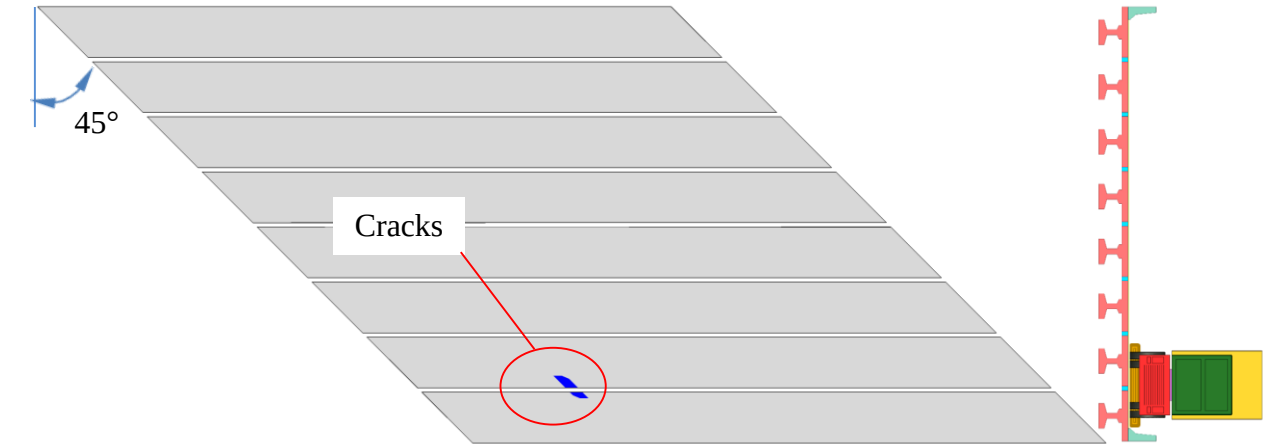

Figure 4.4-22 Development of shear key cracks in bridges with a skew angle of 45° under TL#I

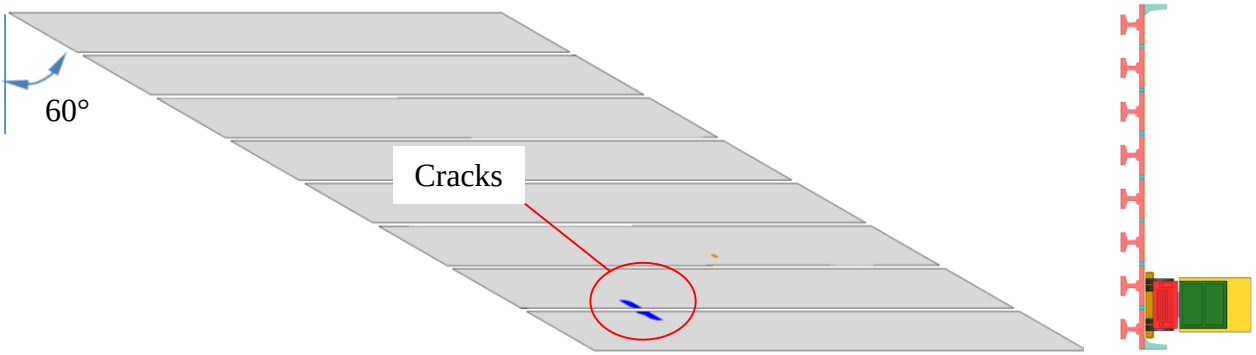

Figure 4.4-23 Development of shear key cracks in bridges with a skew angle of 60° under TL#I

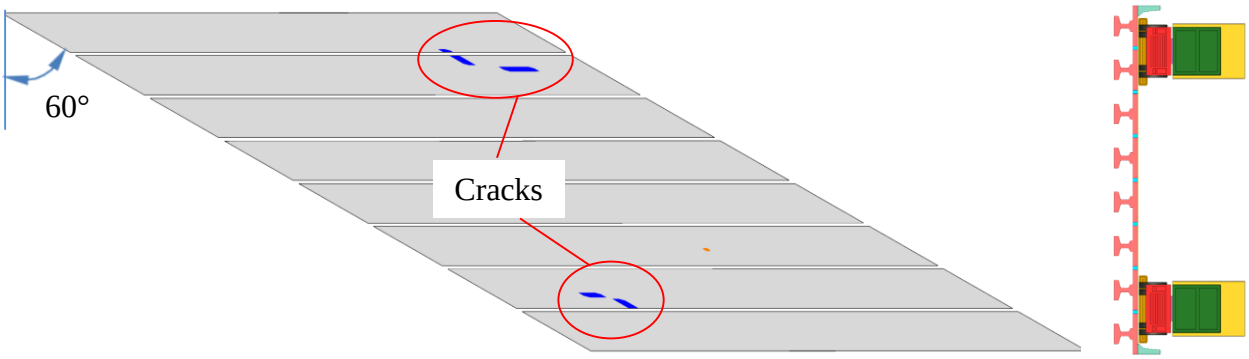

Figure 4.4-24 Development of shear key cracks in bridges with a skew angle of 60° under TL#II

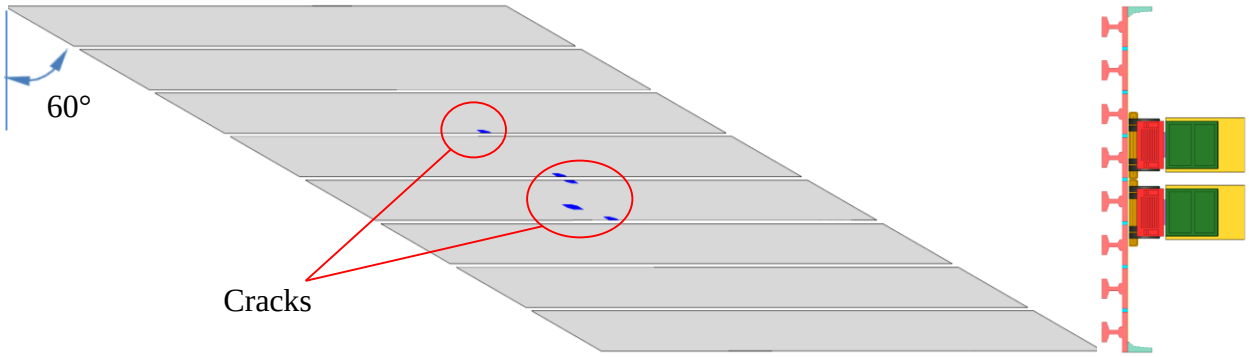

Figure 4.4-25 Development of shear key cracks in bridges with a skew angle of 60° under TL#III

4.4.6 Effect of TPT force

To evaluate the influence of providing TPT force on the lateral integrity of decked bulb T beam bridges, select bridge models were analyzed with TPT forces of 50, 100, 150, and 200 kip per diaphragm. All bridge models were provided with five equally spaced transverse diaphragms. To ensure the uniformity of the TPT through the section, the force was applied as a distributed load over the exterior face of the diaphragm.

Figure 4.4-26 through Figure 4.4-37 show the developed stresses in the deck flange of the bridge models. As shown in the figures, the effect of the TPT force was not highly significant. In general, the principal stresses in the deck flanges did not exhibit a significant change with adding the TPT force. In some models, the principal stresses tended to slightly decrease with increasing the TPT force level. In other models, the maximum principal stresses actually increased with increasing the TPT force level. The change in the maximum principal stresses whether a increase or a decrease never exceeded the limit of 100 psi.

The longitudinal tensile stresses in the deck seem to slightly increase with increasing the TPT force. This is due to the fact that TPT force usually generates a field of compressive stresses in the transverse direction, which are accompanied by tensile stresses in the longitudinal direction. Because of the longitudinal prestressing force, the top flange of the decked bulb T beam experiences longitudinal tensile stresses especially at the ends, where the moment due to the dead and live loads diminishes. Therefore, adding the TPT force, especially at the end diaphragms, seems to increase the longitudinal tensile stresses. The maximum increase in the longitudinal stresses in the deck flange did not exceed 50 psi.

On the other hand, it was noticed that the transverse tensile stresses in general decreased with increasing the TPT force. A decrease of transverse tensile stresses of approximately 150 psi was noted in some cases of loading (case of bridges with a span of 50 ft, a width of 51.5 ft, a TPT force of 200 kip per diaphragm, under TL#I). However, the decrease in the transverse tensile stresses was accompanied by an increase of the longitudinal tensile stresses, and overall, the maximum principal stresses for this particular case increased by around 71 psi.

Table 4.4-19, through Table 4.4-21 document the change in the tensile stresses in the deck flange with increasing the TPT force from zero to 200 kip per diaphragm for bridges with different spans and different widths. A direct relationship between the bridge span or width and the developed stresses with adding TPT force was not observed. The maximum principal stresses in the deck flange usually exceeded the limit of 300 psi but they were less than the limit of 500 psi under any load combination with different TPT force levels. This is considering a concrete cracking strength of 608 psi (According to AASHTO LRFD for typical 7000-psi concrete). It should be noted that the tensile stresses in the deck can be controlled by limiting the longitudinal tensile stresses in the deck due to longitudinal prestressing.

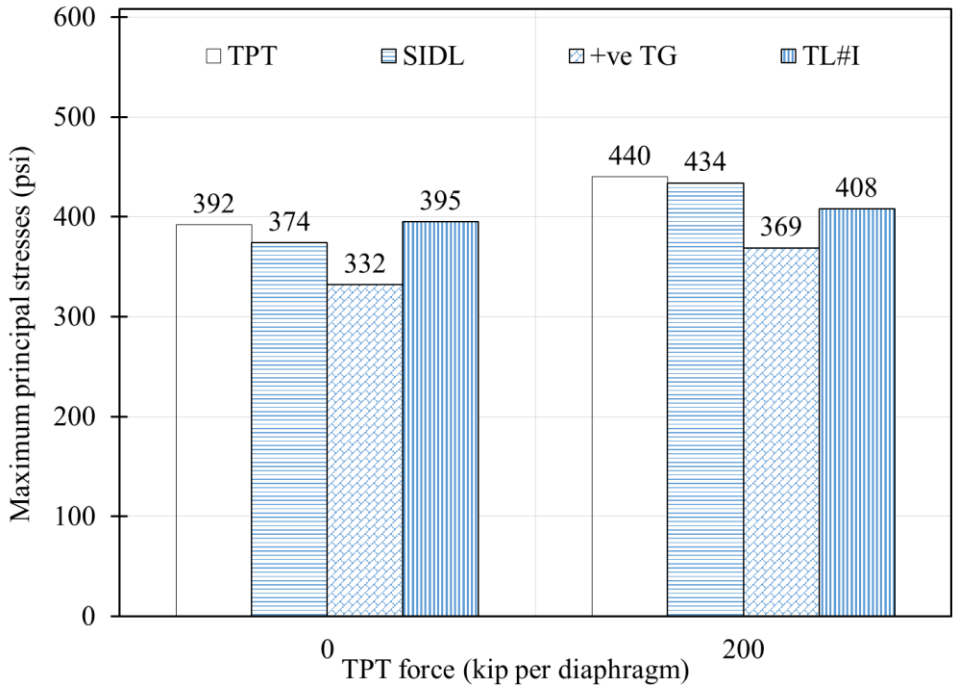

Figure 4.4-26 Maximum principal stresses in deck flange at different TPT force levels in bridge models with a span of 50 ft and a width of 25.5 ft

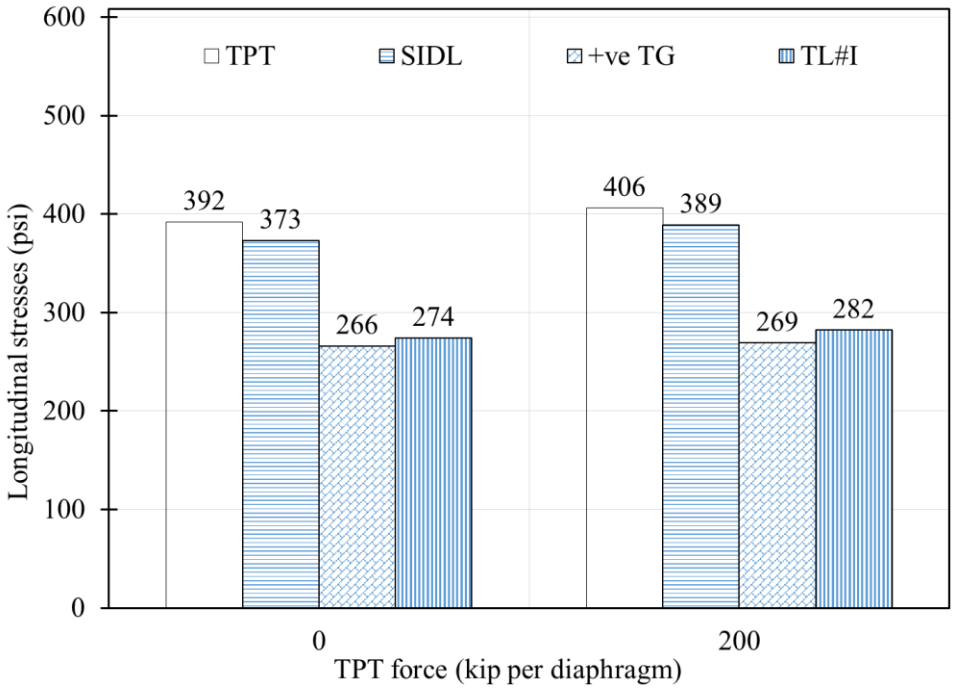

Figure 4.4-27 Longitudinal stresses in deck flange at different TPT force levels in bridge models with a span of 50 ft and a width of 25.5 ft

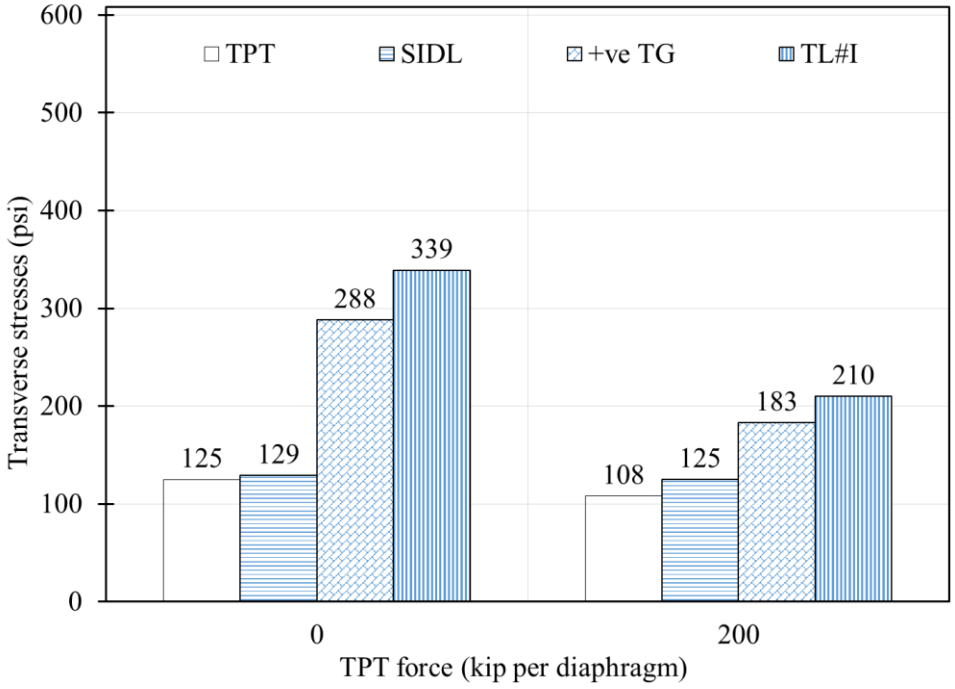

Figure 4.4-28 Transverse stresses in deck flange at different TPT force levels in bridge models with a span of 50 ft and a width of 25.5 ft

Table 4.4-19 Deck flange stresses at different TPT force levels in bridge models with a span of 50 ft and a width of 51.5 ft

	Maximum principal stresses (psi)			Longitudinal stresses (psi)			Transverse stresses (psi)		
TPT (kip/Diaph.)	0	100	200	0	100	200	0	100	200
TPT	392	431	470	392	413	434	125	110	95
SIDL	388	434.5	481	387	408	436	137	123	114
+ve TG	347	383	419	293	301	309	334	286	238
TL#I	416	452	487	310	321	331	389	314	239
TL#II	407	436	464	296	310	321	399	356	313
TL#III	309	341	373	247	257	267	282	235	181

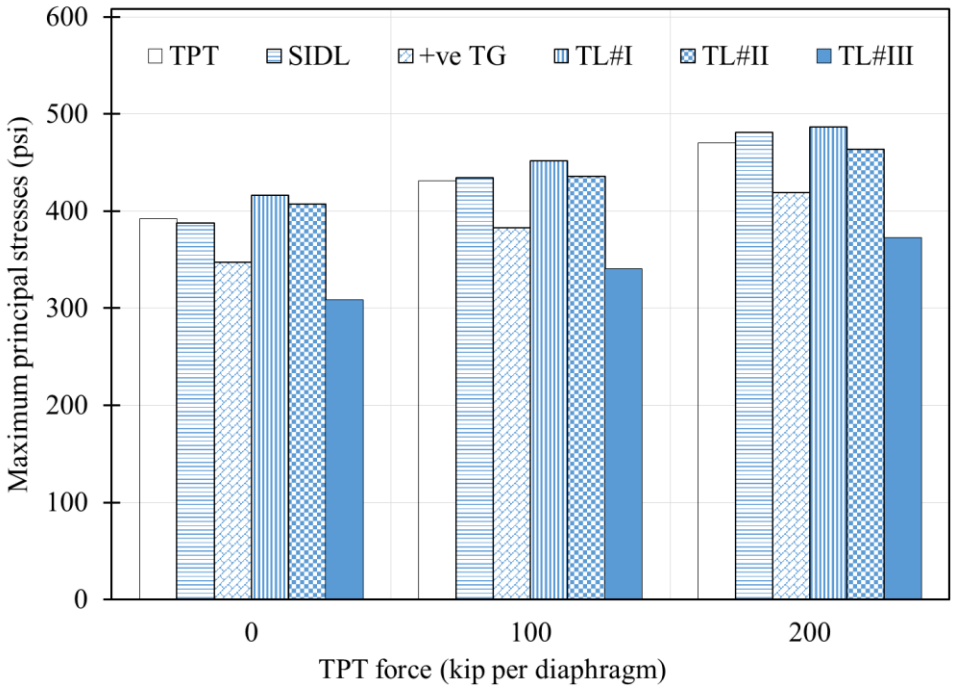

Figure 4.4-29 Maximum principal stresses in deck flange at different TPT force levels in bridge models with a span of 50 ft and a width of 51.5 ft

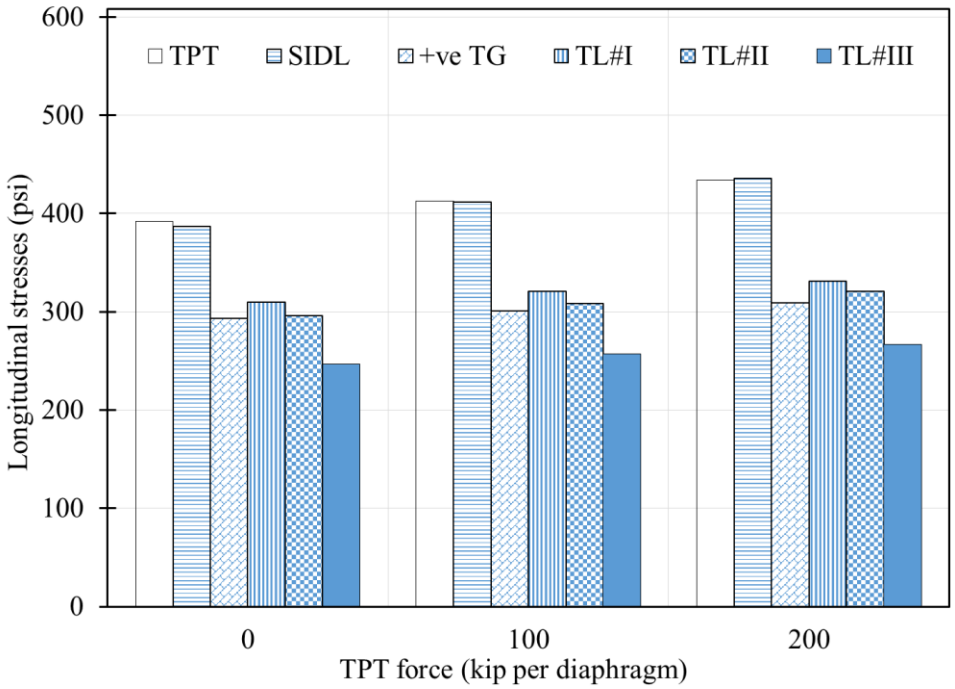

Figure 4.4-30 Longitudinal stresses in deck flange at different TPT force levels in bridge models with a span of 50 ft and a width of 51.5 ft

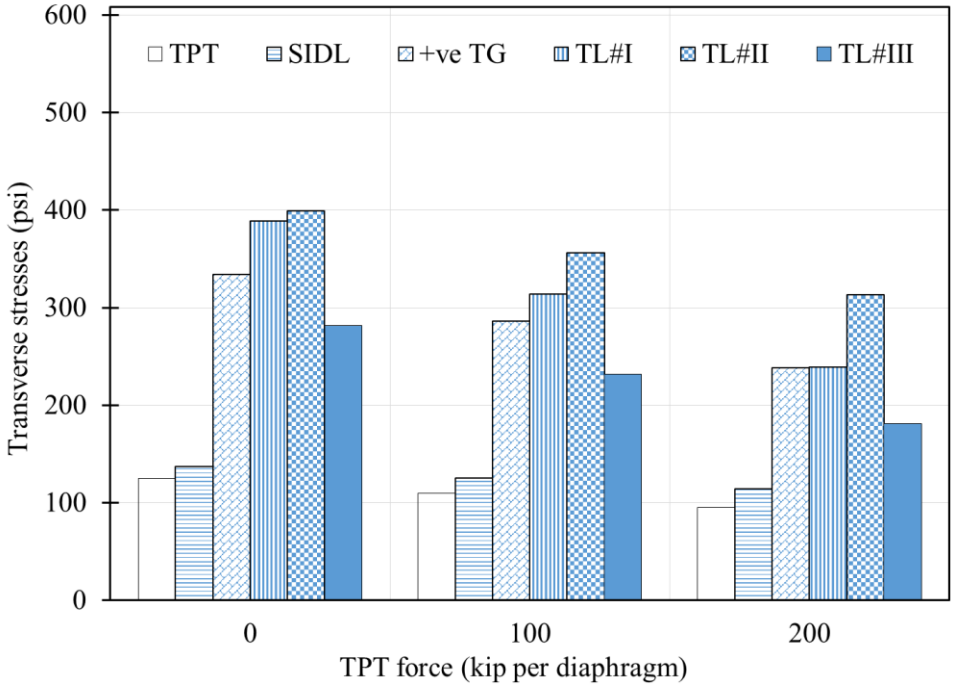

Figure 4.4-31 Transverse stresses in deck flange at different TPT force levels in bridge models with a span of 50 ft and a width of 51.5 ft

Table 4.4-20 Deck flange stresses at different TPT force levels in bridge models with a span of 75 ft and a width of 51.5 ft

	Maximum principal stresses (psi)					Longitudinal stresses (psi)					Transverse stresses (psi)				
TPT (kip/Diaph.)	0	50	100	150	200	0	50	100	150	200	0	50	100	150	200
TPT	357	363	373	385	398	357	362	369	376	384	110	85	58	46	57
SIDL	360	369	381	394	408	358	365	372	379	386	118	94	68	65	76
+ve TG	348	355	363	371	380	269	272	276	279	283	314	304	293	283	273
TL#I	384	397	409	422	434	298	302	305	308	311	343	329	317	306	295
TL#II	352	362	372	382	395	266	268	271	275	279	327	317	307	297	286
TL#III	357	359	362	364	367	235	239	243	247	252	355	335	315	295	276

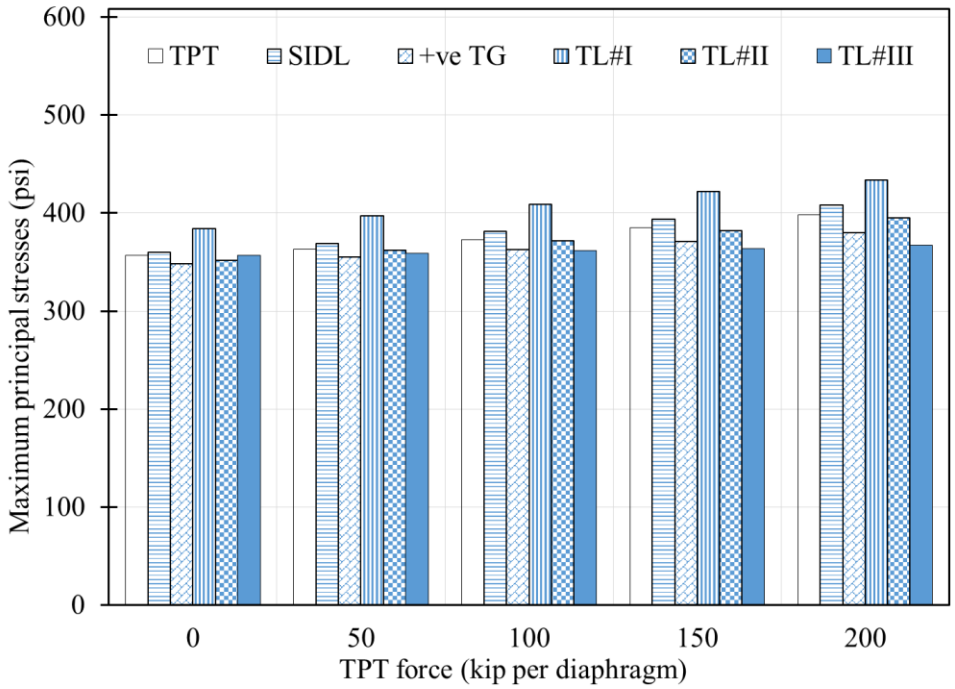

Figure 4.4-32 Maximum principal stresses in deck flange at different TPT force levels in bridge models with a span of 75 ft and a width of 51.5 ft

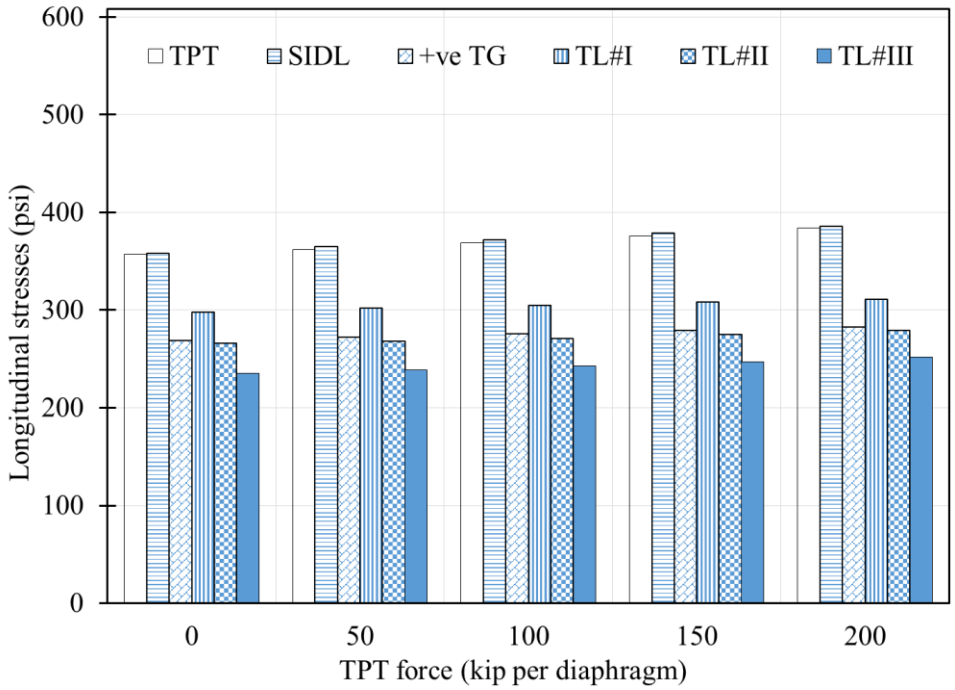

Figure 4.4-33 Longitudinal stresses in deck flange at different TPT force levels in bridge models with a span of 75 ft and a width of 51.5 ft

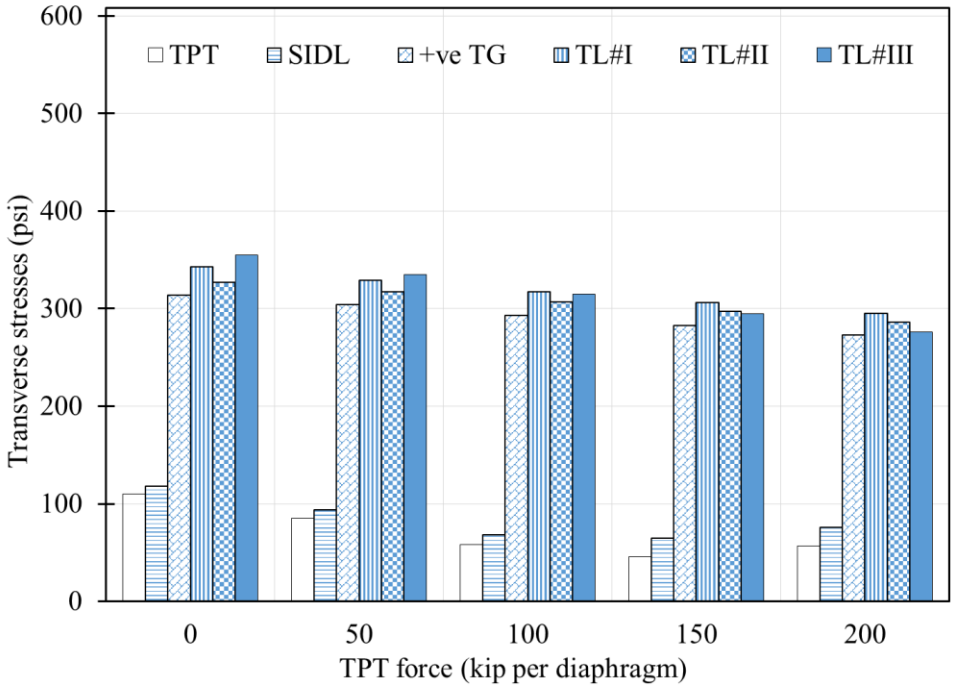

Figure 4.4-34 Transverse stresses in deck flange at different TPT force levels in bridge models with a span of 75 ft and a width of 51.5 ft

Table 4.4-21 Deck flange stresses at different TPT force levels in bridge models with a span of 100 ft and a width of 77.5 ft

	Maximum principal stresses (psi)				Longitudinal stresses (psi)				Transverse stresses (psi)			
TPT (kip/Diaph.)	0	50	100	200	0	50	100	200	0	50	100	200
TPT	355	332	341	359	354	331	339	355	103	73	63	43
SIDL	366	334	344	364	364	330	338	353	124	90	83	67
+ve TG	351	407	413	426	274	278	287	306	347	324	320	309
TL#I	-	-	-	-	-	-	-	-	-	-	-	-
TL#II	469	398	405	415	296	280	282	286	467	352	340	321
TL#III	358	373	388	403	237	249	273	287	356	344	322	309

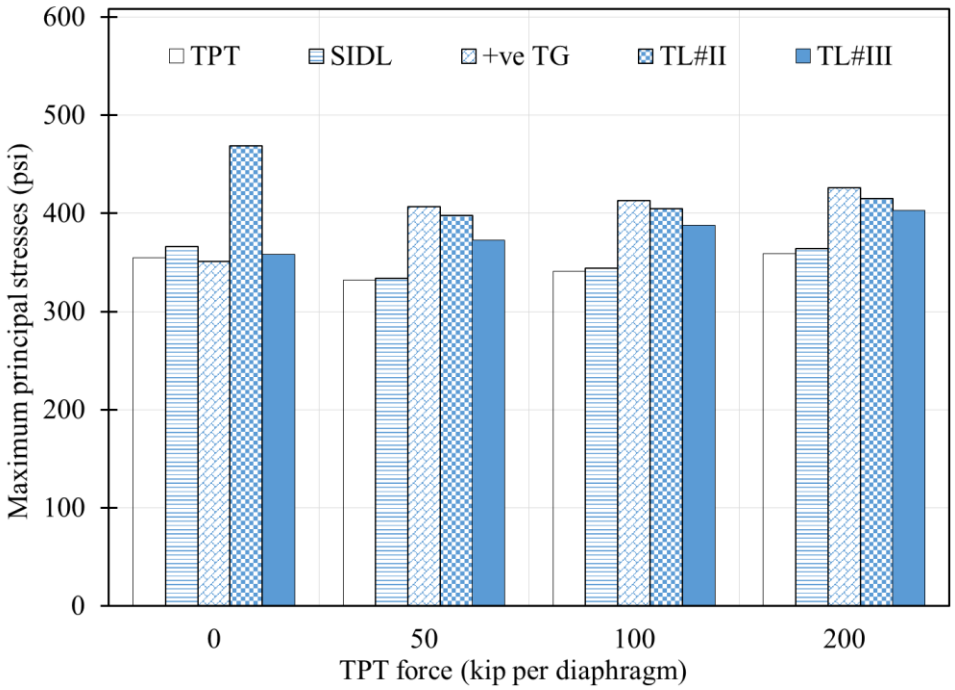

Figure 4.4-35 Maximum principal stresses in deck flange at different TPT force levels in bridge models with a span of 100 ft and a width of 77.5 ft

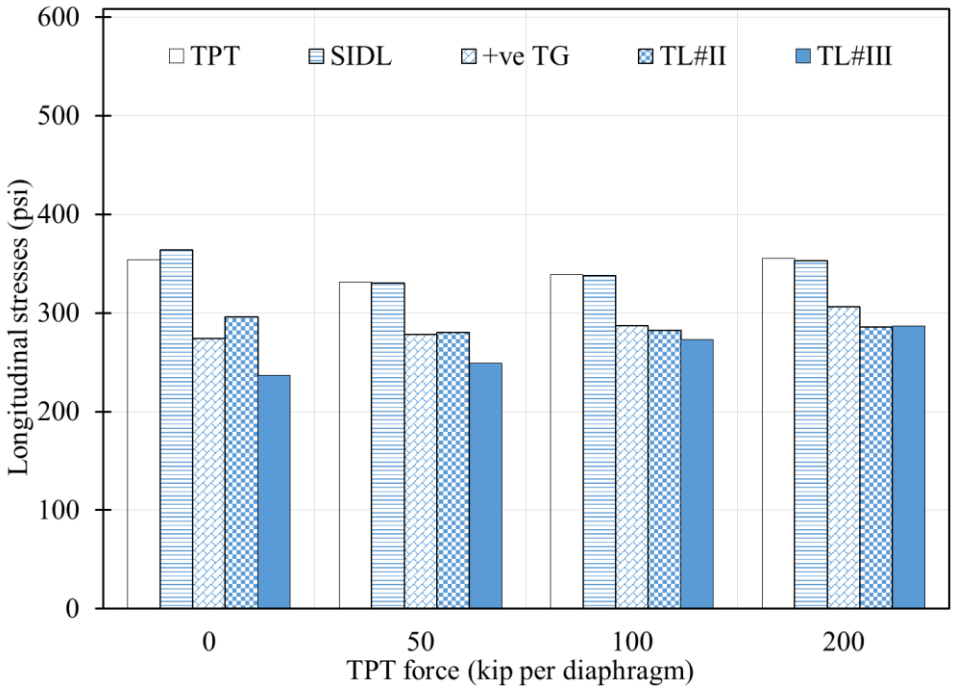

Figure 4.4-36 Longitudinal stresses in deck flange at different TPT force levels in bridge models with a span of 100 ft and a width of 77.5 ft

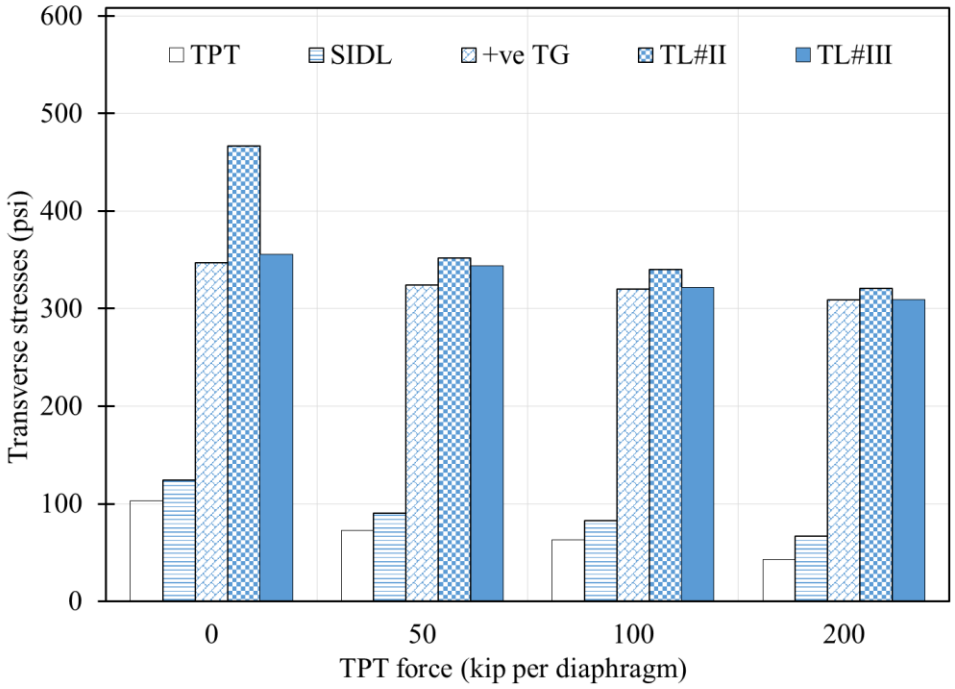

Figure 4.4-37 Transverse stresses in deck flange at different TPT force levels in bridge models with a span of 100 ft and a width of 77.5 ft

4.5 Summary

The results from the numerical analysis suggest that it is feasible to numerically and analytically predict the performance of beams and bridges with CFCC reinforcement with very good accuracy. The overall performance of such beams and bridges follows the principles of strain compatibility and force equilibrium through the section. In addition, decked bulb T beam bridges with UHPC shear key joints can be safely used in bridge construction with no deck slab. However, it is mandatory to provide transverse diaphragms along with the shear key joints. Without transverse diaphragms, the joints between the top flanges become the sole path for load transfer among the adjacent beams, resulting in additional stresses, which may crack the joints under positive temperature gradient and traffic loads. Even with the use of UHPC shear key joint, which exhibit exceptional bond strength to concrete, the cracks may develop on the concrete side of the joint. Providing shear key reinforcement is believed to be a viable line of defense against crack propagation. However, the development of cracks over time and under repeated load cycles can lead to series consequences and greatly reduce the lifespan of the joints and the entire superstructure.

Through the parametric study, it was determined that five equally spaced transverse diaphragms are sufficient to mitigate the longitudinal crack development in decked bulb T beams with spans ranging from 50 to 100 ft and widths ranging from 25 to 77 ft. The bridges were subjected to positive temperature gradient and traffic loads at different locations. For bridges with spans and widths exceeding the aforementioned ranges, it may be mandatory to increase the number of diaphragms.

In addition, the parametric study also showed that decked bulb T beam bridges with a skew angle are prone to shear key cracking. Cracks were observed in bridges with skew angles of 45° and larger. Therefore, it is highly recommended that decked bulb T beam bridge system be used with a skew angle of no more than 30°. Bridges with larger skew angles will need a special evaluation to ensure the integrity.

Furthermore, the study showed that providing transverse post-tensioning through the transverse diaphragms may not serve its purpose of mitigating the tensile stresses in the deck flange. It was observed that while the transverse post-tensioning force reduced the transverse tensile stresses in bridge models with different spans and widths under different load combinations,

it also generated a field of longitudinal tensile stresses. Since the flanges of the decked bulb T beams experience tensile stresses due to the longitudinal prestressing especially at the ends, adding transverse post-tensioning increases the overall longitudinal tensile stresses. Consequently, the maximum principal stresses in the deck flanges seem to slightly increase with adding the post-tensioning force. This increase in principal stresses may lead to the development of deck cracking (not necessarily at the shear key joints). Therefore, transverse post-tensioning needs not to be provided during construction but it may be reserved for future use, when integrity of the superstructure is jeopardized. For example, post-tensioning can be used to ensure the integrity of the superstructure after a beam replacement or when additional beams are provided. It is recommended that post-tensioning ducts through the transverse diaphragms be provided during construction for any possible future use.

CHAPTER 5: SUMMARY AND CONCLUSIONS

5.1 Summary of the work

Through this experimental/numerical investigation, a new decked bulb T beam bridge system with non-corrosive CFCC reinforcement and UHPC shear key joints was evaluated. The experimental investigation included building one-half-scale five individual control beams and one-half-scale complete bridge model. Four control beams were tested to failure under four-point flexural loading and one beam was tested to failure under shear loading. The bridge model was tested under different load levels and configurations to evaluate its performance under service, post-cracking, and strength limit states. Special attention was given to the performance of the UHPC shear key joints and to the integrity of the bridge model in the transverse direction.

The numerical study consisted of a verification phase and a parametric phase. In the verification phase, numerical models model were generated and analyzed for tested control beams and the bridge model. The results from the numerical study were compared with those of the experimental study to ensure the accuracy of the numerical models. After validation of the numerical models, the parametric study was initiated by generating a series of models for full-scale decked bulb T beam bridges with spans ranging from 50 ft to 100 ft and widths ranging from 24 ft to 78 ft. The main objective of the parametric study was to evaluate the transverse integrity of decked bulb T beam bridge system and to assess the need for transverse diaphragms and/or transverse post-tensioning. In addition, the study was extended to examine the effect of the skew angle on the stress distribution in the beams and the potential for developing longitudinal deck cracks at the shear key joints

5.2 Observations & conclusions

The following observations and conclusions are drawn based on the results of the experimental investigation:

1. Decked bulb T beams with CFCC reinforcement can be designed as under-reinforced, balanced, or over-reinforced. The difference in the ductility ratio did not vary significantly with reference to the design of the section. It was observed that the ductility ratio in all control beams with CFCC reinforcement averaged approximately 30 %, while the ductility ratio of control beam with steel strands was around 70 %. However, by examining the load

deflection curves, it was observed that beams with CFCC strands exhibited significant deflection at failure. This maximum deflection was similar to that observed in the beam with steel strands. This large deflection at failure, along with the extensive cracking, can serve as a clear visual sign before failure.

2. It was also observed that due to construction configuration of CFCC strands, the tension failure in Beam C-S-F-U did not occur suddenly. Rather, the 7-wire CFCC strands showed a gradual failure as the individual wires within the strands experienced consecutive rupture without dramatic decrease in the overall load carrying capacity.

3. The flexural failure of all control beams was accurately predicted using the method of strain compatibility. However, special attention must be made when evaluating the type of failure. In beams with multiple layers of non-prestressed and prestressed CFCC strands, the equation of balanced reinforcement ratio as recommend by ACI-440 (2006) can only be used as a rough estimate during the initial design stage. Exact failure mode can only be verified using the strain compatibility method considering the distribution of the strands and prestressing force through different reinforcement layers.

4. It is fairly accurate to assume that decked bulb T beams exhibit a bilinear load-deflection relationship. The slope of the first segment of the bilinear curve represents the flexural stiffness of the un-cracked section, while the slope of the second segment represents the flexural stiffness of the cracked section. When conducting multiple post-cracking load cycle tests, the segments of the bilinear curve meet at the decompression load, defined as the load required to decompress the beam and cause the strain in the bottom fibers of the beam to reach zero.

5. Decked bulb T beams with CFCC stirrups exhibited shear compression failure with no signs of yielding or rupture of stirrups. The failure occurred in the web struts due to excessive shear strain. The maximum recorded strain in the CFCC stirrups was approximately 0.0035, which is the maximum shear strain as given in AASHTO LRFD regardless of the type of reinforcement. This finding suggests that the strain limit of 0.002 as given in ACI 440-3R is overly conservative and needs to be changed to match that of AASHTO LRFD.

6. Under service load condition, the decked bulb T beam bridge model did not exhibit any flexural or shear key cracks. The service load was transversely distributed among the beams in a pattern similar to that of bridges with cast-in-place deck slab. The addition of transverse post-tensioning did not seem to affect the load distribution at the service limit stage. No signs of shear key distress or longitudinal shear key cracks were observed.

7. Beyond cracking, the distribution of the load followed a similar pattern to that before cracking. No signs of shear key failure were observed. The load distribution factor beyond cracking was similar to that before cracking. Similarly, transverse post-tensioning did not seem to affect the load distribution among the beams at this stage of loading.

8. To evaluate the shear key capacity, it was decided to partially crack the shear key joint by loading one of the exterior beams in the bridge model under four point-loading. The beam was loaded to approximately twice its load carrying capacity without any shear key cracking. After further increasing the load, minor cracks around the shear key joints developed. However, all the cracks were localized at the concrete side of the joint and did not seem to propagate uniformly. The most noticeable crack developed in the diaphragm joining the exterior beam to the rest of the bridge model at the mid-span. It was therefore concluded that UHPC shear key joints without transverse post-tensioning can promote the integrity of decked bulb T beam bridges given that adequate number of UHPC transverse diaphragms are provided.

9. The bridge model was loaded under four-point loading in load cycles to 160 kip, which represented 80 % of its estimated maximum load carrying capacity. The performance of the bridge model was similar to those of the control beams. The load-deflection curves demonstrated a bilinear relationship with the decompression load marking the change of slope on the bilinear curve.

10. The strength limit state testing included loading the center beam of the bridge model under four-point loading to failure. The failure took place at a load level of 220 kip. The failure started with the rupture of the prestressed CFCC strands in the loaded beam, followed by the rupture of the CFCC strands in the adjacent beams, and finally the strands in the exterior beams. The rupture of the strands was accompanied by a loud popping sound, significant cracks, and spalling of the concrete. The failure, therefore, was classified as a tension

failure. After failure, the shear key joints were inspected. It was noticed that hairline shear cracks developed at the mid-span around the shear key joints of the loaded beam. Nevertheless, the deflection of the bridge model at the maximum load showed a uniform load distribution between the beams. This suggested that these cracks developed only after the failure of the prestressing strands in the loaded beam. Overall, it is reasonable to conclude that UHPC shear key joints and UHPC transverse diaphragms were sufficient to transfer the load laterally even at the ultimate load.

The following observations and conclusions were drawn based on the results of the numerical investigation:

1. The results from the developed comprehensive numerical models for the control beams and the bridge model fairly matched the experimental results and showed a difference of less than 10%.

2. The parametric study included modeling full-scale decked bulb T beam highway bridges with various spans, widths, and skew angles, and analyzing the bridges under positive temperature gradient and under traffic loads. Both temperature gradient and traffic loads were adopted from AASTHO LRFD (2012).

3. The analysis of different highway bridges under temperature gradient alone revealed that when the bridges are exposed to positive temperature gradient, tensile stresses develop near the shear key joints. If no diaphragms are provided, the tensile stresses seem to accumulate at the ends of the simply supported bridges.

4. Adding end diaphragms has a significant influence on the development of the tensile stresses around the shear key joints. It was noticed that with adding the end diaphragms, the tensile stresses migrated from the ends to the mid-region of the bridge and they became more uniform. However, adding intermediate diaphragms did not seem to influence the distribution of the tensile stresses due to positive temperature gradient stresses any further. Therefore, it is concluded that end diaphragms are mandatory in decked bulb T beam bridges to avoid the development of shear key cracks at the ends of the bridge.

5. The traffic load (AASHTO LRFD HL-93 vehicular loading with impact allowance) was applied to the bridge model at three locations: in Location I, the vehicular loading was

applied next to the parapet at one side of the bridge. In Location II, two vehicular loadings were applied next to the parapets at both sides of the bridge model. In Location III, two vehicular loadings were applied at the mid-width of the bridge model. In the longitudinal direction, all the traffic loads were positioned as to induce the maximum bending moment of the span.

6. Positive temperature gradients with vehicular loading at Locations I and II resulted in increasing the tensile stresses near the ends of bridges with no transverse diaphragms. Adding two end diaphragms mitigated the development of tensile stresses and eliminated the potential of shear key cracking. The addition of intermediate diaphragms did not seem to influence the stress level at the ends of the bridge under this particular loading case.

7. When applying positive temperature gradient with vehicular loading at Location III, the tensile stresses developed along the span with a concentration at the middle region of the span under the truck loading. Adding end diaphragms did not seem to decrease the tensile stresses, while adding intermediate diaphragms significantly reduced the tensile stresses.

8. Bridges with skew angle exhibited an increase in tensile stresses at the shear key joints with the concentration of the tensile stresses near the corners when vehicular loading was at Locations I and II, and near the middle region of the span when vehicular loading was at Location III. As a results, it is recommended that decked bulb T beam bridge systems without TPT should not be used for a skew angle of 45 degrees or higher.

9. Overall, it was determined from the numerical investigation that for decked bulb T beam bridges with span range from 50 to 100 ft, five equally spaced transverse diaphragms would be sufficient to eliminate the shear key cracks. No TPT force is necessary. The same number of diaphragms can be used with a skew angle of 30 degrees. However, analysis of bridges with skew angles of 45 and 60 degrees showed shear key cracking under one or more load cases.

10. Applying TPT in decked bulb T beam bridges with no skew generated a field of transverse compressive stresses in the deck flange. The compressive stresses ranged between 20 to 100 psi with TPT of 50 to 200 kip/diaphragm in five diaphragms. This compressive field seemed to relieve some of the tensile stresses around the shear key joints but it was noticed

that this relief was maximized near the mid-span and minimized near the ends of the span. Overall, due to the increase in the longitudinal tensile stresses that accompanied the application of transverse post-tensioning force, the maximum principal stresses in the deck flange did not decrease and therefore, the probability of crack development remained unchanged.

5.3 Recommendations

Based on the experimental and numerical investigations, the following recommendations are drawn:

1. Based on the literature review, bulb T beams are routinely used by several states and a few states have successfully constructed decked bulb T beam bridges in their implementation for accelerated bridge construction. In addition, the comprehensive numerical models compared well to the control beams and showed a uniform distribution for traffic loads among the adjacent beams. Therefore, it is recommended that state DOT's consider Decked bulb T beam as a viable option in their bridge construction.
2. The overall procedure for the construction of CFCC decked bulb T beams is fairly simple and quick. CFCC strands are lighter than steel and they are easy to handle. However, special care shall be made to avoid shearing the strands or scratching them.
3. The coupler system of prestressed CFCC strands, while effective, is time consuming and it is strongly recommended that a simpler CFCC anchorage system be developed, tested, and verified to expedite construction process.
4. The long-term performance of CFCC strands is a crucial element in bridge performance and must be thoroughly examined and investigated. A research investigation is currently underway at Lawrence Technological University to establish a complete performance profile for CFCC material, determine the appropriate design factors, and ensure the longevity and safety of bridges with CFCC strands.

REFERENCES

1. AASHTO, 2007, "AASHTO LRFD Bridge Design Specifications," 4th ed., American Association of State Highway and Transportation Officials, Washington, DC.
2. AASHTO T 259-02, 2002, "Standard Method of Test for Resistance of Concrete to Chloride Ion Penetration," American Association of State Highway and Transportation Officials, Washington, DC.
3. Abdelrahman, A. and Rizkalla, S., 1999, "Deflection Control of Concrete Beams Pretensioned by CFRP Reinforcements," Journal of Composites for Construction, ASCE, Vol. 3, No. 2, May, pp. 55 -62.
4. American Concrete Institute (ACI), 2004, "Prestressing Concrete Structures with FRP Tendons." ACI 440.4R-04, Farmington Hills, MI.
5. American Concrete Institute (ACI), 2006, "Guide for the Design and Construction of Structural Concrete Reinforced with FRP Bars." ACI 440.1R-06, Farmington Hills, MI.
6. ASTM Standard C496, 2011, "Test Method for Splitting Tensile Strength of Cylindrical Concrete Specimens," ASTM International, West Conshohocken, PA, USA. DOI: 10.1520/C0882_C0882M-05E01, www.astm.org.
7. ASTM Standard C882, 2005, "Test Method for Bond Strength of Epoxy-Resin Systems Used With Concrete by Slant Shear," ASTM International, West Conshohocken, PA, USA. DOI: 10.1520/C0496_C0496M-11, www.astm.org.
8. ASTM Standard C666, 2008, "Test Method for Resistance of Concrete to Rapid Freezing and Thawing," ASTM International, West Conshohocken, PA, USA. DOI: 10.1520/C0666_C0666M-03R08, www.astm.org.
9. ASTM Standard C944, 2005, "Test Method for Abrasion Resistance of Concrete or Mortar Surfaces by the Rotating-Cutter Method," ASTM International, West Conshohocken, PA, USA. DOI: 10.1520/C0944_C0944M-99R05E01, www.astm.org.
10. Bache, H., 1981, "Densified Cement/Ultra-Fine Particle-Based Materials," CBL Report No. 40. Aalborg Portland, Denmark.

11. Badwan, I. and Liang R., 2007, “Performance Evaluation of Precast Posttensioned Concrete Multibeam Deck,” J. Perform. Constr. Facil. Vol. 21, Issue 5, pp. 368: 374

12. Bakht, B.; Jaeger L.G.; and Cheung M.S., 1983, “Transverse Shear in Multi Beam Bridges,” Journal of Structural Engineering, Vol. 109, No. 4, April, pp. 936–949.

13. Bhide, S., 2008, "Material Usage and Condition of Existing Bridges in the US", Portland Cement Association, PCA Report, No. SR34204, Skokie, Illinois, USA.

14. Collins, M.P.; Mitchell, D.; and Macgregor, J.G., 1993, "Structural Design Considerations for High-Strength Concrete," Concrete International, American Concrete Institute, Vol. 15, No. 5, May, pp. 27–34.

15. Dolan, C.W. and Swanson, D., 2002 “Development of Flexural Capacity of a FRP Prestressed Beam with Vertically Distributed Tendons,” Composites Part B: Engineering, Vol. 33, Issue 1, January, pp. 1-6.

16. Ebeido, T. and Kennedy J., 1996, “Girder Moments in Continuous Skew Composite Bridges,” Journal of Bridge Engineering, Vol. 1, No. 1, Feb., pp. 37-45

17. El-Remaily, A.; Tadros, M.K.; Yamane T.; and Krause, G., 1996, “Transverse Design of Adjacent Precast Prestressed Concrete Box Girder Bridges,” PCI Journal, V. 41, No. 4 , July–August, pp. 96–112.

18. El-Sayed, A.K.; El-Salawaky, E.F.; and Benmokrane, B., 2006 “Shear Capacity of High-Strength Concrete Beams Reinforced with FRP Bars,” ACI Structural Journal, Vol. 103, No. 3, May-June, pp. 383-389.

19. Fam, A.Z.; Rizkalla, S.H.; and Tadros, G., 1997 “Behavior of CFRP for Prestressing and Shear Reinforcements of Concrete Highway Bridges,” ACI Structural Journal, Vol. 94, No. 1, January-February, pp. 77-86.

20. French, C.E.; Shield, C.K.; Klaseus, D.; Smith, M.; Eriksson, W.; Ma, Z.J.; Zhu, P.; Lewis, S.; and Chapman, C; 2011, “Cast-in-Place concrete Connections for Precast Deck Systems,” Final Report, NCHRP No. 173, web-only Document 173, www.trb.org.

21. Gilberston, C.U.; Attanayake, T.; Ahlborn; and Aktan. H., 2006, "Prestressed Concrete Box-Beam Bridge Performance: Condition Assessment and Design Analysis," Transportation Research Board (TRB), Washington, D.C., U.S.A..

22. Grace, N.F.; Soliman, A.K.; Abdel-Sayed, G.; and Saleh, K.R., 1998, "Behavior and Ductility of Simple and Continuous FRP Reinforced Beams," Journal of Composites for Construction, Vol. 2, No. 4, November, pp. 186-194.

23. Grace and Abdel-Sayed, 1999, "Mathematical Solution of Skew Bridges Prestressed with CFRP Strands," ACI Structural Journal, V. 96, No. 69, Nov.-Dec.

24. Grace, 1999, "Innovative CFRP Continuous Prestressed Concrete Bridges," ACI Concrete International, V. 21, No. 10, Oct.

25. Grace; Abdel-Sayed; Soliman; and Sale, 1999, "Strengthening Reinforced Concrete Beams Using Fiber Reinforced Polymer CFRP Laminates," ACI Structural Journal, V. 96, No. 5, Sept.-Oct.

26. Grace; Enomoto, T.; and Yagi, K., 2002, "Behavior of CFCC and CFRP Leadline Prestressing Systems in Bridge Construction," PCI JOURNAL, Vol. 47, No. 3, May/June.

27. Grace; Abdel-Sayed; Navarre; Nacey; Bonus; and Collavino, 2003, "Full-Scale Test of Prestressed Double-Tee Beam," ACI-Concrete International, Vol. 25, No. 4, April.

28. Grace, N.F. and Singh, S.B. 2003 "Design Approach for Carbon Fiber-Reinforced Polymer Prestressed Concrete Bridge Beams," ACI Structural Journal, Vol. 100, No.3, May, pp. 365-376.

29. Grace, N.F.; Roller, J.J.; Navarre, F.N.; Nacey, R.B.; and Bonus, W., 2005, "Truck Load Distribution Behavior of the Bridge Street Bridge, Southfield, Michigan," PCI Journal, Vol. 50, No. 2, March/April, pp.76-89.

30. Grace, N.F.; Jensen, E.; Matsager, V.; Bebawy, M.; Hanson, J.; and Soliman, E., 2008, "Use of Un-bonded CFCC for Transverse Post-Tensioning of Side-by-Side Box-Beam Bridges," Technical Report, Michigan Department of Transportation, Lansing, MI.

31. Graybeal, B.A., 2006, "Material Property Characterization of Ultra-High Performance Concrete," Report No. FHWA-HRT-06-103, August, McLean, VA.

32. Graybeal, B.A., 2006, "Structural Behavior of Ultra-High Performance Concrete Prestressed I-Girders," Report No. FHWA-HRT-06-115, August, McLean, VA.

33. Graybeal, B.A., 2010, "Behavior of Field-Cast Ultra-High Performance Concrete Bridge Deck Connections Under Cyclic and Static Structural Loading," FHWA Publications, Report No. FHWA-HRT-11-023, Nov., McLean, VA.

34. Hansson, C.M; Poursaee A.; and Jaffer S.J., 2007, "Corrosion of Reinforcing Bars in Concrete," Portland Cement Association (PCA), R&D Serial No. 3013, Skokie, Illinois. www.cement.org

35. Hassan, T.; Rizkalla, S.; Abdelrahman, A.; and Tadros, G., 1999 "Design Recommendations for Bridge Deck Slabs Reinforced by Fiber Reinforced Polymers," Proceedings of the Fourth International Symposium on Fiber Reinforced Polymers Reinforcement for Concrete Structures, FRPRCS-4, ACI-SP-188, Baltimore, USA, pp. 313-323.

36. Hill, J.J.; McGinnis, L.G.; hughes, W.R.; and Shirole, A.M., 1988, "Design and Construction of Transversely Posttensioned Concrete Bulb Tee Beam Bridge," Transportation Research Record, Issue 1180, ISSN 0361-1981, Washington, DC, U.S.A., pp. 87-89.

37. Hlavacs, G.; Long, T.; Miller, R.; and Baseheart, T., 1996, Nondestructive Determination of Response of Shear Keys to Environmental and Structural Cyclic Loading. Transportation Research Record, V. 1574, pp. 18–24.

38. Huang, J.; French, C.E.; and Shield, C.K., 2004, "Behavior of Concrete Integral Abutment Bridges," St. Paul, Minnesota: Minnesota Department of Transportation.

39. Jo, B.W.; Tae, G.H.; and Kwon, B.Y., 2004, "Ductility Evaluation of Prestressed Concrete Beams with CFRP Tendons," Journal of Reinforced Plastics and Composites, ASCE, Vol. 23, No. 8, pp. 843-859.

40. Khaloo, A. and Mirzabozorg, H., 2003, "Load Distribution Factors in Simply Supported Skew Bridges," Journal of Bridge Engineering, Vol. 8, No. 4, July/August, pp. 241-244

41. Lall, J.; Alampalli, S.; and Di Cocco, E.F., 1998, "Performance of Full-Depth Shear Keys in Adjacent Prestressed Box Beam Bridges," PCI Journal, V. 43, No. 2, March–April, pp. 72–79.

42. Li, L.; Ma, Z.J.; and Oesterle, R.G., 2010, "Improved Longitudinal Joint Details in Decked Bulb Tees for Accelerated Bridge Construction: Fatigue Evaluation," Journal of bridge Engineering, Vol. 15, No. 5, Sept/Oct. pp. 511:522

43. Martin, L.D.; and Osborn, A.E.N., 1983, "Connections for Modular Precast Concrete Bridge Decks," Report No. FHWA/RD-82/106, US DOT, Federal Highway Administration.

44. Michigan Department of Transportation Construction and Technology Division, 2005, "Box-Beam Concerns Found Under the Bridge," C & T Research Record, No. 102, September, pp. 1-4.

45. Miller, R.A.; Hlavacs, G.M.; Long T.; and Greuel, A., 1999, "Full-Scale Testing of Shear Keys for Adjacent Box Girder Bridges," PCI Journal, V. 44, No. 6, November–December, pp. 80–90.

46. Morais, M.M. and Burgoyne, C. J., 2003 "Experimental Investigation of the Ductility of Beams Prestressed with FRP," Proceedings of the 6th International Symposium on FRP Reinforcement for Concrete Structures (FRPRCS-06), Singapore, pp.1013-1022.

47. Mutsuyoshi, H. and Machida, A., 1993, "Behavior of Prestressed Concrete Beams using FRP as Cable," Proceedings of International Symposium on FRP Reinforcement for Concrete Structures, American Concrete Institute, pp. 401–417.

48. Namaan, A.E.; Tan, K.H.; Jeong, S. M.; and Alkahiri, F.M., 1993, "Partially Prestressed Beams with Carbon Fiber Composite Cable Strands: Preliminary Tests on Strands," International Symposium on Fiber Reinforced-plastic Reinforcement for Concrete Structures, SP-138 ACI, Farmington Hills, MI, p. 441-464.

49. New York State Department of Transportation (NYSDOT), 1992, "Modifications of the Current Shear Key and Tendon System for Adjacent Beam Prestressed Concrete Structures," Engineering Instruction, pp. 1-6.

50. Oesterle, R.G. and Elremaily, A.F., 2009, “Design and Construction guidelines for Long-span Decked Precast, Prestressed concrete Girder bridge,” Final Report, NCHRP Project No. 12-69, www.trb.org

51. Owen C.R., 1987, “Continuity Strengthens South Fork Hoh River Bridge Replacement,” PCI Journal, Vol. 32, No. 1, Jan./Feb., pp. 86:103

52. Ozyildirim, C., 2011, “Case Study: Ultra High Performance Concrete with Steel Fibers for the Route 624 Bridge in Virginia,” SP-280, Advances in FRC Durability and field Applications, ACI symposium Publication 280 CD-ROM, Farmington Hill, Mich.

53. Park, H., 2003, “Model-Based Optimization of Ultra-High Performance Concrete Highway Bridge Girders,” Massachusetts Institute of Technology, Cambridge, MA.

54. Parsekian, G.A.; Shrive, N.G.; Brown, T. G.; Kroman, J.; Seibert, P. J.; Perry V. H.; and Boucher, A., 2008, “Innovative Ultra-high Performance Concrete Structures.” In Tailor Made Concrete Structures. Taylor & Francis Group, London, pp. 325-330.

55. Perry, V. and Weiss, G., 2009, “Innovative Field Cast UHPC Joints for Precast Bridge Decks Design, Prototype Testing and Projects,” UHPFRC 2009 – November 17th & 18th, Marseille, France

56. Popovics, S., 1973, "A Numerical Approach to the Complete Stress-Strain Curve of Concrete," Cement and Concrete Research, Vol. 3, No. 5, May, pp. 583–599.

57. Prestressed Concrete Institute (PCI), 2004, “PCI Design Handbook,” 6th Edition, Chicago, Illinois.

58. Soh, M., 2003, “Model-Based Design of Ultra-High Performance Concrete Prototype Highway Bridge Girder,” Massachusetts Institute of Technology, Cambridge, MA.

59. Stoll, F.; Saliba J.E.; and Casper L.E., 2000, “Experimental Study of CFRP-Prestressed High-Strength Concrete Bridge Beams,” Composite Structures (UK), Vol. 49, No. 2 pp.191-200.

60. Thorenfeldt, E.; Tomaszewicz, A.; and Jensen, J. J., 1987, "Mechanical Properties of High-Strength Concrete and Application in Design," Proceedings of the Symposium on Utilization of High-Strength Concrete, Tapir, Trondheim, pp. 149–159.

61. Tuchscherer, R.G.; Birrcher, D.B.; and Bayrak, O., 2011, “Strut-and-tie Model Design Provisions.” Precast/Prestressed Concrete Institute (PCI), winter 2011, 155-170.

62. Washington State Department of Transportation, 2008, “Bridge Standard Drawings,” http://www.wsdot.wa.gov/eesc/bridge/drawings/index.cfm?fuseaction=drawings &section_nbr=6&type_id=24

63. Youakim, S.A.; Karbhari, V.M.; Ghali, A.; and.Hida, S.E., 2007, “Prediction of Long-Term Prestress Losses,” Prestressed Concrete Institute Journal, March – April 2007, pp. 116-130.

64. Zou, P.X.W. and Shang, S., 2007, “Time-Dependent Behavior of Concrete Beams Pretensioned by Carbon Fiber-Reinforced Polymers (CFRP) Tendons.” Construction and Building Materials, Vol. 21, pp. 777-788.

65. Zsutty, T., 1971, “Shear Strength Prediction for Separate Categories of Simple Beam Tests.” ACI Structural Journal, 68 (2), 138–143.